

A Course of Solar Physics

Lecturer: Prof. Ashok Ambastha

Scribe: Yao Zhang

Introduction

A brief review of what covered in the course: a general introduction, ground-based observations and space-borne observations of the Sun; the solar interior: theory and probes; helioseismology: technique and results; solar activity and magnetic cycles; solar explosive phenomena: flares, CMEs.

These notes were TeX Live, though I edited for typos and used the editor TeXstudio.

I am responsible for all faults in this document, mathematical or otherwise; any merits of the material here should be credited to the lecturer, not to me.

Please email any corrections or suggestions to jaafar_zhang@163.com.

Acknowledgments

Thank you to all of my friends who will send me suggestions and corrections. My notes will be much improved due to your help.

I would like to especially thank Professor Ashock Ambastha, and Space Education and Research Foundation Ahmedabad, India who put this courses in website.

October 15, 2019, Beijing.

1 A general introduction of the Sun

1.1 Why the Sun is important to study?

1. Sun is the governor of our solar system, and source of all forms of energy, sustains life, weather and climate on Earth.
2. It has played a major role in development of mathematics and physics (Galileo, Kepler, Newton, Einstein)
3. Closest star and only star where it is possible to observe surface structure, dynamics and study various physical processes. The rosetta stone of astronomy.
4. Manifestations of the Sun: quiet, active, dynamic and explosive
 - Drives the space weather and planetary environments.
5. Sun's interior and exterior provide a cosmic laboratory for:
 - atomic physics, nuclear and neutrino physics, high temperature plasma physics and MHD, general relativity

1.2 The Sun, our day-time star – The governor of solar system

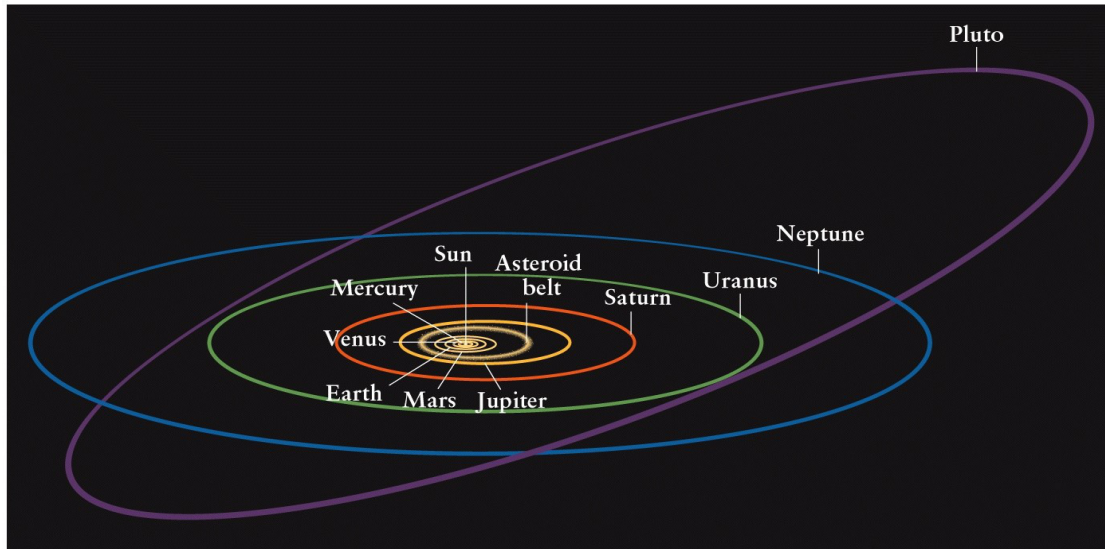


Figure 1: Solar System

1.3 The extended solar system

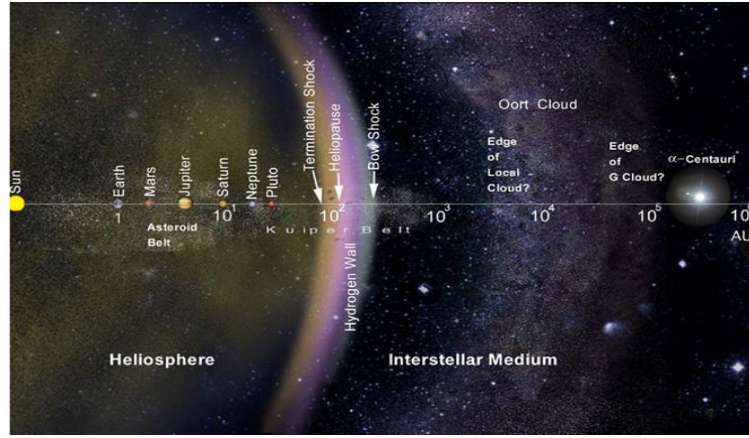


Figure 2: The solar system, including the Oort Cloud, on a logarithmic scale.

1. AU: astronomical unit, a unit of measurement equal to 149.6 million kilometers, the mean distance from the center of the Earth to the center of the Sun.
2. Kuiper Belt, or the 3rd zone, Pluto, Eris, and icy bodies \Rightarrow extends from 30 - 50 AU
3. Termination shock: At 200-230 AU where solar wind collides with ISM and piles up into a comet-like tail away from Sun.
4. Oort Cloud; (theorized) cloud of icy objects at a distance of 100,000 AU or 1.9 lt-year away. Long-period comets are thought to originate from this region.

1.4 Our modest, average day-time star: the Sun

The Sun is our (Earth's) closest star, therefore is a great deal easier to study its surface in detail. The next nearest star is about 250,000 times as far!

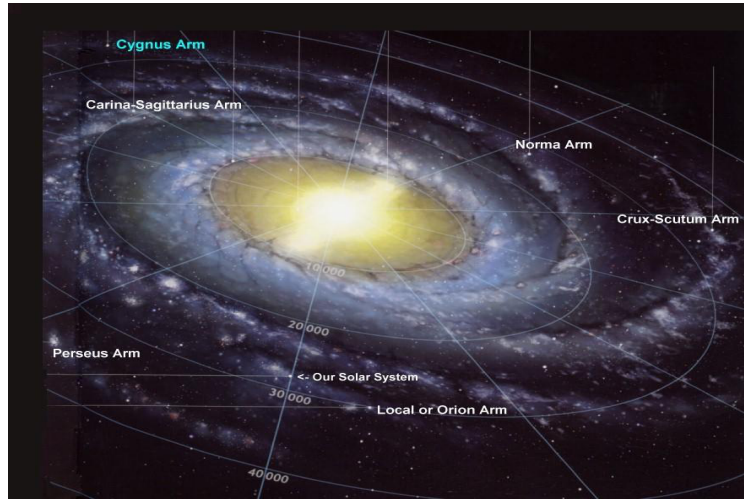


Figure 3: The Sun is only an average star, and one of the ~ 400 billion stars of our galaxy: the Milky Way

Remark. Another unit for astronomical distances: parsec (pc). 1 parsec is defined as the distance at which 1 AU will extend an angle of 1 arc-second (~ 3.26 ly). Galactic sizes : Kilo parsecs (kpc). Extra-galactic distances : Mega parsecs (Mpc).

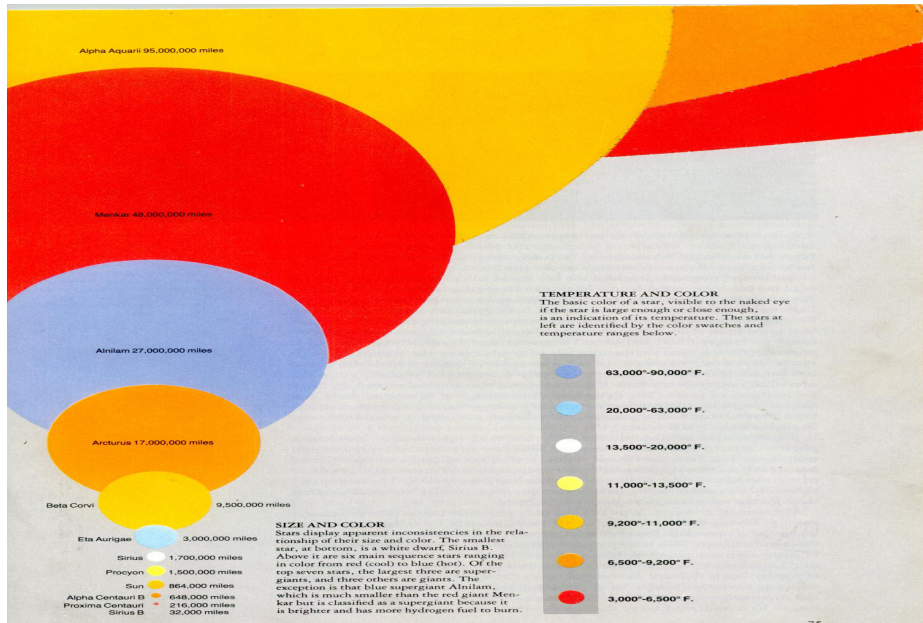
1.5 Structural map of the Milky Way as constructed from theory and observations

Our Milky Way Galaxy, home to 400 billion stars: spiral galaxy consisting of central bulge, 5 major arms, and some shorter local arms. Sun is located in local Orion arm at 28 kly from Center, takes



230 million years at a velocity of 828,000 km/hr., for one orbit around the Milky Way!

1.6 The Sun is an average star as compared to some other stars



- A spiral galaxy like the Milky Way contains stars, stellar remnants, and a diffuse interstellar medium (ISM) of gas and dust. ...

- Molecular cloud, also called a stellar nursery, is a type of interstellar cloud higher density regions, which permit the formation of molecules, most common molecular hydrogen (H_2). These are regions where star formation takes place.



(a) Two dramatic star formation regions in the Southern Milky Way

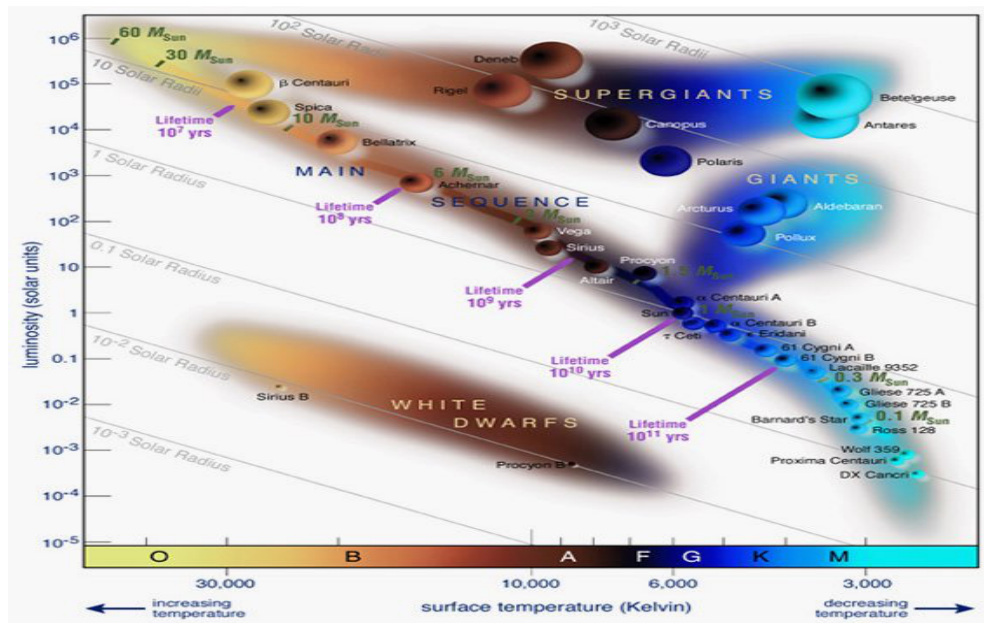


(b) Eagle Nebula is one of the best examples of molecular clouds

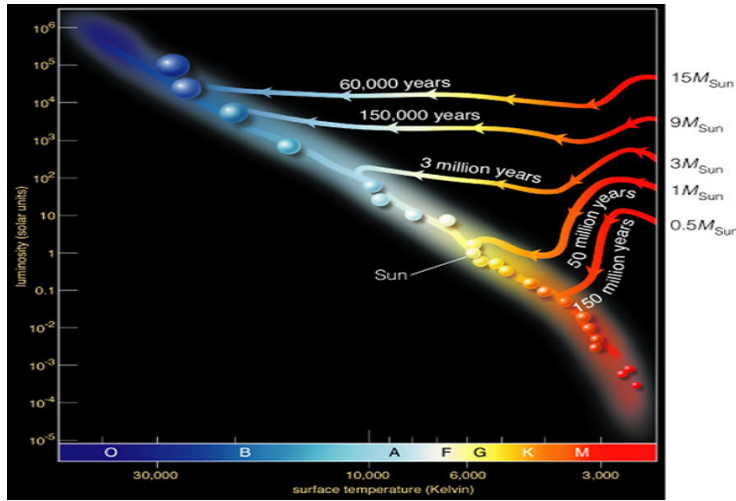
$T \sim 10$ K, and densities $> 10^2$ particles/cm³, masses ranging from a few to over a million solar masses and diameters from 20 to 200 parsecs. Located mostly in disks of spiral galaxies like Milky way, and irregular galaxies.

1.7 Classification of stars by spectral class—The H-R diagram

The Hertzsprung–Russell diagram, or H–R diagram, is a scatter plot of stars' absolute magnitudes/luminosities v/s their stellar classifications/effective temperatures.



1.8 Pre-main sequence contraction of stars

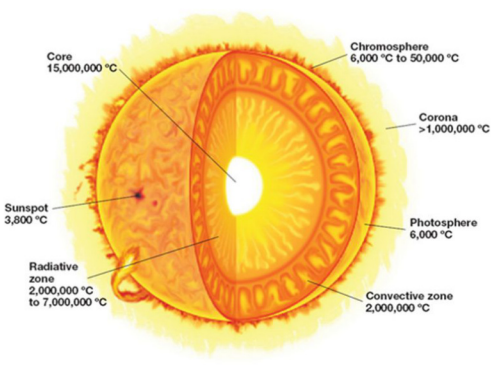


Low mass protostars contract more slowly.

Duration on main sequence depends on the ratio of mass and luminosity, or on the amount of hydrogen in the star's core and the rate at which the hydrogen is consumed \Rightarrow The more massive a star, the shorter is its main-sequence lifetime.

1.9 The luminosity of the Sun

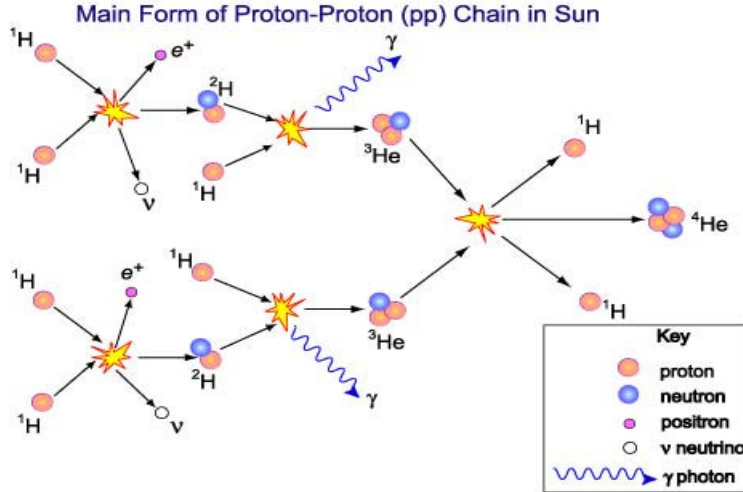
The luminosity of the Sun is due to the powerhouse operating in the solar interior, the central engine. But, the Sun reached this main sequence stage after its evolutionary phase lasting 50 million years from proto-sun.



1. Core: energy generated by thermonuclear fusion
2. Radiative zone: energy transport by radiation.
3. Convective zone: energy transport by convection.

1.10 The core: central engine driving the Sun

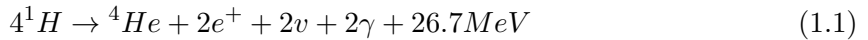
Sun's core is very dense, and hot $\geq \frac{1}{2} M_s$ within $\frac{1}{4} R_s$, \geq density ~ 160 gm/cc, $T_{core} \sim 15 \times 10^6$ °K, $P_{core} \sim 250 \times 10^9$ Earth atmospheres.



- Step 1: ${}^1H + {}^1H \rightarrow {}^2H + e^+ + \nu$ ($Q = 1.44 MeV$)
- Step 2: ${}^2H + {}^1H \rightarrow {}^3He + \gamma$ ($Q = 5.49 MeV$), 3He can react with 1H , but the result 4Li is unusable (i.e. ${}^3He + {}^1H \rightarrow {}^4Li \rightarrow {}^3He + {}^1H$)
- Step 3: ${}^3He + {}^3He \rightarrow {}^4He + 2{}^1H + \gamma$ ($Q = 12.86 MeV$)
- The net result is : $4{}^1H \rightarrow {}^4He + 2e^+ + 2\nu$ ($Q = 26.7 MeV$)

1.11 Energy powerhouse—the core

- The net p-p fusion reaction in the core :



- i.e. 4 protons fuse to give one helium nucleus, and release of energy.
- Mass of $4{}^1H$ (4.0331 amu) is greater than 4He (4.0026 amu) \Rightarrow Mass converted to energy via $E = mc^2$. (1 amu = 1.66×10^{-30} gm, and $c = 3.0 \times 10^8$ m/s). Mass loss per reaction = $\Delta M = 0.02866$ amu = 4.8×10^{-32} gm. Energy produced per reaction = $\Delta M \times c^2 = 4.3 \times 10^{-5}$ ergs = 4.3×10^{-12} Joules.
- Sun loses $\sim 6 \times 10^{12}$ gm/s, i.e., $\sim 10^{-13}$ of its 2×10^{33} gm mass per year to give solar luminosity of 3.8×10^{26} W.
- As this high energy photon moves outwards through the radiative and convective zones, it interacts with the dense medium and transforms to photons with lower energy – giving rise to entire radiation spectrum we see.

1.12 Future of our Sun in ~ 5 Gyr

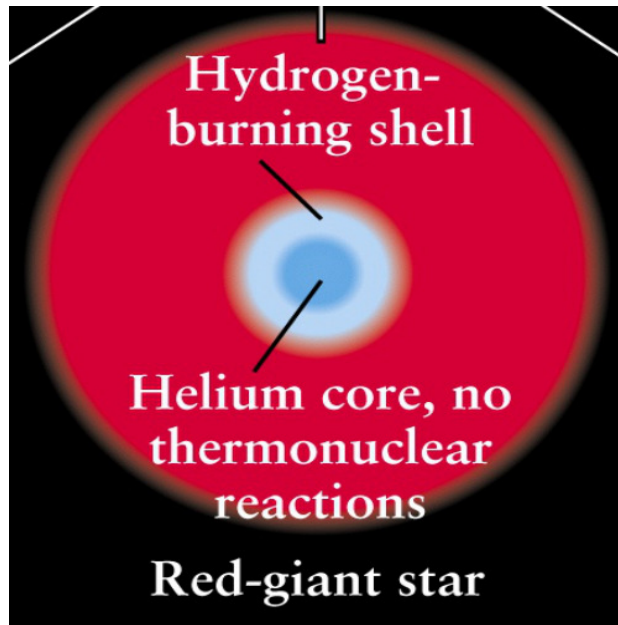


Figure 4: Helium fusion at the center of a red giant

- Sun is powered by p-p fusion reaction in central core.
- As H in the core is consumed resulting in He core, it will cool and begin to contract.
- This will lead to raising T in the surrounding, where H will start burning \Rightarrow less gravity from above to balance this pressure.
- So, it will start swelling up and become a red giant.
- The outer layers of the Sun will grow beyond Mercury and Venus, and may even reach out as far as Earth.

1.13 Planetary nebula formation: end (death) of a Sun-like star

When the red giant exhausts its He fuel:

- the core collapses \rightarrow white dwarf (WD)
- No fusion inside \rightarrow a dead star
- WD size slightly less than that of the Earth, dense, one teaspoon ~ 15 tons!
- WD from an isolated star simply cools, T decreasing until no longer visible \rightarrow "black dwarf".

Pressure of He & H burning shells overcome gravity so the outer envelope of the star is blown outward \rightarrow forms a planetary nebula.

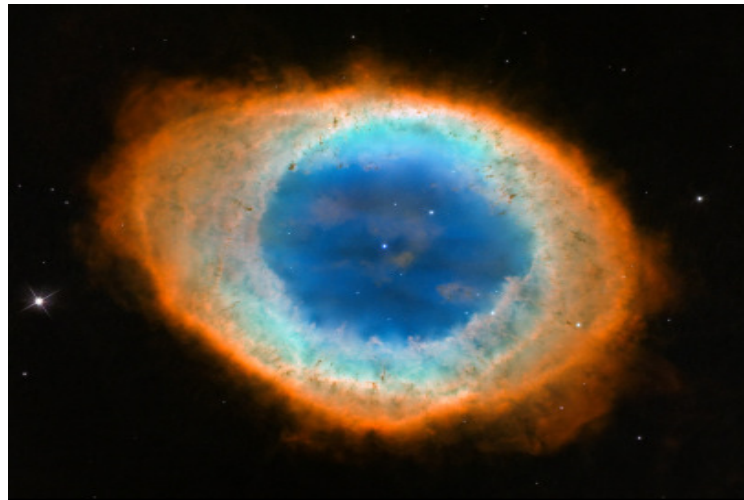
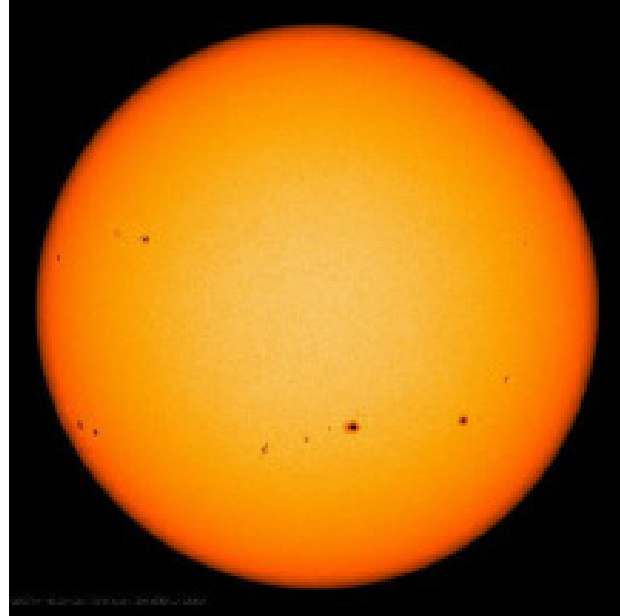


Figure 5: M57–The Ring Nebula (A Hubble Picture)

1.14 General properties: distance and diameter

- Angular diameter $\theta = 32\text{arc-min}$ (from observations)
- Sun-Earth distance $R_\theta = 1.49 \times 10^8 \text{ km}$ (1 AU = 8.3 light minutes)
- (Transits of Venus, and also from Kepler's 3rd law and trigonometric parallax of Venus)
- Sun's diameter is therefore: $d = R_\theta \theta$, where $\theta = 0.5\text{deg} = 0.5 \times 2\pi/360$ in radians for Sun, and R_θ is Earth-Sun distance.

Therefore, $d_\theta = 1.49 \times 10^{11} \text{ m} \times (0.5 \times 2\pi/360) = 1.3 \times 10^9 \text{ m}$, (Precise value of d_θ is 1,391,978 km)



1.15 Mass of the Sun

- Consider Earth (m) in circular orbit about Sun (m_θ) at velocity (v) and distance (R). From Newton's Law of Gravity, planet held in orbit by force:

$$F_g = \frac{Gmm_\theta}{R^2} \quad (1.2)$$

For centripetal force on Earth:

$$F_c = ma = m\left(\frac{v^2}{R}\right) \quad (1.3)$$

- Therefore, for equilibrium

$$F_c = F_g \Rightarrow m(v^2/R) = (Gm_\theta m)/R^2 \Rightarrow m_\theta = (v^2/RG) \quad (1.4)$$

- But $v = (\text{distance in orbit} / \text{Period of Earth's orbit}) = 2\pi R/P$

- Therefore,

$$m_\theta = (v^2/RG) = (4\pi^2 R)/(GP^2) \quad (1.5)$$

- If R , P and G are known, we can calculate mass of the Sun, and

$$G \sim 6.67 \times 10^{-11} m^3 \cdot kg^{-1} \cdot s^{-2} \quad (1.6)$$

$$m_\theta = (1.989 \pm 0.003) \times 10^{33} gm \quad (1.7)$$

\Rightarrow contains 99.8% of mass of solar system. But there is a minute change in solar mass due to mass loss:

1. through radiation $\sim 6 \times 10^{12} gm/s$ (using solar luminosity),
2. $10^{12} gm/s$ is carried away by the solar wind.

1.16 Mean density, escape velocity of the Sun

- The mean density of Sun

$$r_\theta = m_\theta/Vol_\theta \Rightarrow r_\theta = 1.41 gm/cm^3 \quad (1.8)$$

(Earth's average density $5.51 gm/cm^3$)

- Escape velocity on solar surface is given by K.E.= P.E.

$$\Rightarrow \frac{1}{2}mv_e^2 = (Gmm_\theta/r_\theta) \quad (1.9)$$

- Therefore,

$$v_e = \sqrt{2Gm_\theta/r_\theta}, \quad v_\theta = 618 km/s \quad (1.10)$$

- The gravitational acceleration on the surface of Sun,

$$g_\theta = Gm_\theta/r_\theta^2 = 274 ms^{-2} \quad (1.11)$$

1.17 Surface temperature of the Sun

The Sun emits nearly as a ‘blackbody’ its spectrum with $\lambda_{peak} \sim 510nm$. The effective temperature of the Sun can be determined by the peak of its output (Wien’s displacement law), or by Stefan-Boltzmann law and knowledge of the Sun’s radius r_θ : Wein’s Law for black bodies:

$$\begin{aligned} T_\theta &= (2.8978 \times 10^{-3})/\lambda_{peak} {}^\circ K \\ \Rightarrow T_\theta &= (2.8978 \times 10^{-3})/(510 \times 10^{-9}) \\ \Rightarrow T_\theta &= 5700 {}^\circ K \end{aligned} \quad (1.12)$$

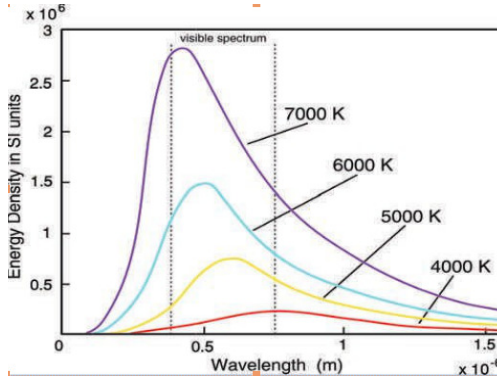


Figure 6: Body Level One

1.18 Sun’s power output (luminosity) and solar constant (solar irradiance)

- Solar constant S_θ or total irradiance or the radiation flux outside the Earth’s atmosphere (at distance $R_\theta = 1AU$ from Sun) integrated over all wavelengths can be measured directly. It is usually measured as $S_\theta = 1367 \pm 3Wm^{-2}$.

Luminosity $L_\theta = (4\pi R^2)S = 4\pi(1.50 \times 10^{11} m)^2 1370 w/m^2 = 3.9 \times 10^{26}$ watts. Alternatively, using Stefan-Boltzmann law (once we know the effective temperature T_θ ,

$$\begin{aligned} L_\theta &= (4\pi r_\theta^2)(\sigma T_\theta^4) \\ &= 4\pi(7 \times 10^8 m)^2 5.67 \times 10^{-8} watts / (m^2 K^4) T_\theta^4 \\ &= 3.9 \times 10^{26} watts \end{aligned} \quad (1.13)$$

where, $T_\theta = 5700K$, and Stefan-Boltzmann constant is $10^{-8} Wm^{-2} K^{-4}$

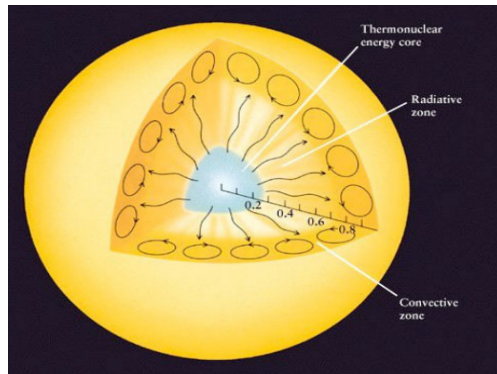
- Note, however, that the solar constant is NOT a constant. It has been varying from the early stages over different time scales. Recent space observations indicate that the on average $S_\theta \sim 1366 Wm^{-2}$ around solar minima and $1367 Wm^{-2}$ near solar maxima.

1.19 What happens to neutrinos produced in the core?

- Fusion processes produce neutrinos at almost every step of the p-p chain along with γ -ray photons.
- Neutrino propagation through the interior
 - Because neutrinos are very weakly interacting particles, they pass through the solar atmosphere unhindered.
 - Experiments to detect solar neutrinos began in the 1960s, which reported far too few neutrinos by detectors on Earth based as compared to predictions from standard models of the solar interior.
 - Only recently has this problem been resolved by the discovery of neutrino oscillation from one flavor to another.
- The photons (γ -rays) from the core cannot fly out and reach us directly through the interior.
 - In the region $0.2R_\theta$ to $\sim 0.75R_\theta$ the material's ability to block light, or opacity, is low. Therefore the energy produced in the core is most efficiently lost by radiation - Radiative Zone.
 - However, because the gas density is high, photons are absorbed by atoms in the gas and emitted in a random direction \Rightarrow A photon executes a random walk from the core to outwards.
 - The mean free path of photons is of a order of 1-2 cm.
- Due to this random-walk process, photons are trapped and take 10,000 years before actually reaching the edge of the radiative zone from the core (as compared to the direct flight time of about 2 sec!).

1.20 Energy transport through the solar interior: radiative zone

The temperature falls from 8×10^6 from the outer core to about 2×10^6 in the zone $0.25 < r/R_\theta < 0.75$, From Wien's law: for $T \sim 10MK$, $\lambda_{max} \sim 0.25nm$, Density falls from ~ 20 g/cc to ~ 0.2 gm/cc (full of X-rays)



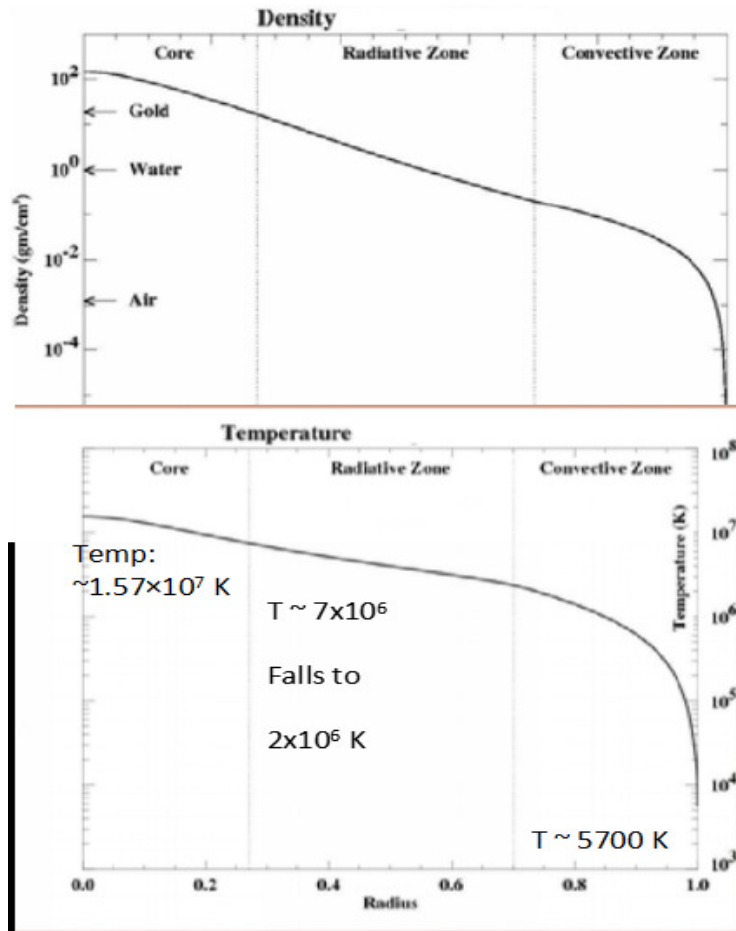
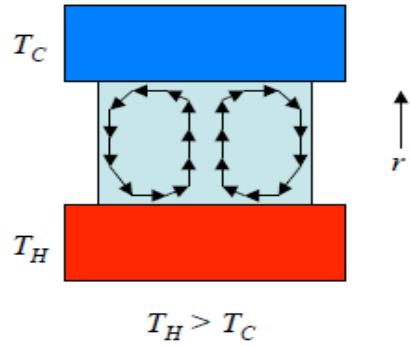


Figure 7: Convective zone

Temperature falls from 2×10^6 at the radiative zone to about 6000° close to Sun's surface, and density $\rho < 0.2\text{g/cc}$ down to $\sim 0.0002\text{g/cc}$

- Photons are continuously absorbed in lower layers of this region as T is sufficiently low to form atoms, leading to temperature gradient between the lower layer and upper layer - more opaque (optically thick)
- heat starts to build up at the lower layer— setting up of convection that dominates through the outermost 30% of solar interior.

Convection much faster way for transfer of energy than radiation in this opaque medium – Convective zone– and it takes heat energy now only 10-30 days to climb through!



1.21 Photosphere

- At the top of the convection zone, the optical depth of the solar atmosphere rapidly decreases over a few hundred kilometers. Optical depth (τ) is the wavelength-dependent measure of a material's transparency. It is related to light scattered or absorbed by $I/I_0 = e^{-\tau}$.
- For $\tau > 1$ the material is “optically thick” as most photons cannot pass through without being scattered or absorbed.
- For $\tau < 1$, the material is “optically thin” and most photons are able to escape without interaction.
- For $\tau = 1$, surface layer where observed photons originate . This is called the photosphere.

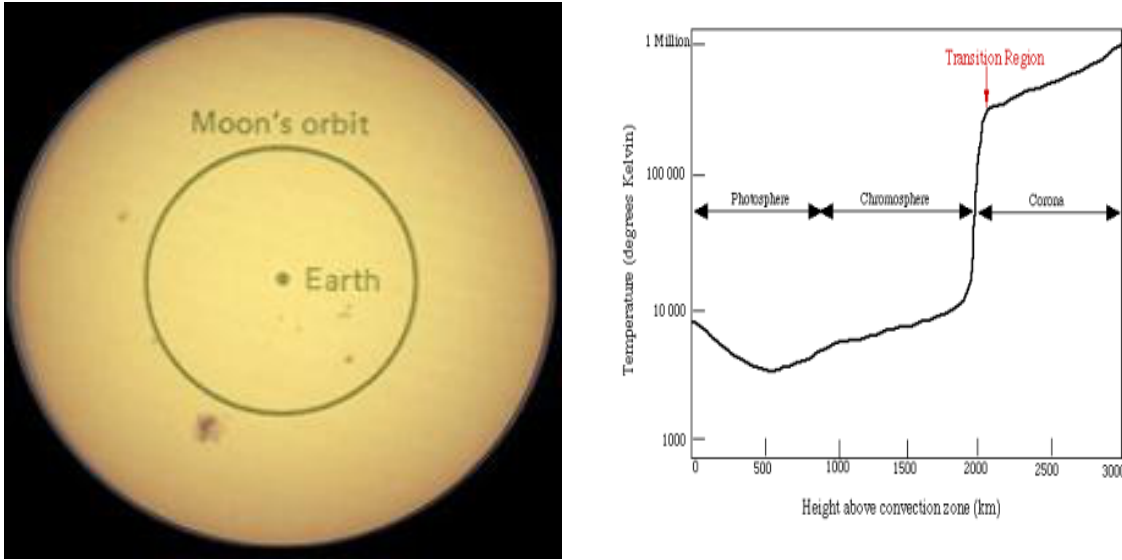
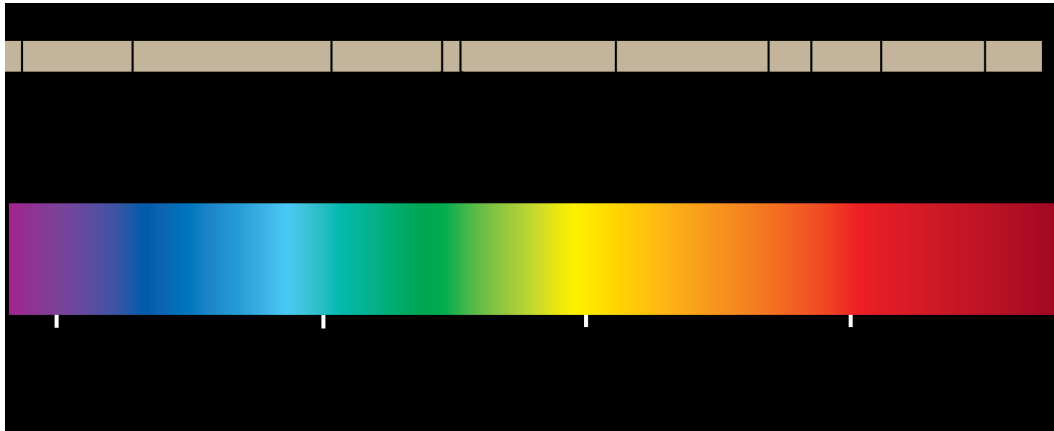


Figure 8: Surface of the Sun: $T_{eff} = 5776K$, but photosphere T ranges from 6500 K at the bottom to 4400 K at the top.

The energy carried out by g-ray photons produced in the core goes down as it travels from the core through the radiation zone and above to X-ray, then into the UV, visible, IR and beyond to radio over the entire EM spectrum (black-body spectrum). These photons are messengers carrying



information of Sun's structure and dynamics.

Dark lines in the Spectrum: Fraunhofer absorption lines Over 20,000 absorption lines have been identified in the solar spectrum from the photosphere, “thumb prints” of elements in solar photosphere and chromosphere.

1.22 A black-body at Sun's temperature and solar electromagnetic spectrum

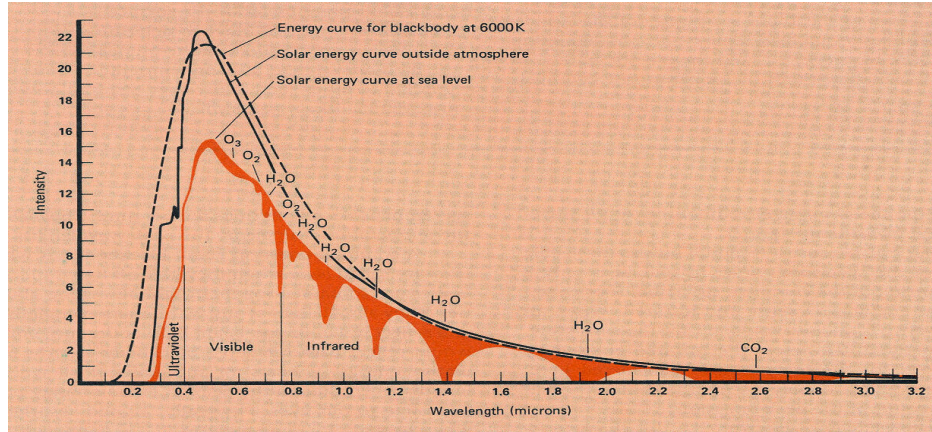


Figure 9: Earth's atmosphere absorbs a part of solar radiation – UV (by ozone) and IR (by water vapor and CO_2)

Solar energy at the earth's orbit and the attenuation by the earth's atmosphere. The sea level curve shows the spectrum along with atmospheric molecules responsible for absorption at different wavelengths (Hynek 1951)

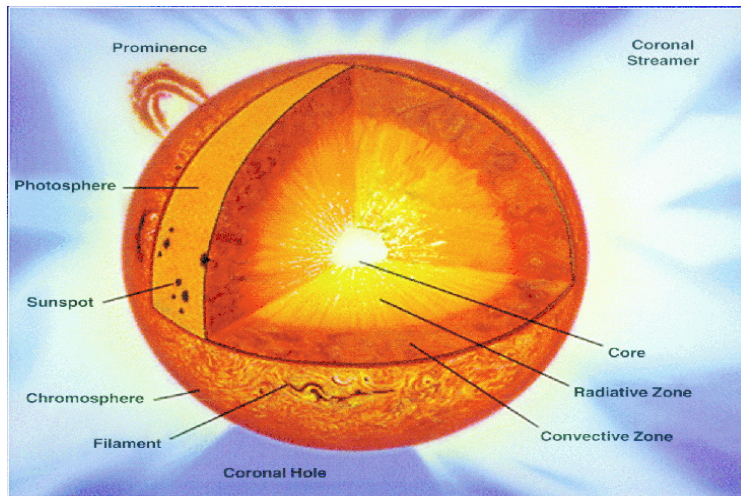
1.23 General properties of the Sun: summary

- Angular Diameter $\theta = 32\text{arc-min}$ (from observations)

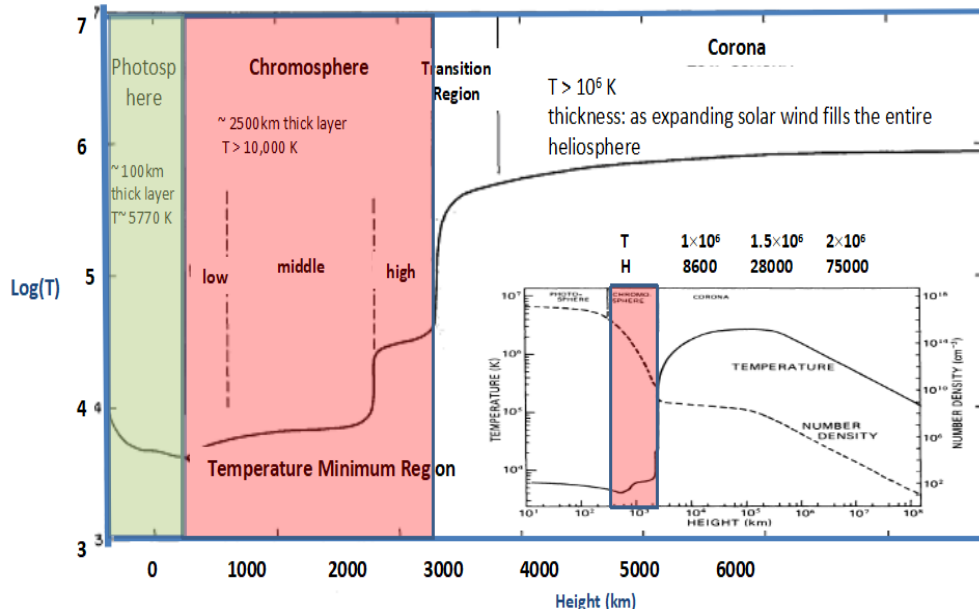
- Distance $R_\theta = 1.5 \times 10^8 \text{ km}$ (1 AU = 8.3 light minutes) (from Kepler's 3rd law and trigonometric parallax of Venus)
- Radius $r_\theta = 7 \times 10^5 \text{ km} = 109 R_\oplus$ (from geometry: $d = 2r = R\theta$)
- Mass $M_\oplus = 2 \times 10^{33} \text{ gm} = 3,33,000 M_\oplus$ (from Kepler's 3rd law, $M = (4\pi^2/G)d^3 P^2$), Av. Density $1\rho_\oplus 1.4 \text{ gm/cc} = 0.255 \rho_\oplus$
- Temperature $T_\theta = 5800^\circ K$ (from Wien's law $l_{peak} T_{eff} = c$, or black body law: $L_\theta = 4\pi R^2 \sigma T_\theta^4$)
- Solar Constant $S_\theta = 1367 \text{ Watts/m}^2$ (from observations)
- Luminosity $L_\theta = 3.85 \times 10^{26} \text{ Watts}$ (from the inverse-square law: $L = 4\pi d^2 f$)
- Average Magnetic field strength = 1-3 gauss (polarimetry & Zeeman effect)
- Composition 74% Hydrogen, 24% Helium, and 2% others (by mass) (from spectroscopy)
- Solar Differential rotation = 28—37 days
- Present age = $4.6'10^9$ yrs

1.24 External atmosphere of the Sun

- Photosphere: The visible solar surface : changes from completely opaque to transparent to radiation .
- Chromosphere: Hot and thin layer $\sim 2000 \text{ km}$ thick
- Transition Region: thin, hotter region of steep temperature and density gradients
- Corona: T rises more rapidly to greater than one million degrees.



1.25 Temperature/density variation in outer layers of Sun's atmosphere



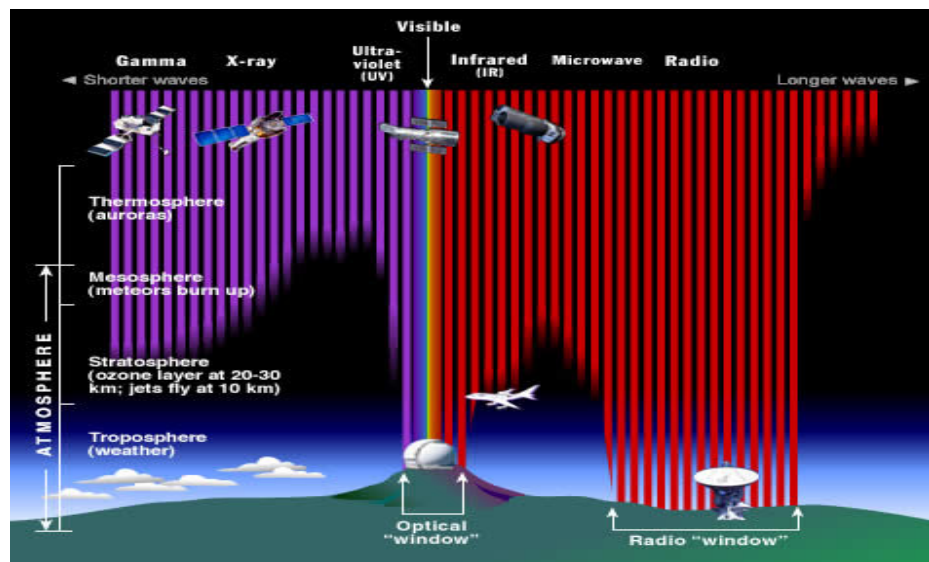
1. Photosphere – Density: $\sim 0.0002 \text{ g/cm}^3$ visible by protected eyes/telescopes
2. Chromosphere – Density $\sim 10^{-4} \times$ photosphere, and $10^{-8} \times$ Earth's atmosphere at sea level. Visible only during TSEs, and by telescopes aided with special optical filters
3. Corona – Very low density ($\sim 10^{12} \text{ particle/cm}^3$). visible as faint white-light solar crown during TSEs, invisible otherwise, except from space in X-ray and UV .

1.26 Web sites of interest

1. SOHO Homepage: <https://sohowww.nascom.nasa.gov/>
2. Extensive data and educational material: <http://solar-center.stanford.edu/>
3. National Solar Observatory, USA: <https://www.nso.edu/>
4. Solar News and current activities: <https://solarnews.nso.edu/>
5. The Sun now: Solar Dynamics Obs.: <https://sdo.gsfc.nasa.gov/>
6. Solar activity, space-weather, etc.: <http://spaceweather.com>

2 Ground-based observations of the Sun

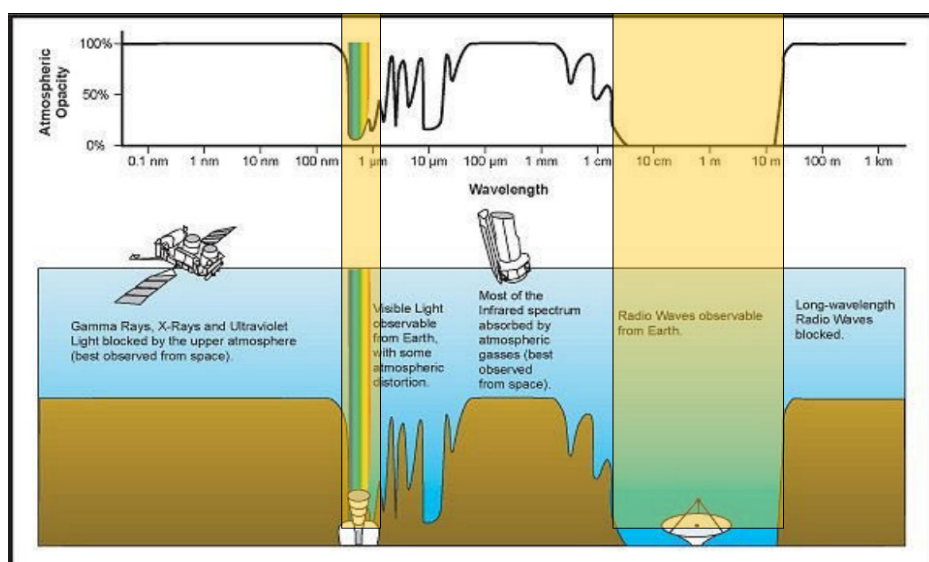
2.1 Sun's (star's) radiation passage through the Earth's atmosphere



There are windows in visible (optical) and radio wavelengths for observing from ground.

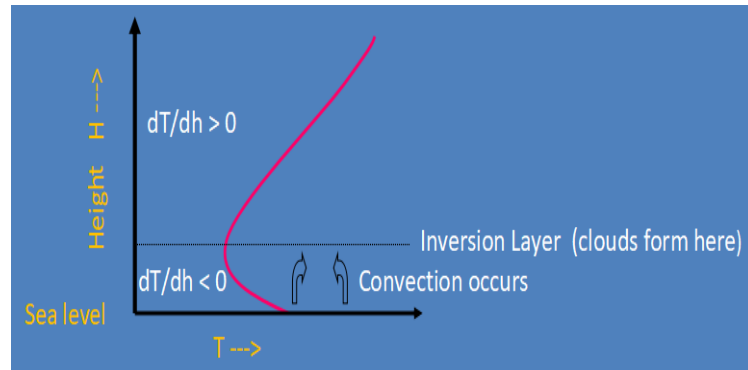
The radio waves are not absorbed by clouds or dust in the atmosphere, while visible light gets absorbed/scattered/blocked.. Also thermal convection/turbulence distorts imaging.

2.2 Observation the Sun in various wavelengths



2.3 Selection of solar (optical) observing site

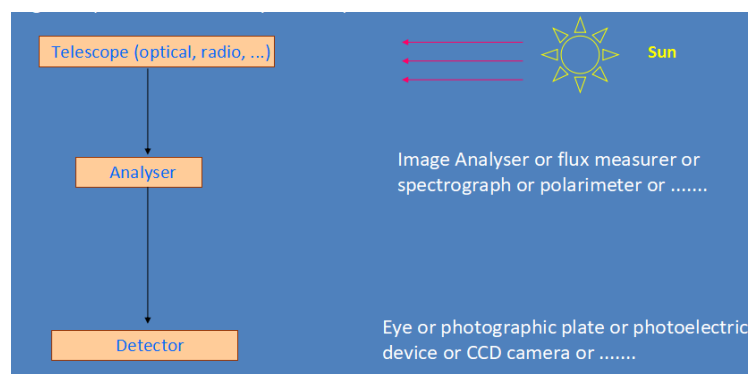
1. Clear Sky condition (cloudless, dust-free ...)
2. Good “seeing” condition (minimum atmospheric turbulence)
3. Little or no water vapour (important for IR wavelengths)



1. Lake/ocean (large water body) sites preferred for reduced local turbulence
2. High altitude (mountains) for low water vapour, cloudless, dust-free environs
3. Careful dome, building design to reduce local/internal turbulence

2.4 Observing the Sun (or other cosmic objects)

By collecting and analysing the photons using Eye (caution), optical ..radio.. Telescopes (from ground) and UV, EUV, X-ray.. From space



2.5 Selection of solar telescope design

- Reflector v/s refractor
- Telescope with short primary focus: compact size, but excessive heating; preferable for polarimetry.
- Telescope with long focal length: large image size, large physical size of the telescope, big mechanical system/mounts required.
- Stationary telescopes: good for massive backend instruments
- Open (collapsible) dome-less design to reduce local heating
- Telescope evacuation, or inert gas (Helium, Argon) filling for reducing the internal turbulence.



Figure 10: USO's Open (collapsible) Dome

2.6 Observing the Sun in optical wavelengths



Figure 11: Udaipur Solar Observatory, Udaipur (Rajasthan), India. Solar optical facilities in India also in Kodaikanal, and Nainital

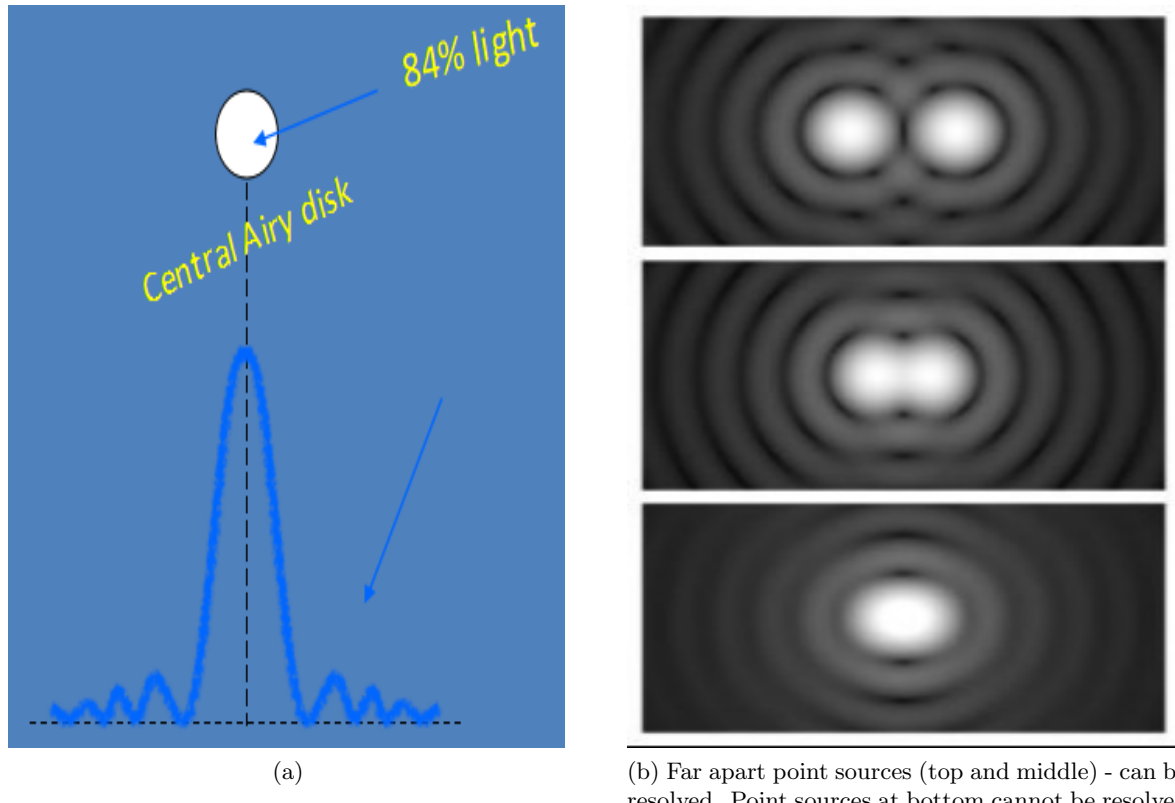
The observatory is located in the lake to reduce image distortion which occurs when the Sun heats the ground, producing convection currents. The reduction of local convection currents along with the large number of cloudless skies make USO one of the best sites in the world for solar observations.

2.7 Some notable solar optical telescopes surrounded by large water bodies

- Big Bear Solar Observatory (BBSO), located in Big Bear Lake, California (USA), operated by NJIT
- Swedish 1-m Solar Telescope, operated by the Institute for Solar Physics (Sweden), is located in La Palma island (Spain).
- Multi-Application Solar Telescope (MAST)- Udaipur (India) operates many other solar instruments
- The Huairou Solar Observing Station, Beijing, China - On a north bank of the Huairou Reservoir, about 40km north of Beijing
- Fuxian Solar Observatory (FSO), Yunnan, China - northeast side of Fuxian Lake
- There are many solar telescopes on high towers located on mountain tops

2.8 Spatial resolution of a telescope

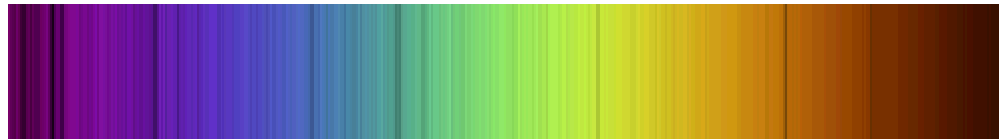
Resolving power is limit in detail that telescope can image. Light from point source generates an Airy pattern when viewed through telescope. Theoretical diffraction pattern of a point source.



Most of the light is concentrated in central bright spot (the Airy disk). The diffraction limited

spatial resolution a is given by the first zero of Bessel's function J_1 , i.e. $a = \frac{1.221}{D}$ radians, where $1 = \text{wavelength of light}$, $D = \text{diameter of the telescopes aperture}$. However, actual resolution depends on atmospheric seeing.

2.9 Optical observations of the Sun: continuum and spectral line diagnostics



- White light or continuum : Usually neutral density filters are used to reduce heat flux entering the telescope
- Spectral Fraunhofer lines : Narrow pass-band filters at entrance or near focal plane are used
 - Measurement of Velocity – Doppler shift

$$\frac{\Delta\lambda}{\lambda} = \frac{v}{c} \quad (2.1)$$

- Measurement of Magnetic Fields: Zeeman Effect - line splitting
- Measurement of Temperature and turbulent velocity : Line width
- Elemental abundance, temperature (via ionisation and excitation balance): Equivalent width
- Inhomogeneities in the solar atmosphere: Line asymmetry

2.10 What do we observe in WL(white-light) or continuum?

The yellow luminous disk ... Photosphere – outer skin of Sun.

- At the top of the convection zone, the optical depth of the solar atmosphere rapidly decreases over a few hundred kilometers.
- Thickness ~ 150 km (pressure scale height at $T_{eff} \sim 5700K$).
- Average temperature varies from 6500 K at the bottom (near the convection zone) to 4400 K at the top.

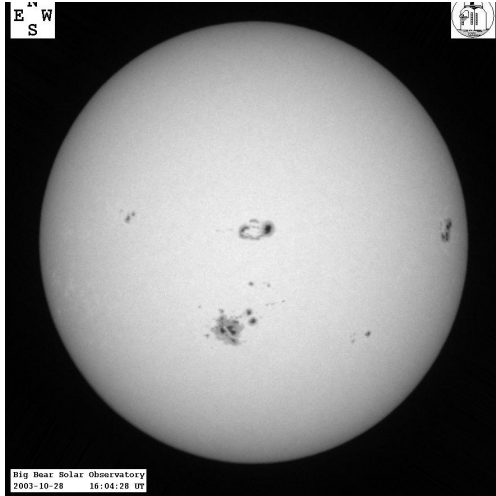
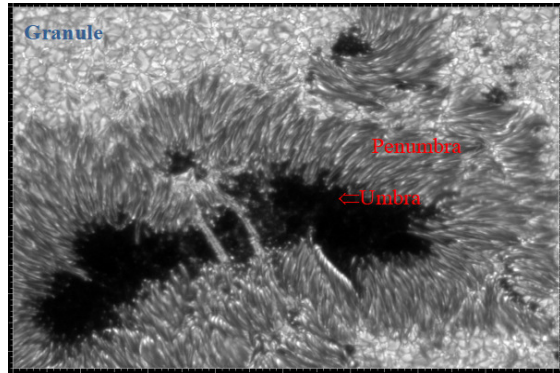


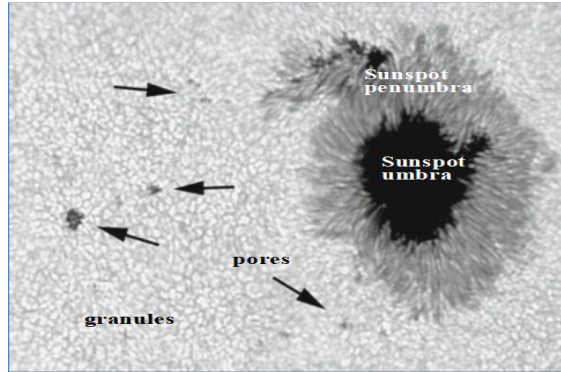
Figure 12: A white-light image of the Sun shows limb darkening effect, sharp solar edge and several dark sunspots (but not always), faculae, and granules.

Sunspots are dark localized irregular features. Occur as single spots or in groups in a latitude belt between 40° N and S. Lifetime: \sim an hour to weeks. Sizes: from the resolution limit of telescope to \sim 100,000 km!



- Not more than \sim 1% of hemisphere is covered by sunspots at a given time.
- Well developed sunspots show dark interior (umbra), surrounded by lighter (penumbra)
- Appear dark due to lower T than the surroundings: due to magnetic fields > 1000 G
- According to Stephan-Boltzmann law, black-body irradiance is T^4 so the ratio of brightness of a typical sunspot (say $T=4100$ K) to that of the surrounding disk ($T=5800$ K) would be $(4100K/5800K)^{1/4} = 25\%$.

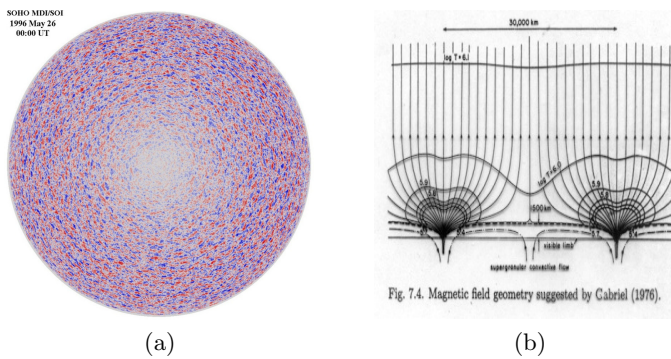
2.11 The granules: convection cells



- polygonal cells in 'quiet' photosphere, \Rightarrow evidence of convection
- \Rightarrow upward-moving, hot gas
- central upflow ~ 0.4 km/s, surrounded by horizontal outflow ~ 0.25 km/s, a small downflow at dark intergranular lanes boundaries.
- granules form due to large temperature gradients close to the surface.
- granules evolve – coalesce, expand, fragment, explode.
- sizes: 1000 km across (size 1.5–2 arc-secs), lasting ~ 15 minutes (largest granules last longest).
- quiet photosphere granules are $\sim 30\%$ brighter than the inter-granular lanes \Rightarrow temperature difference of $\sim 400^\circ$.

Velocity images of Sun show also larger scale convective structures, such as “mesogranules” (~ 10 arc-sec size) and “supergranules” (~ 40 arc-sec size).

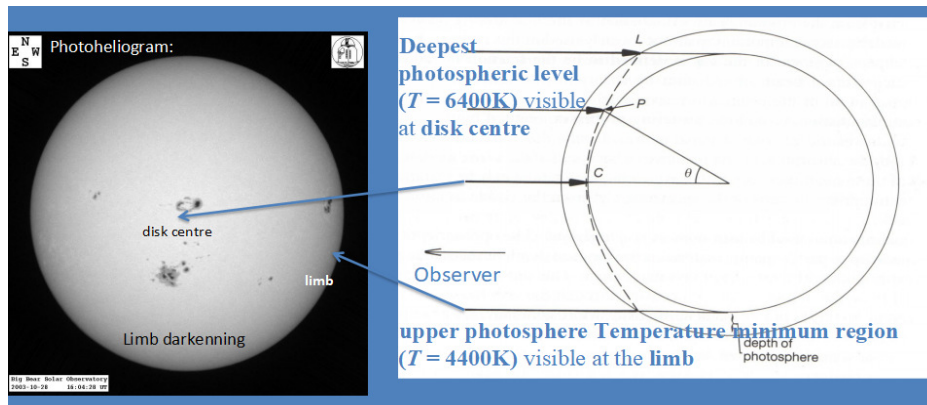
2.12 Supergranules



- They cover entire solar surface, continually evolving. more deep rooted than granules

- Best seen in measurements of the "Doppler shift"
- Individual supergranules last for a day or two and have flow speeds of about 0.5 km/s (1000 mph)
- Size $\sim 18\text{--}20 \times$ granulations
- Lifetime $\sim 120 \times$ granules lifetime
- Fluid flows observed in supergranules carry magnetic field bundles to the edges of the cells where they produce the chromospheric network.

2.13 Limb darkening: the photospheric limb is darker than the center



At the center of the disk of the Sun we look straight in and see somewhat deeper, hotter and brighter regions. Limb darkening observed where $dT/dh < 0$.

limb darkening (decrease of solar intensity with angle θ):

$$I(\theta) = I(0) [1 - u(1 - \cos(\theta))] \quad (2.2)$$

where u is limb darkening coefficient.

For limb, $\theta = 90$ and for center, $\theta = 0$. so one has

$$u = \frac{I(\text{center}) - I(\text{limb})}{I(\text{center})} \quad (2.3)$$

u is wavelength dependent.

Effective temperature is the average kinetic temperature of the Sun.

2.14 Wavelength dependence of limb darkening

- Limb darkening depends on wavelength
- More pronounced in violet than in the red region of the spectrum.
- In FIR ~ 9 micron, opacity is very high, both at the limb and disk center, radiation comes only from the outer-most layers of the photosphere, therefore, limb darkening curve in FIR is almost flat
- As the limb darkening is caused due to the photospheric temperature gradient dT/dh , it disappears in FIR and in UV ~ 0.15 micron, where $dT/dh \sim 0$ or > 0 .

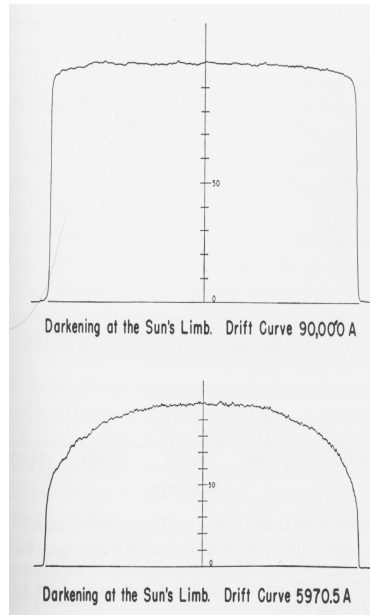


Figure 13: Limb darkening profiles at $90,000 \text{ } \text{\AA}$ (9 micron) (top curve) shows nearly no limb-darkening. At $5970.5 \text{ } \text{\AA}$ (lower curve) shows strong limb darkening effect.

Thus the wavelength at which disk intensity profile changes from limb darkening to limb brightness provides a means to locate the height of the photospheric temperature minimum layer.

2.15 Solar differential rotation

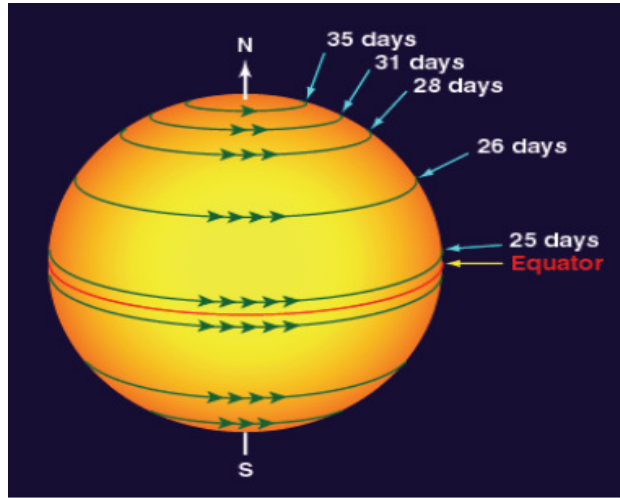


Figure 14: Solar Differential rotation

- Photosphere does not rotate as a solid body
- Rotates faster at equator than at the high latitudes
- Differential rotation coupled with solar magnetic fields are key to several observational activities

Spectroscopy using the Doppler effect (discovered in 1872) provided earliest measurements of solar sidereal rotation rate.

$$\Omega = A + B\sin^2\theta + C\sin^4\theta \text{ degree/day} \quad (2.4)$$

where θ is solar latitude, such that

$$A = \Omega \text{ at the equator} \quad (2.5)$$

and

$$A + B + C = \Omega \text{ (at poles)} \quad (2.6)$$

One model gives

$$\Omega = 14.38 - 2.7\sin^2\theta \text{ degree/day} \quad (2.7)$$

2.16 Solar magnetic fields

- Our present day understanding of solar magnetic fields dates back to 1908 when G.E. Hale made the first magnetic field observations of sunspots.
- However, systematic mapping of the Sun's magnetic field began only after 1952, carried out by the Babcocks , that the true nature of solar magnetic activity became apparent.
- Turns out that the sunspots (active regions in 3D) are islands of intense magnetic fields as compared to ambient or surrounding photosphere.

2.17 Measurement of B by line-splitting (Zeeman Effect)

If there are magnetic fields present, the atomic energy levels are split and the spectral lines are also split. The amount of splitting is a signature of magnetic field strength.

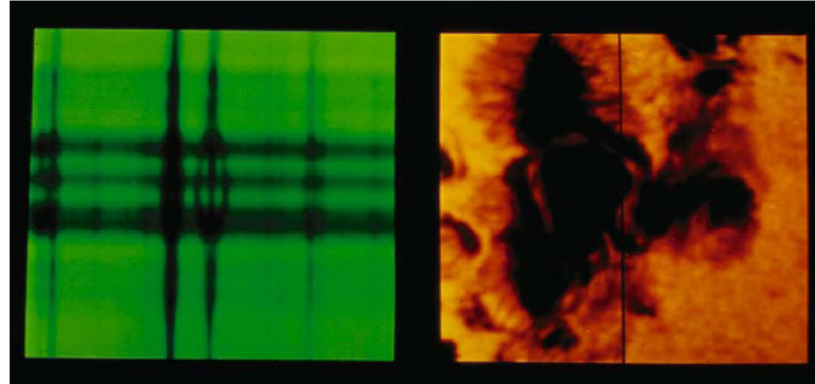


Figure 15: Line splitting usually small to measure even for strong fields! However, magnetic fields cause polarization , which can be measured to infer magnetic fluxes.

$$\begin{aligned}
 E &= h\nu = \frac{hc}{\lambda} \\
 \Delta E_M &= \frac{hc}{\lambda^2} \Delta\lambda_M \\
 \Delta E_M &= \frac{1}{2} \left(\frac{e h B}{2\pi m_e} \right) M_J g \\
 \Rightarrow \Delta\lambda_M &= \frac{1}{2} \left(\frac{e h}{2\pi m_e} \right) \frac{B M_J g \lambda^2}{hc} \\
 &= 4.67 \times 10^{-13} M_J g \lambda^2 B
 \end{aligned} \tag{2.8}$$

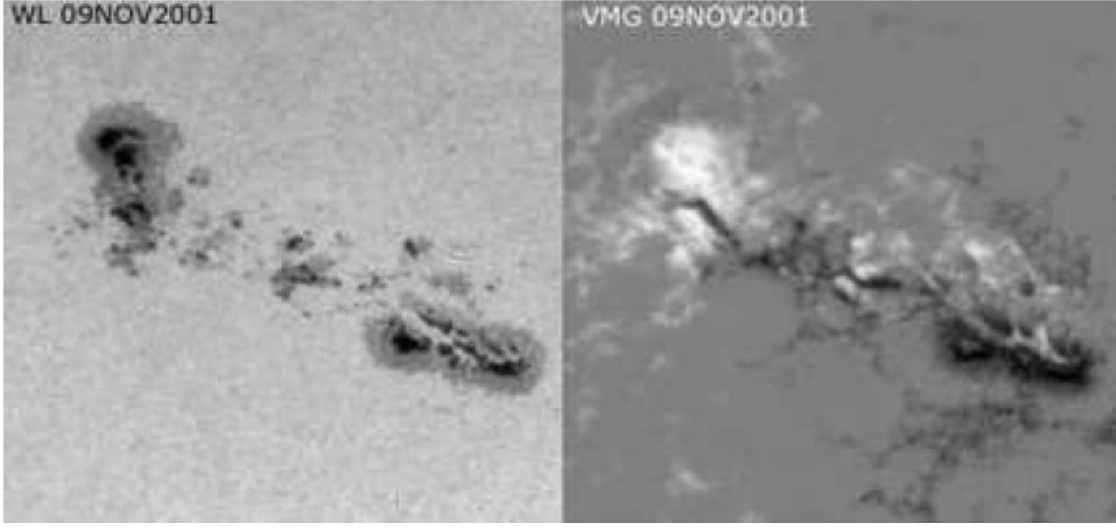
$$\text{For } r M_J g = 1, \lambda = 7000 \text{ \AA}, \Delta\lambda_M = 0.1 \text{ \AA} \Rightarrow B = 4370 \text{ G}.$$

Sunspots are the seats of strong magnetic fields. This is the reason why they appear dark compared to ambient medium. From energy conservation one has:

$$P_s + \frac{B^2}{8\pi} = P_0 \Rightarrow P_s < P_0 \Rightarrow T_s < T_0 \tag{2.9}$$

High resolution magnetic image of solar photosphere shows magnetic structure, and polarity distribution of sunspot and its surroundings. Full disk magnetograms are regularly obtained from ground and space. Sunspots at photosphere are only the 2D footpoints (cross-section) of a 3D flux system of overlying atmospheric layers.

Strong magnetic flux tubes are formed in a very thin layer (tacocline) just below the convective zone. Local instabilities allow such flux tubes to emerge into the convective zone.



Pressure in the flux tube is the sum of its gas- pressure p and magnetic pressure $\frac{B^2}{8\pi}$. This must balance the ambient pressure p_0 (assuming negligible B_0), so that

$$p + \frac{B^2}{8\pi} = p_0 \quad (2.10)$$

As $\frac{B^2}{8\pi}$ is strictly positive, $p < p_0$. Assuming similar temperatures throughout requires that flux tube mass density $\rho < \rho_0$ (ambient).

Thus flux tube experience a positive buoyancy force and floats up from the base of CZ. Simulations estimate escape time for a flux tube to reach the surface is of the order of a month.

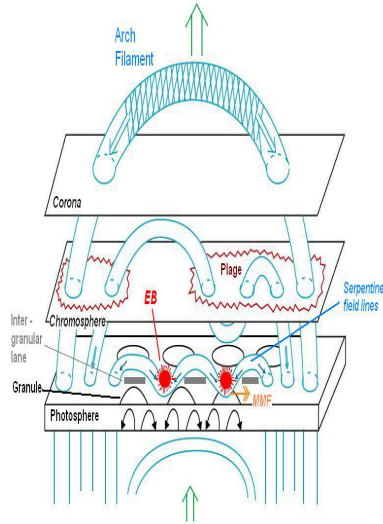


Figure 16: Why does the Flux Tubes Rise from solar interior?

2.18 Chromosphere $\sim 2500\text{km}$ thick layer, hotter $T > 10,000K$

Above the 1000s times brighter photosphere lies a fainter, normally invisible layer , optically transparent in visible wavelengths. Bright photosphere is directly seen through the rarefied faint chromosphere.

This layer is seen briefly as a thin red layer of gases just before (and after) the totality of solar eclipses when bright photosphere is just covered by moon. Name derived from the bright red color displays viewed on the limb during a solar eclipse due to $H\alpha 6562.8\text{\AA}$ emission.

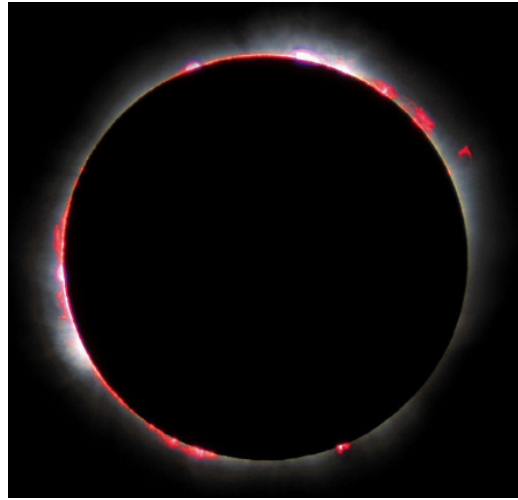


Figure 17: total solar eclipse of Aug 11, 1999. Photo by Luc Viatour

2.19 Observing chromosphere on and off disk without Solar Eclipse

Chromospheric spectral lines briefly show up as flash spectrum during TSE. Optical narrow band

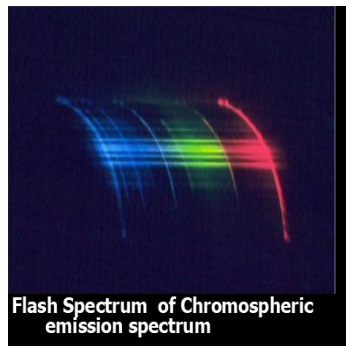
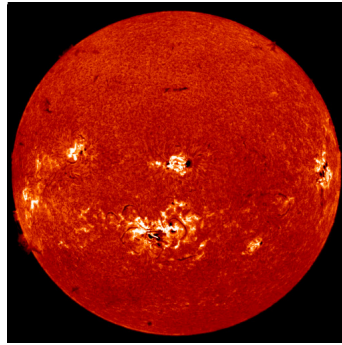


Figure 18: Flash Spectrum of Chromospheric emission spectrum

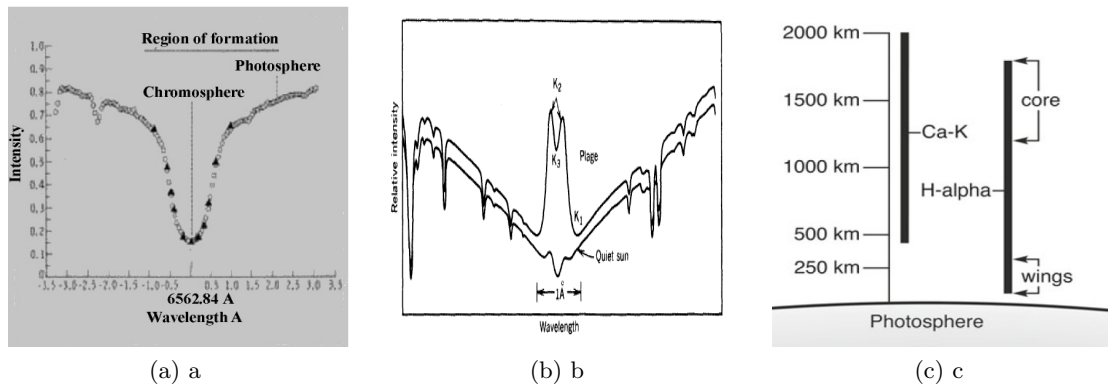
filters in $H\alpha$ (red line) 6563\AA , or singly ionised CaII K 3934\AA (blue line), are used to block intense

photospheric light.

Not just the limb (as during TSEs) but on disk, chromosphere can be spectrographically observed on a routine basis.



2.20 Regions of formation of chromospheric lines ($H\alpha$ and Ca K)



- a: $H\alpha$ absorption line. It is exceptionally strong line. Contributions to $H\alpha$ line span from the photosphere (in the line wing) up to the upper chromosphere (in the line core).
- b: Profiles of the Ca K-line of the quiet Sun (lower curve) and of a plage region (upper curve).
- c: Most Fraunhofer lines are weaker, and are formed entirely below the temperature minimum in the photosphere

2.21 The chromosphere

- Magnetic pressure begins to dominate plasma pressure (β no longer too large.)
- So, it is highly structured by magnetic field. Dynamics begins to be guided by magnetic Fields.

- Not just sunspots and granules, but a whole lot of other features can be seen: "spicules", "plage", "filaments", prominences, etc.

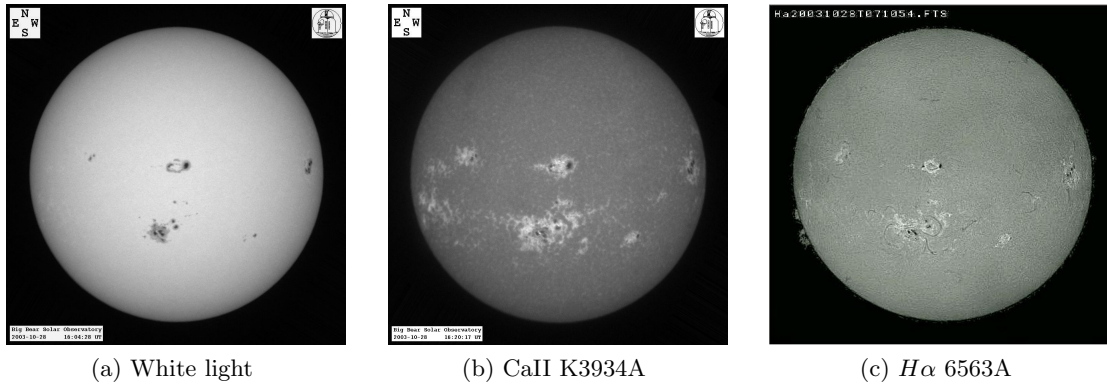
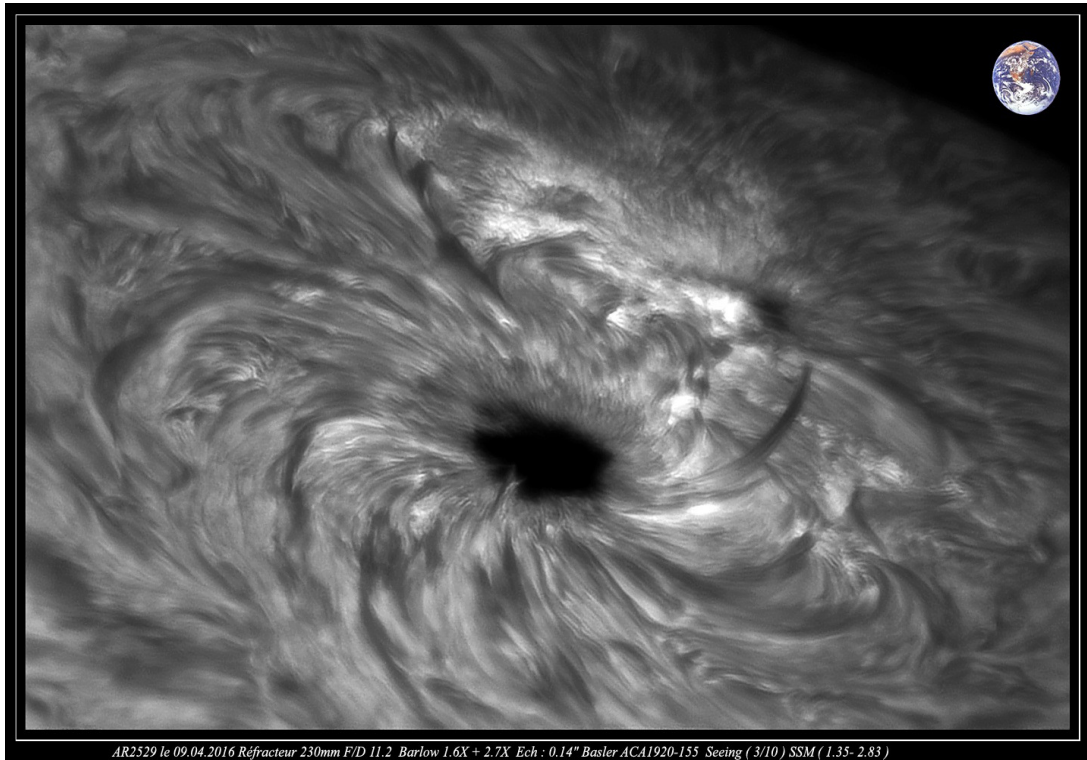
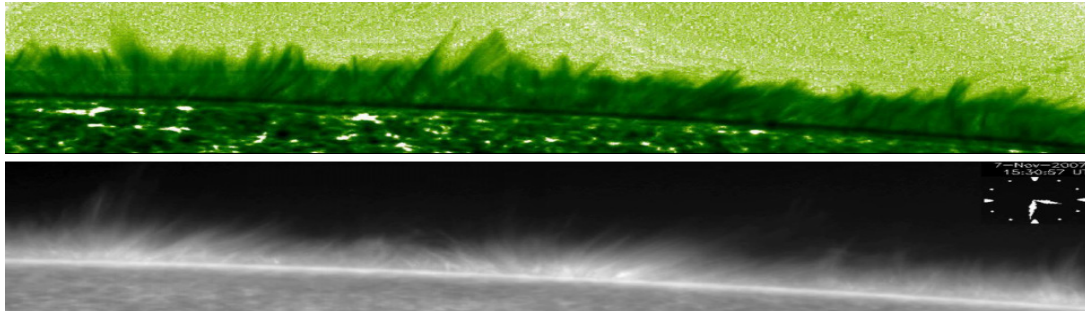


Figure 19: The photosphere, lower chromosphere and upper chromosphere

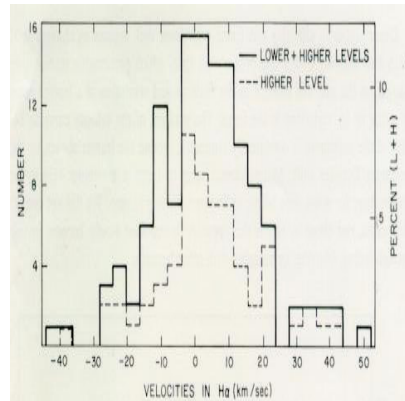


A high resolution filtergram of an active region (AR), consisting of a large sunspot surrounded by lot of structures which show the influence of sunspot's magnetic fields... also bright plage (French for beach) which marks hotter region with flux of opposite magnetic polarity.

2.22 Spicules: small, jet-like eruptions



The solar surface is covered with "grass blades" known as spicules. Typical diameters are 500km. They eject material into the hot corona at speeds of 20–30 km/s, reaching $\sim 5,000\text{km}$ above the photosphere, and last 5–10min. Limb images best illustrate their geometry. However, they occur throughout the disk.

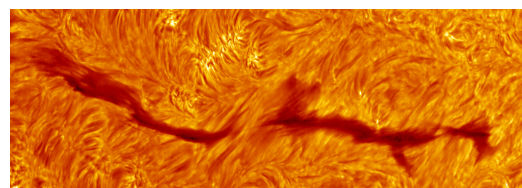


2.23 Solar prominences/filaments

Dense ($n \sim 0 : 5 - 1.0 \times 10^{-3} \text{ m}^{-3}$), cooler gas clouds (5000 – 10 000 K), seen on the limb, but appear as dark, thin and long ribbons or filaments on disk. Typical thickness, height, and length are 5000 km, 50,000 km, and 200,000 km, respectively. The prominences protrude far above the chromosphere, surrounded by 100 times hotter, 500 times lower density coronal matter. However, prominences remain stable for weeks.



(a) a



(b) b

- a: as the connection is gradually lost due to magnetic flux evolution, eventually the balance is lost and prominence may erupts.
- b: Prominences/filaments are anchored to chromospheric layer at supergranulation cell boundaries through footpoints or barbs.

2.24 Filament disappearance events – disparition brusques

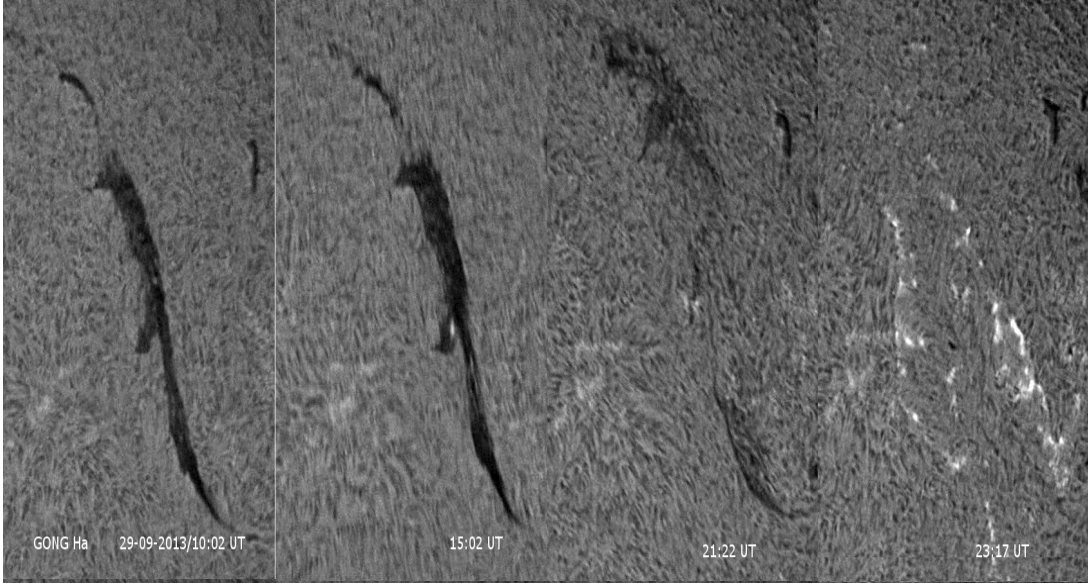


Figure 20: Time evolution and disappearance of filaments observed during 29 September 2013 (GONG H-alpha images)

2.25 The white light Corona

Coronal dynamics and properties are dominated by the solar magnetic field:

$$\beta = \frac{P_G}{P_B} = \frac{2nkT}{B^2/8\pi} \ll 1 \quad (2.11)$$

Above transition region (not observed from ground), temperature increases more slowly with distance, up to several million K, as the density further decreases. The corona, in white light appears due to scattering of photospheric photons by fast moving coronal electrons, but it is million times fainter compared to photosphere. So it is revealed from ground only when photosphere is fully covered during TSE. In addition, other forms of coronal emissions are also produced in the optically thin outer atmosphere, observed close to the Sun's limb during TSE, and from space. Further out, the reddened sunlight scattered from dust particles combines with the zodiacal light at great distances from the Sun. The plasma frequencies of corona can be observed in radio wavelengths too (without the need for eclipse).

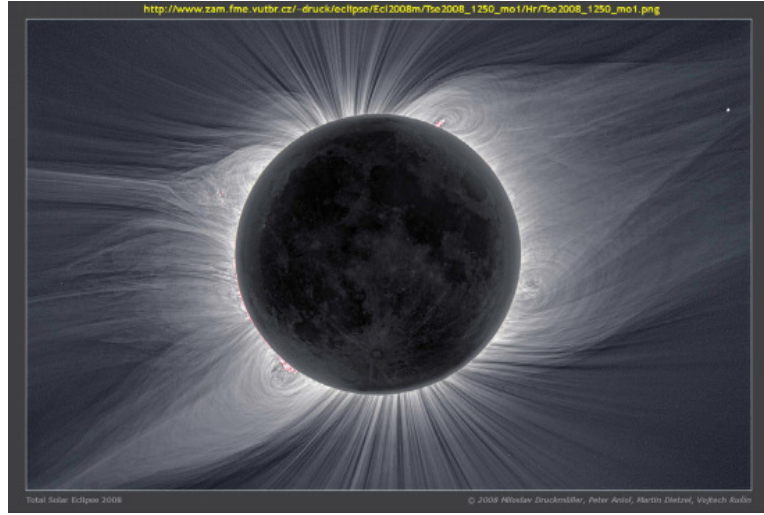


Figure 21: The white light Corona

2.26 Discovery of a million-degree temperature of the corona

C.A. Young and W. Harkness obtained the spectrum of solar corona during a TSE in 1869, and discovered an emission line corresponding to Fe XIV 530.3 nm in corona. Helium (2nd most abundant element) was first discovered spectroscopically during TSE 1868 observed from India. Emission lines from the chromosphere ($H\alpha$, $H\beta$, helium D_3 and others), and two emission lines

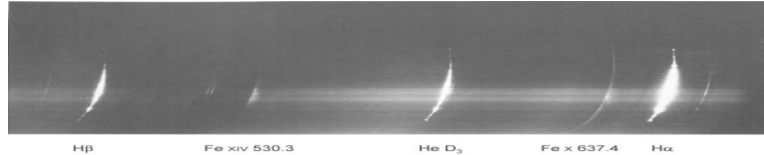


Figure 22: Coronal mission spectrum — 1970 solar eclipse (Kyoto University's TSE expedition)

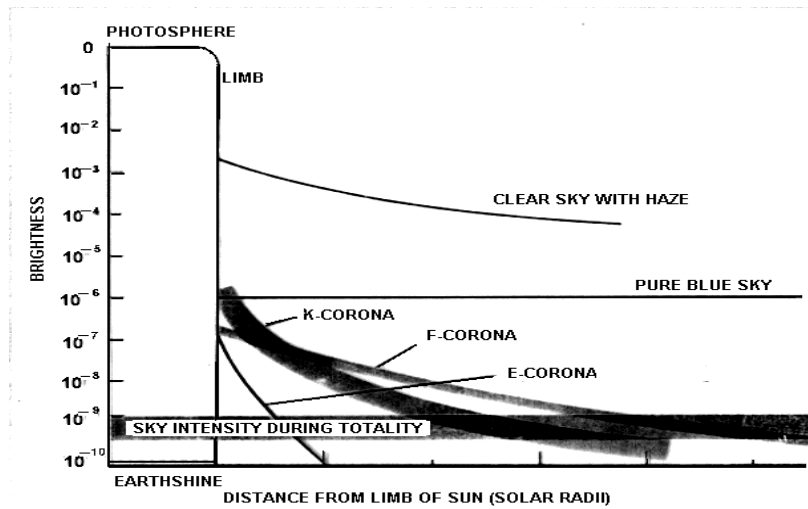
of coronal origin are seen in red (637.4 nm) and green (530.3 nm) wavelengths; these forbidden lines are the strongest coronal emission lines in visible wavelengths. These forbidden lines of highly ionized atomic species, such as, Fe XIV 530.3 nm, in emission spectra during TSEs indicate coronal temperature of 2×10^6 K required to ionize Fe. Dozens of other coronal emission lines are known now.

2.27 The Emission Line Corona

The coronal gases super-heated to $T > 10^6 K$, so that H & He completely ionized, including elements like C, N, O. Only heavier trace elements like Fe and Ca able to retain a few electrons. Emission from these highly ionized elements produces the mysterious spectral emission lines not known to early astronomers. Artificial eclipses in coronagraphs show corona in these coronal emission lines.



2.28 The corona and coronal emission



2.29 Radio emission from solar plasma

- Radio wavelengths $> 1\text{mm}$. Frequency is often used to characterize radio emissions, such that $\lambda(m) = 300/f(\text{MHz})$. Thus, e.g., $\lambda(1\text{mm}) = f(300\text{GHz})$.
- Radio emissions occur in perturbed plasma layers of the solar atmosphere in plasma frequency and are mainly due to free electrons moving in the magnetized plasma

$$f_{pe} = \frac{1}{2\pi} \sqrt{\frac{n_e e^2}{\epsilon_0 m_e}} \quad \text{or} \quad f_{pe} (\text{Hz}) \sim 9 \times \sqrt{n_e (\text{m}^{-3})} \quad (2.12)$$

Chromosphere: electron density drops from $2 : 5 \times 10^{17}\text{m}^{-3}$ to 10^{16}m^{-3} \Rightarrow correspond to plasma frequencies 4.5 GHz – 0.9 GHz (6.7 – 33.3 cm).

Corona: electron density varies with γ as

$$n_e = (1.55r^{-6} + 2.99r^{-16}) \times 10^{14} \quad (2.13)$$

where r is in solar radii, density in m^{-3} .

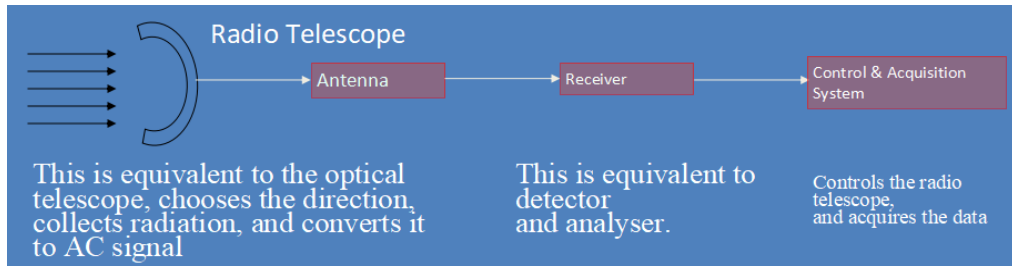
This gives at $2R_s$, plasma frequency ~ 14 MHz (21 m). The energy density in radio waves is extremely small for astronomical objects, and measured in Jansky:

$$1 \text{Jy} = 10^{-26} \text{W Hz}^{-1} \text{m}^{-2} \quad (2.14)$$

In solar astronomy, Solar flux unit (sfu) is used

$$1 \text{sfu} = 10^{-22} \text{W Hz}^{-1} \text{m}^{-2} = 10^4 \text{Jy} \quad (2.15)$$

2.30 Observing in radio wavelengths



- Advantage: clouds, dust no hindrance for radio waves
- Drawback: lower spatial resolution because $\lambda_{radio} (\sim cm - m)$ while $\lambda_{optical} \sim 100nm$, therefore, for same resolution α as for $D = 1m$ optical telescope, we need $D \sim 20km$ aperture for radio wavelength.
- Radio telescopes are linked over large distances to create a diameter of thousands of km for better resolutions.
- Detection of radio signal: By alternating electromagnetic field excited by radio waves in the detector, detected electronically as an AC voltage:

$$V = V_0 \sin(\omega t - \varphi) \quad (2.16)$$

Amplitude V_0 and phase ϕ of this voltage is analysed.



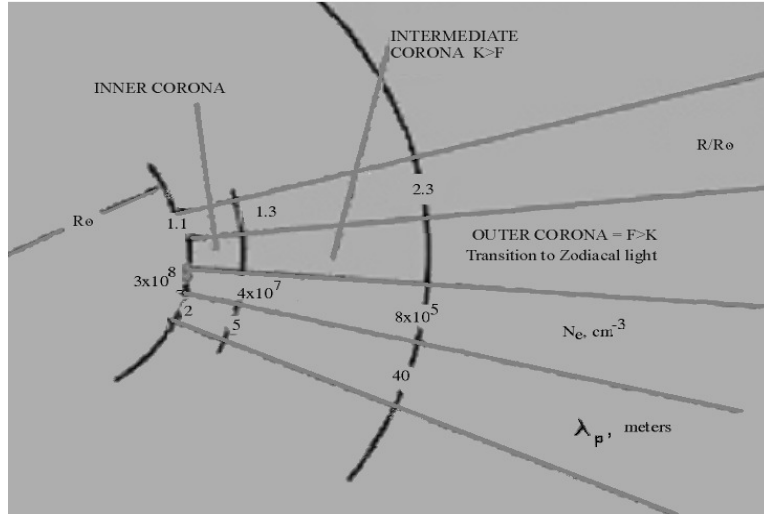
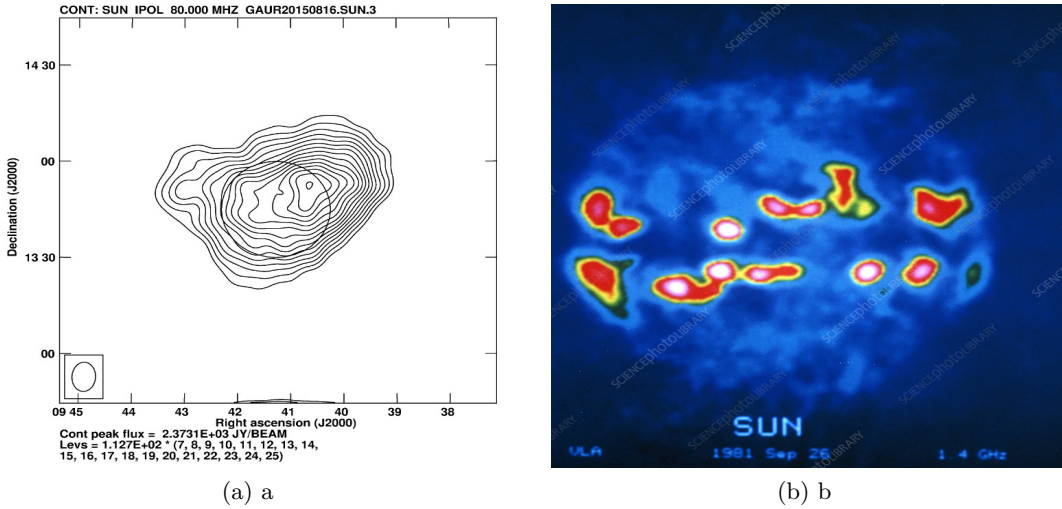


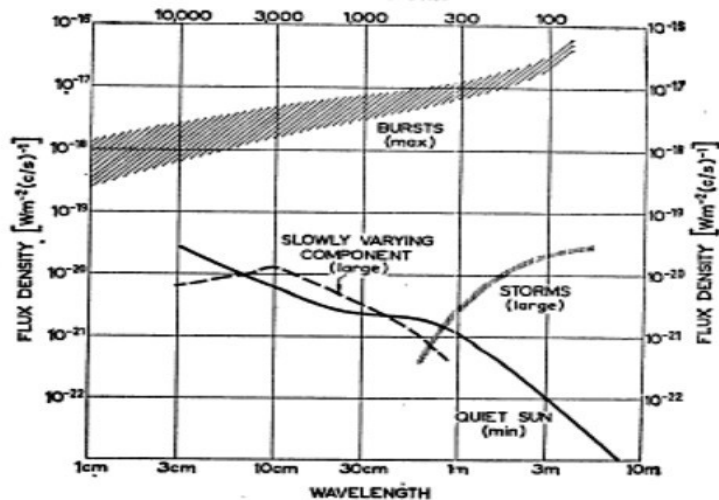
Figure 23: Radio sun is much bigger than the optical sun



- a: Radio Sun at $\lambda 20cm(80MHz)$, by Gauribidanur Radio Heliograph near Bengaluru (India) — operated by Indian Institute of Astrophysics (IIA).
- b: Radio Sun at $\lambda 20cm(1.4GHz)$, by VLA, New Mexico. Bright region around solar equator: hot, dense coronal plasma above sunspots. Dark blue regions: coronal holes, of low density. Resolution 40 arcsec.

2.31 Radio spectrum: The longer end of solar spectrum

Sun is strongly variable at radio wavelengths. The reason for this variability is that the radio emissions originate from non-thermal plasma processes (synchrotron process). During strong solar disturbances the radio emissions can exceed the quiet levels by several orders of magnitude. The slope at longest wavelenghts for quiet Sun corresponds to higher temperatures than the main black body radiation. This tells that the chromosphere and corona are much hotter than the Sun itself.



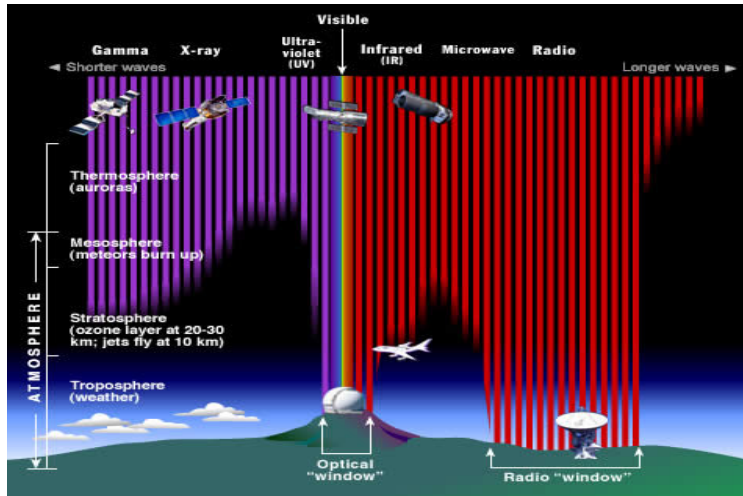
Solar radio emissions. Dots and the solid curve represent the quiet Sun, the dashed line (S-comp.) is a slowly varying component correlated to the solar cycle, and the dotted lines illustrate the rapidly varying events in the solar atmosphere.

2.32 Solar radio telescopes

- Nançay Radioheliograph (NRH), France: interferometer composed of 48 antennas observing at meter-decimeter wavelengths.
- Owens Valley Solar Array (OVSA), California, USA: radio interferometer operated by the NJIT observing from 1 to 18 GHz.
- Nobeyama Radioheliograph (NoRH), Japan: interferometer formed by 84 small (80 cm) antennas, with receivers at 17 GHz and 34 GHz.
- Siberian Solar Radio Telescope (SSRT): Operates at microwave range (5.7 GHz) to observe solar activity processes I solar corona.
- Solar Submillimeter Telescope, Argentina: a single dish telescope observing the Sun at 212 and 405 GHz.
- Bleien Radio Observatory, Switzerland: A set of telescopes observe solar flare radio emission from 10 MHz (ionospheric limit) to 5 GHz. The broadband spectrometers are Phoenix and CALLISTO (also having its network around the world)
- Ooty Radio Telescope, India: 530m long 30 m wide Cylindrical Paraboloid steerable Radio telescope at 327 MHz (0.92m) radio scintillations to infer IPM
- Giant Meterwave Radio Telescope (NCRA), India: array of 30 steerable parabolic radio telescopes of 45 metre diameter, observing at \sim metre wavelengths (327 MHz).
- Gauribidanur Radio Heliograph, India – solar radio images at 40 – 150 MHz

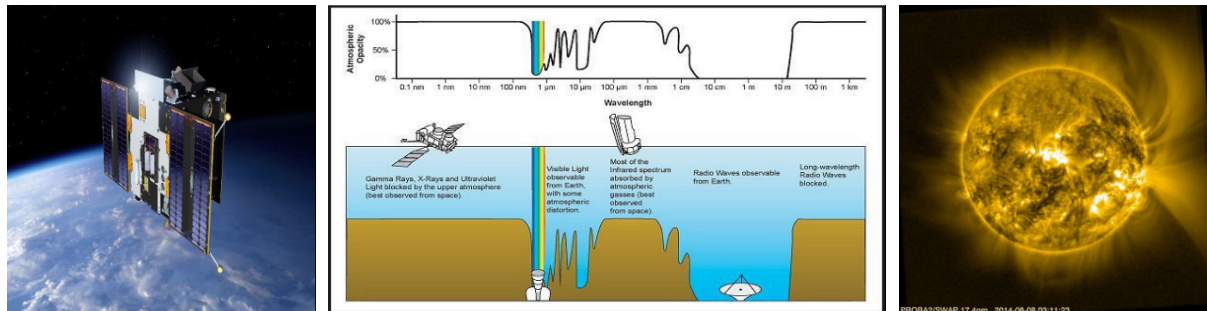
3 Space-borne observations of the Sun

3.1 Sun's (star's) radiation passage through the Earth's atmosphere



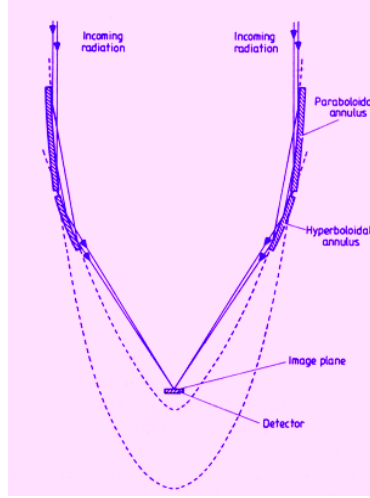
3.2 Space telescopes for observing the Sun in high energy emission

UV, X-ray, gamma-rays do not penetrate to ground: Must therefore go to space. Costly to fly large telescopes. Outside Earth's atmosphere, so no "seeing" effects from atmosphere.

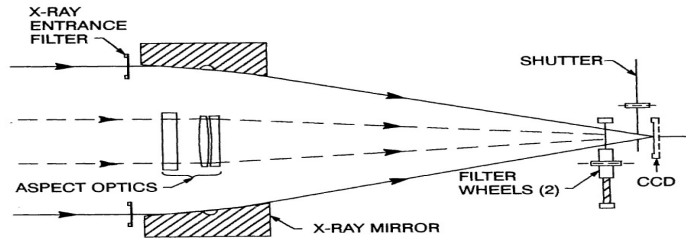


3.3 Observation X-ray wavelengths

- X-rays too energetic to be reflected at normal incidence; conventional telescope cannot be used except for very soft x-rays.
- Grazing incidence relaxes the requirement of surface accuracy of the optics by a factor of sine of the grazing angle. $\gamma - rays$ are too energetic for even grazing- incidence telescopes to work. They rely on mechanical collimation (soft $\gamma - rays$) and particle track analysis for hard $\gamma - rays$.



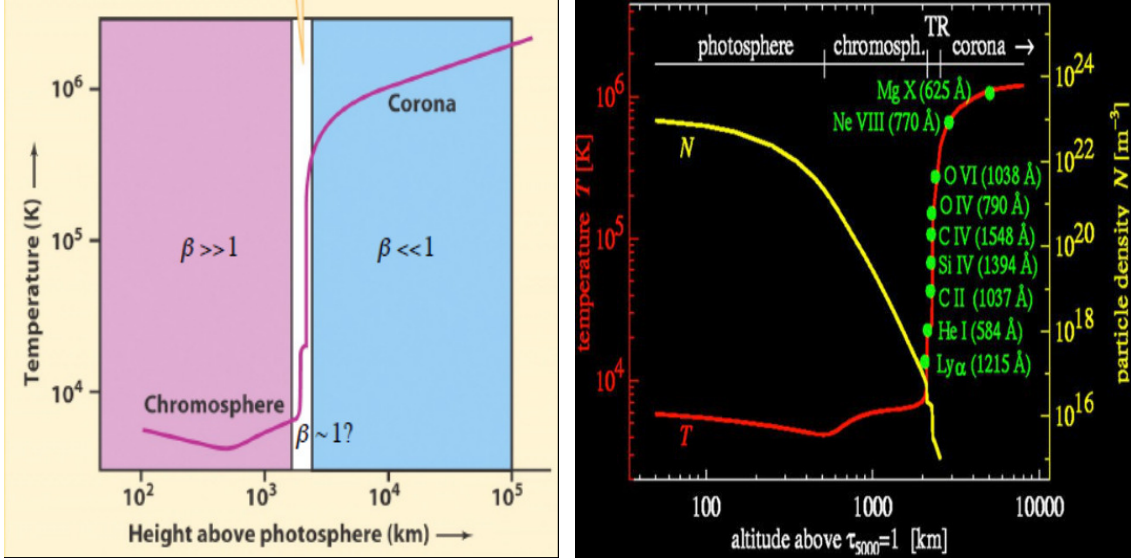
Wolter-type grazing incidence X-ray telescope. X-rays far from the axis are brought to focus after successive grazing-incidence reflections $< 2^\circ$



Schematic of Yohkoh SXT based on Wolter-type grazing incidence X-ray telescope.

3.4 The transition region (TR)

- Moving above the chromosphere, temperature increases rapidly from $\sim 20,000^\circ K$ to $10^6^\circ K$ within a short height span of around a few hundred kms. Density falls too.
- TR separates the hot corona from the cooler chromosphere.
- The increase in temperature is much more than the radiative heating of the chromosphere: one of the outstanding problems in solar physics.
- The million degrees temperatures of the outermost hot plasma is adequate to ionize hydrogen so it is difficult to observe in $H\alpha$.
- TR is dominated by ionized elements such as C IV, O IV, and Si IV (each with three electrons stripped off), and emits UV, and EUV.
- R can thus only be observed from space.



3.5 The prime ions observed by SDO-AIA

Atmospheric Imaging Assembly (AIA) on-board Solar Dynamics Observatory (SDO) launched on 11 February 2010 provides simultaneous full-disk images of the corona and transition region up to $0.5 R_\theta$ above the solar limb. Narrow-band imaging of seven extreme ultraviolet (EUV) band passes centered on specific lines. EUV emissions cover the range from $6 \times 10^4 K$ to $2 \times 10^7 K$. Also C iv (near 1600 \AA) and the nearby continuum (1700 \AA).

Channel(Å)	Primary Ions(s)	Region of Atmosphere	Char.Log(T)
4500	Continuum	Photosphere	3.7
1700	Continuum	Temperature minimum, Photosphere	3.7
304	He II	chromosphere, transition region	4.7
1600	C IV-cont	transition region, upper photosphere	5.0
171	Fe IX	quiet corona, upper transition region	5.8
193	Fe XII,XXIV	corona and hot flare plasma	6.2,7.3
211	Fe XIV	active region corona	6.3
335	Fe XVI	active region corona	6.4
94	Fe XVIII	flaring corona	6.8
131	Fe VIII,XXI	transition region, flaring corona	5.6,7.0

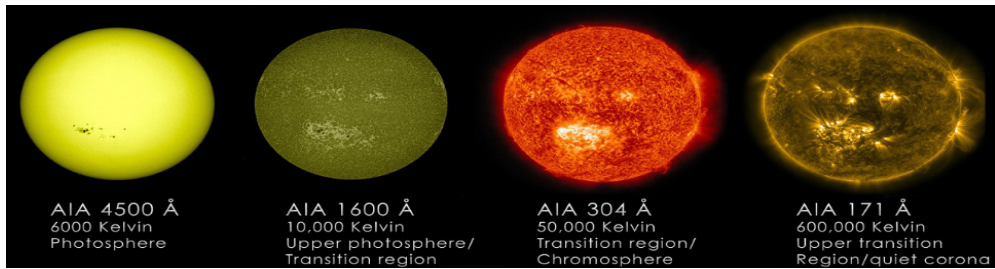
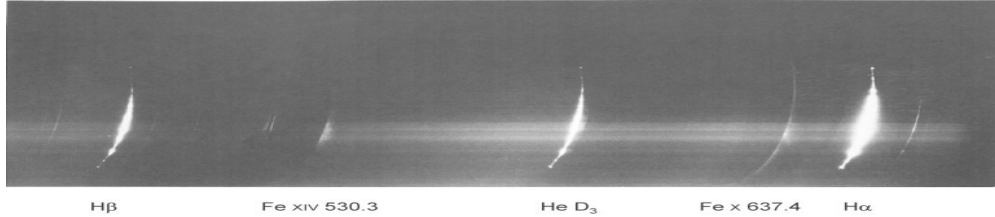


Figure 24: Some images of Transition Region by SDO–AIA

3.6 Discovery of a million-degree temperature of the corona

The corona is the outermost atmosphere of the Sun, traditionally observed during total solar eclipses. Spectrum of solar corona was obtained during a TSE in India in 1868 when He was discovered. In a TSE observed from North America in 1869 an emission line corresponding to Fe XIV 530.3 nm in corona was found \Rightarrow require extremely high, million degrees K to ionize Fe. Coronal mission spectrum at the solar eclipse of 1970 (Kyoto University's eclipse expedition



photographed). This coronal spectrum: Emission lines from chromosphere ($H\alpha$, $H\beta$, helium D_3 and others), two emission lines of coronal origin in red (637.4 nm) and green (530.3 nm) wavelengths; these forbidden lines are the strongest coronal emission lines in the visible wavelengths, although currently dozens of other coronal emission lines are known.

3.7 Forbidden lines seen in Coronal emission spectrum: signifies high temperature and low density

- The wavelengths of these coronal emission lines did not match those from elements known in the 19th century, and their origin had been a mystery. Bright emission lines at wavelengths not corresponding to any known materials. "coronium"?
- In 1930s, studies of UV emissions from highly excited ions in spark discharge experiments inferred energy levels of FeX (with 9 of its 26 electrons stripped off)
- Grotrian noticed a possible transition having wavelength matching red coronal line (637.4 nm). This transition is a forbidden transition, as the transition takes very long time under laboratory conditions where density of gases is high. Thus emission due to this transition does not take place due to collisions with particles
- In a tenuous gas like the solar corona, collisions are infrequent and ions have long-enough time for such forbidden transitions to take place
- A series of experiments identified the origins of many coronal lines. The coronal green line was identified as due to Fe XIV
- Forbidden lines corresponding to highly ionized FeX or FeXIV indicate high temperatures of corona at 2×10^6 K

3.8 The corona and coronal emission

The corona and coronal emission:

1. K-Corona (Kontinuierlich)
 - (a) Polarised light
 - (b) Dominates in the inner region ($R < 1.5R_o$)
 - (c) No Fraunhofer lines
 - (d) Arises from Thomson scattering on rapidly moving free-electrons Observations:
 - TSE
 - space-based coronagraph
2. E-Corona (Emission)
 - (a) Emission of radiation by highly-ionized species in the actual corona
 - (b) Observations: From space in EUV and X-rays
3. F-Corona (Fraunhofer)
 - (a) Unpolarised
 - (b) Dominates in $2-3 R_o$
 - (c) Dark Fraunhofer lines
 - (d) Arises due to scattering of photospheric light on interplanetary dust
4. T-Corona (Thermal): Thermal (largely IR) emission of interplanetary dust.

3.9 Artificial solar eclipse from space: Coronagraph in space for large scale structure of Sun's corona

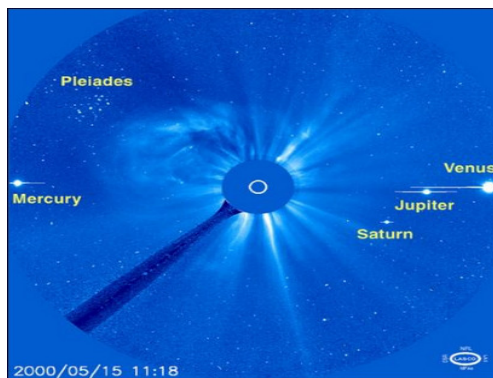


Figure 25: Large Angle and Spectrometric Coronagraph on-board SOHO

3.10 The emission line Corona

The coronal gases super-heated to $T > 10^6 K$, so that H & He completely ionized, including elements like C, N, O. Only heavier trace elements like Fe and Ca able to retain a few electrons. Emission from these highly ionized elements produces the mysterious spectral emission lines not known to early astronomers. Artificial eclipses in coronagraphs show corona in these coronal emission lines.



3.11 Corona in X-rays

A consequence of the corona's high temperature is that it has a large scale height, which means its density drops very slowly with radial distance. Thus, EUV and X-ray emissions come from an extended but optically thin envelope that can reach a significant fraction of a solar radius out from the photosphere. Coronal holes and X-ray bright points were discovered only in early 1970s from space-borne instruments. Later Yohkoh (Solar-A), Hinode, SOHO and TRACE, RHESSI, SDO satellites have followed. Coronal holes are SOURCE of Fast Solar Wind.

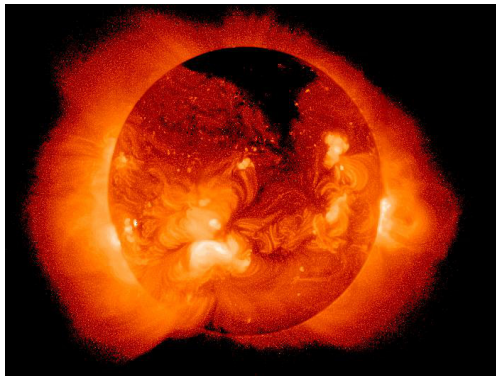


Figure 26: The X-Ray Corona

Coronal emissions are seen against the backdrop of the much cooler and thus dark photosphere.

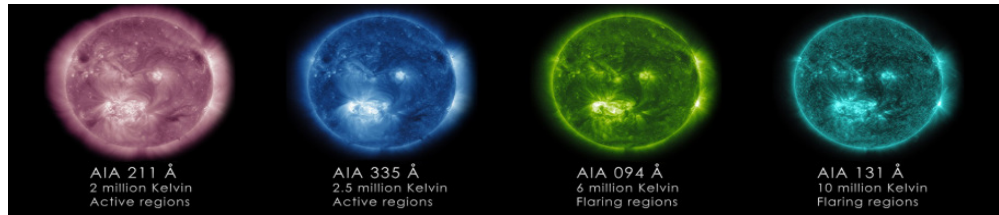


Figure 27: Some images of Corona by SDO–AIA

3.12 The magnetized corona

The corona is highly structured, active and variable. The structures observed in Sun's outer layers highlight dominance of magnetic fields in solar atmosphere.

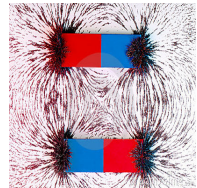
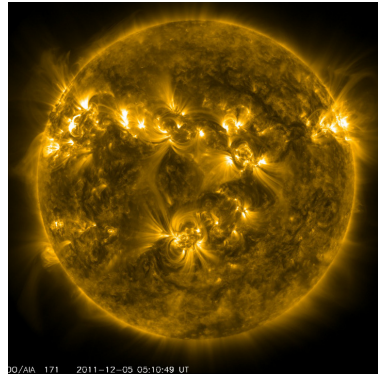
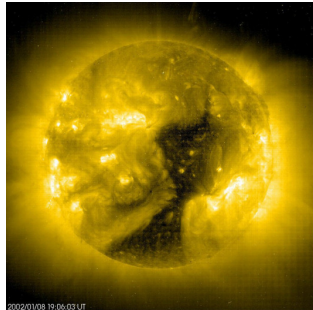


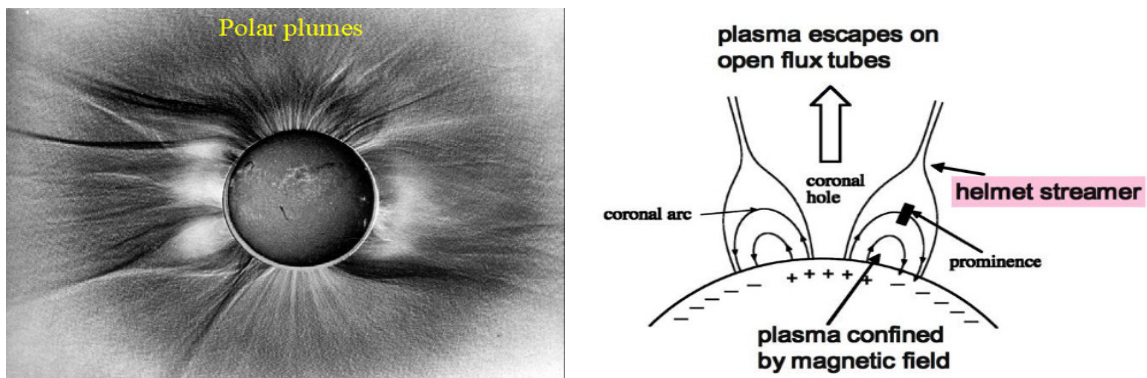
Figure 28: Magnetic fields drive the explosive events

3.13 Coronal holes: sources of fast streams of solar wind



In coronal holes, magnetic field lines are 'open', therefore, they are associated with high speed solar winds stream.

3.14 Helmet streamers and polar plumes



Helmet Streamers: large closed cap-like structures with long pointed peaks usually overlying active regions. Field lines associated with coronal loops, helmet streamers, active regions and prominences are closed : difficult for plasma to escape. Closed magnetic fieldlines trap coronal plasma, while pointed peaks formed by solar wind blowing away in the space as streamers into space. **Polar plumes:** long thin streamers projecting outward from the Sun's N- & S- poles.

3.15 Why and how is the corona heated to million degrees? – An outstanding problem

What causes the corona to be so hot is one of the most vexing problems in astrophysics. Density of the corona (10^{8-9} cm^{-3}) is much smaller than that of the photosphere (10^{17} cm^{-3}) which has $T_{eff} \sim 5770K$ only. Therefore, the thermal energy density of the corona (although it is 200–300 times hotter than the photosphere) is negligibly small compared with the photospheric energy density. Due to the second law of thermodynamics, heat cannot flow from the photosphere (lower T) to the corona (higher T) to raise the coronal temperatures. However, there is no plausible source

of energy further out in the corona to heat up the corona, we must assume that some form of energy other than heat is supplied from below the corona to realize its million-degree temperature.

3.16 Heating mechanisms for solar corona

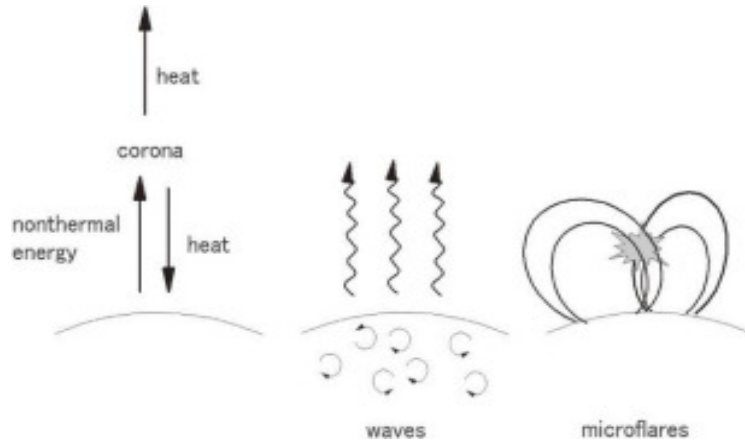


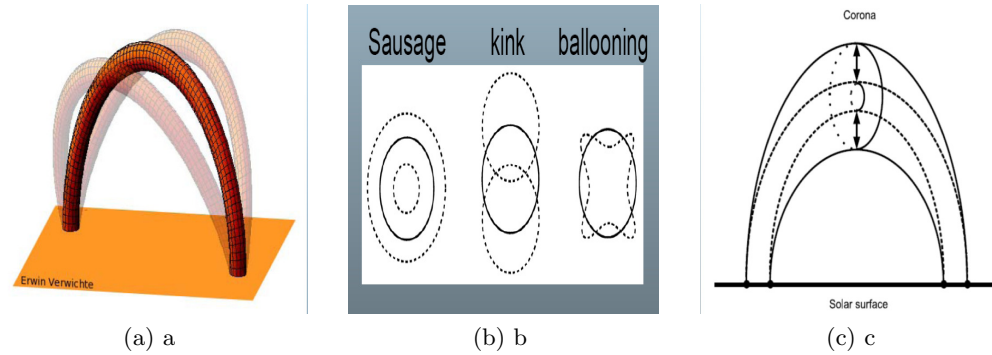
Figure 29: Energy flows to/from the corona (left), and two representative heating mechanisms.

Currently there are two classes of mechanisms: MHD Waves (acoustic and magnetic), Magnetic reconnections: microflare/nanoflare theory. Both models have merits and disadvantages, but the essential issues are nearly pinned down. Acoustic waves (observed at photosphere) do not reach far into the chromosphere, before steepening to shocks in rapidly decreasing density regions. Slow mode magneto-acoustic waves can propagate further but again they too form shocks and dissipate in the chromosphere. Fast modes, however, manage to reach transition region between chromosphere and corona, and they either dissipate (heat) or get reflected back. More recently, there are evidences of coronal waves detection, and also that they may carry adequate energy to heat the corona.

3.17 Coronal seismology

- Exploits observed coronal oscillations as a diagnostic tool for determining the physical conditions of the coronal plasma (density, magnetic field strength).
- Requires high-quality observations of coronal oscillations =; SoHO and TRACE observed in coronal loops, polar plumes and prominences.
- Relevance in wave heating of corona
- MHD wave theory forms the basis for coronal seismology
- Coronal seismology is rapidly being transformed from a theoretical possibility to a viable technique.

3.18 Coronal oscillations



1. Standard model – MHD modes of a straight plasma cylinder (effects such as loop curvature, density variation, field twisting, nonlinearity ignored).
 2. Azimuthal mode number:
 - $m = 0$: sausage (or radial) mode
 - $m = 1$: kink modes
 - $m > 1$: flute or ballooning modes
 3. Fast (predominantly transverse) and slow modes (predominantly longitudinal)
 4. Propagating and Trapped MHD modes
 5. Apart from m , there are two other mode numbers associated with standing MHD modes: radial number l and longitudinal wave number n .

3.19 UV observation of oscillating magnetic structures: Flare shakes the coronal loop

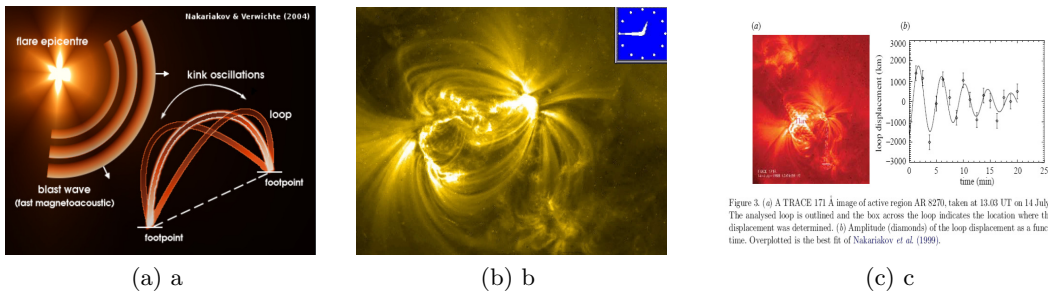


Figure 3. (a) A TRACE 171 Å image of active region AR 8270, taken at 13:03 UT on 14 July 1998. The analysed loop is outlined and the box across the loop indicates the location where the loop displacement was determined. (b) Amplitude (diamonds) of the loop displacement as a function of time. Overplotted is the best fit of Nakariakov *et al.* (1999).

The transverse (kink or $m = 1$) oscillations of the coronal loops are induced by a nearby flare and appear to be heavily damped – Aschwanden et al. (1999, 2002). The waves are identified as impulsively generated, standing, fast magnetoacoustic kink modes: periods $p = 5.4 \pm 2.3$ min, damping time $t_d = 9.7 \pm 6.4$ min, and amplitude of loop displacements $A = 2200 \pm 2800$ km, with maximum transverse velocities $v_{\max} = 42 \pm 53$ km s $^{-1}$.

3.20 A static model of Corona with thermal conduction (Chapman 1957)

Coronal heat flux is related to temperature by

$$q = K \nabla T \quad (3.1)$$

where thermal conductivity is given by $K = K_0 T^{5/2}$. In the absence of heat sources or sinks, $\nabla \cdot q = 0$. Therefore, one has $\nabla \cdot (K_0 T^{5/2} \nabla T) = 0$

In spherical polar co-ordinates:

$$\frac{1}{r^2} \left(r^2 K_0 T^{5/2} \frac{dT}{dR} \right) = 0 \quad (3.2)$$

Separating variables and integrating:

$$\int T^{5/2} dT = \frac{C}{K_0} \int \frac{dr}{dr^2} \Rightarrow \frac{2}{7} T^{7/2} = -\frac{c}{K_0} \frac{1}{r} \quad (3.3)$$

Using the condition that $T = T_0$ at $r = r_0$, we have

$$r_0 T^{7/2} = -\frac{C}{K_0} \cdot \frac{7}{2} \quad (3.4)$$

Therefore

$$T = T_0 \left(\frac{r_0}{r} \right)^{2/7} \quad (3.5)$$

This gives $T = 2 \times 10^6 K$ at $r_0 = 1.05R$ (base of corona) and $T \sim 4 \times 10^5 K$ at $r = 214R$ or $1Au$, close to measured value. The equation 3.5 ensures that $T \sim 0$ as $r \rightarrow \infty$.

Assuming hydrostatic equilibrium, the momentum conservation equation is:

$$\frac{dP}{dr} = -g\rho \quad (3.6)$$

where plasma density $\rho = n(m_e + m_p) \sim nm_p$ (m_p = proton mass) and both electrons and protons contribute to pressure, so $P = 2nkT = \frac{2\rho kT}{m_p}$.

Substituting this we get

$$\frac{d \left(\frac{2\rho kT}{m_p} \right)}{dr} = -g\rho \Rightarrow \frac{2kT}{m_p} \frac{d\rho}{dr} = -g\rho \Rightarrow \frac{d\rho}{dr} = -g\rho \frac{m_p}{2kT} \quad (3.7)$$

This can be solved using derivative multiplication rule, and integrating to get

$$\rho(r) = \rho_0 \left(\frac{r}{r_0} \right)^{2/7} e^{\left[\frac{7}{5} \frac{GMm_p}{2kT_0 r_0} \left\{ \left(\frac{r_0}{r} \right)^{2/7} - 1 \right\} \right]} \quad (3.8)$$

which becomes

$$P(r) = P_0 e^{\left[\frac{7}{5} \frac{GMm_p}{2kT_0 r_0} \left\{ \left(\frac{r_0}{r} \right)^{2/7} - 1 \right\} \right]} \quad (3.9)$$

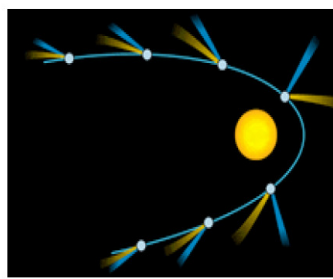
by substituting in Equation 3.8 $P = 2nkT = \frac{2\rho kT}{m_p}$. Equation 3.8 gives $\rho \rightarrow \infty$ and Equation 3.9 gives $P \rightarrow \text{constant}$ ($10^{-4} P_0 \gg P_{ISM} (10^{-15} P_0)$) as $r \rightarrow \infty$.

Thus, static model of corona is not correct. Corona is not static but must be dynamic and expanding!

3.21 Solar wind - historical hints from space of the I.P.M.

In the 50s Ludwig Biermann studying the phenomenon of the anti-solar acceleration of comet tails noticed that the standard explanation for the anti-solar orientation of comet tails (based on light radiation pressure) is inadequate to explain the observed outward acceleration of small inhomogeneities in comet tails.

This provided the evidence that solar wind is made of a corpuscular radiation



Type I: gases origin affected by solar wind



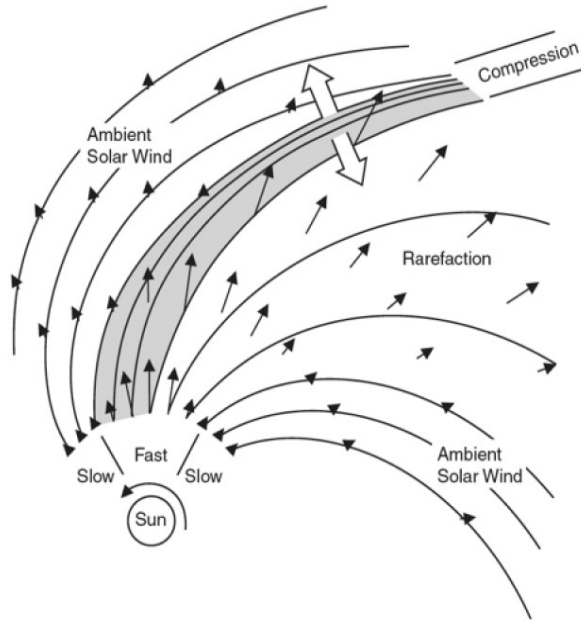
Type II: dust tail

Comet Hale-Bopp. Credit: Dimai & Ghirardo - Col. Druscic Obs., AAC

3.22 Solar Wind

Eugene Parker (1958) suggested that heat flowing from the Sun in Chapman's model and the comet tail blowing away from the Sun in Biermann's hypothesis had to be the result of the same phenomenon, a steady stream of particles that pushes the comet's tail away. He termed this stream as "solar wind". (Faced opposition but finally prevailed by space observations). Charged particle stream in all directions at mean speed ~ 400 km/s. Solar wind plasma - primarily hot electrons, protons with minor fraction of He^{2+} ions and other heavier ions (typically at high charge states). There are slow and fast solar wind streams in the range 300-800 km/s. Low speed winds come from helmet streamers, high speed winds come from coronal holes. These streams rotate as the Sun rotates (co-rotation) producing a pattern like a lawn sprinkler. These streams move radially out from the Sun. Solar rotation makes the magnetic field of spiral form. At Earth's orbit angle between the field-lines and the radial is about 45° . There are also transient streams related to flares/CME's which may be faster.

3.23 The interplanetary magnetic field (IMF)

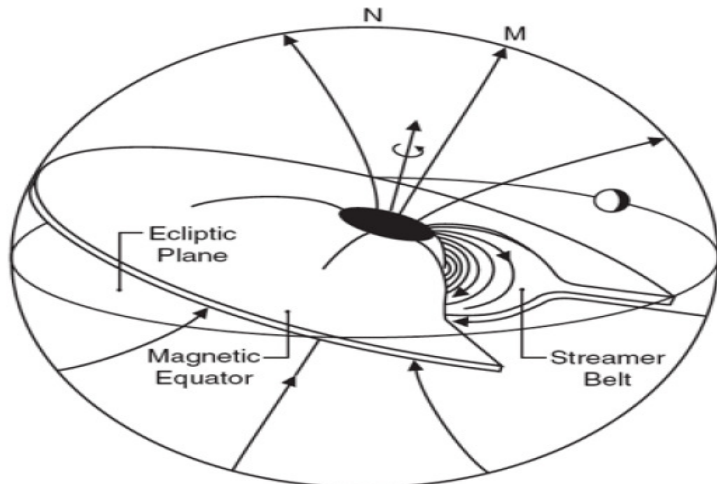


adapted from Pizzo, 1985

Solar magnetic field affects spherical symmetry of the solar wind expansion into spiral shape. Parker's spiral:

$$r - r_0 = - \left(\frac{v}{\Omega} \right) (\theta - \theta_0) \quad (3.10)$$

IMF sweeps the Earth as the Sun rotates, in sectors (typically four) with alternating inward and outward directed magnetic fields. Non-zero angle between Earth's orbit & solar equator, Earth experiences outward/inward magnetic field every 6 months.



3.24 Solar wind characteristics

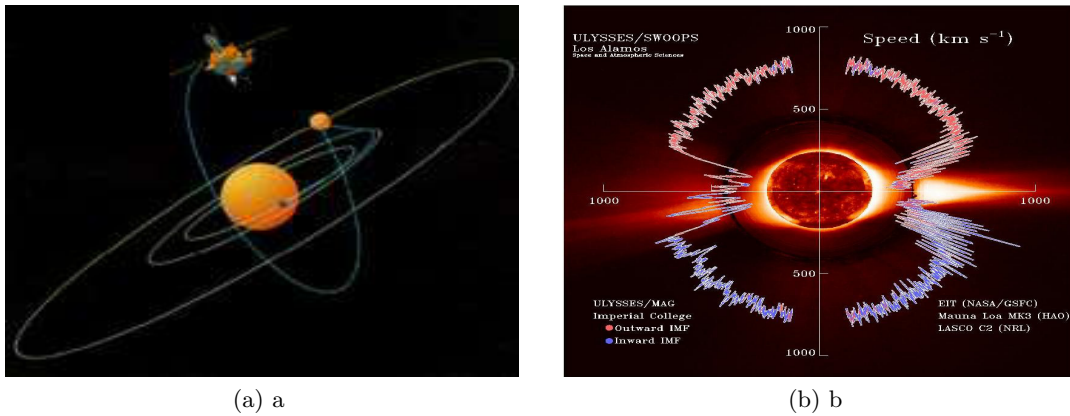
Parameter	Minimum	Average	Maximum
Flux($cm^2 s^{-1}$)	1	3	100
Velocity(km/s)	200	400	900
Density (cm^{-3})	0.4	6.5	100
Helium	0	5	25
B(nT)	0.2	6	80

- These are functions of solar latitude: for example, density is at maximum, speed at minimum around the equator, however, the hemispheres are not exactly symmetric.
- Periodicities in the solar wind can be divided into the time scales of the solar processes, i.e., rotation of the Sun, the orientation of Earth with respect to the Sun.

The first include the 11- and 22-year solar cycles and the 1.3 year and 154 day cycles. Others related to transients leading to geomagnetic activity.

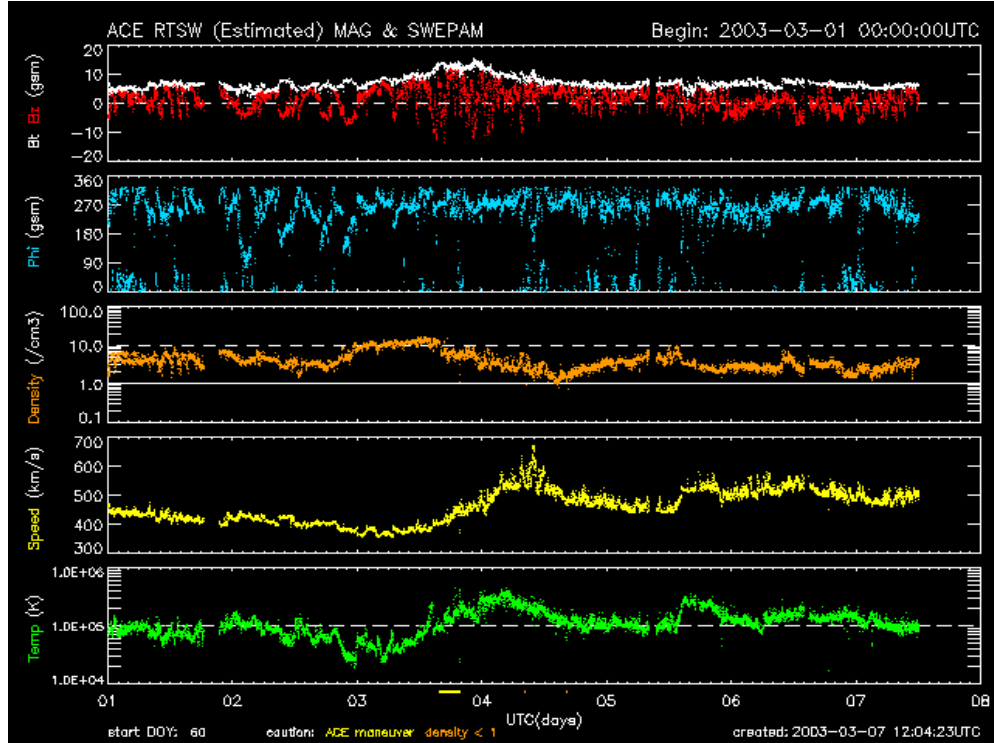
3.25 Spacecrafts for solar wind studies

The Advanced Composition Explorer (ACE) satellite launched in August 1997 placed in L1 point between the Earth and the Sun, where the gravitational attraction of the Sun and Earth are equal and opposite.



- a: Ulysses spacecraft has unique orbit, passing over the Sun's south and north poles. It measured solar wind speed, magnetic field strength and direction, and composition
- b: DIAL PLOT: Solar wind is very irregular, faster near the polar regions than at equatorial latitudes.

3.26 Solar wind condition over a period of 7-days



3.27 Space Weather

- Solar wind or expanding corona propagates outward and fills the interplanetary space.
- Disturbances in the solar wind occur due to coronal holes (fast streams), and solar energetic transient events which shake the Earth's magnetic field and pump energy into the radiation belts.
- Regions on the surface of the Sun often erupt and give off UV and x-rays that heat up the Earth's upper atmosphere.
- This "Space Weather" can change the orbits of satellites and shorten mission lifetimes. The excess radiation can physically damage satellites and pose a threat to astronauts.
- Shaking the Earth's magnetic field can also cause current surges in power lines that destroy equipment and knock out power over large areas. As we become more dependent upon satellites in space we will increasingly feel the effects of space weather and need to predict it.

3.28 Some notable solar space missions

- Yohkoh – (originally Solar A) launched in 1991 and observed till 2001. Two instruments Soft X-ray Telescope (SXT), and Hard X-ray Telescope (HXT) in higher energy X-rays (15-92 keV), particularly for flares.

- Wind spacecraft – For study of the interplanetary medium.
- GOES satellites – In geostationary orbits measured Solar soft X-ray flux since mid-1970s
- RHESSI (Reuven Ramaty High Energy Solar Spectral Imager) – For solar flares from soft X rays ($\sim 3 \text{ keV}$) to $\gamma - rays$ (up to $\sim 20 \text{ MeV}$) and spectroscopy.
- SOHO (Solar and Heliospheric Observatory) – In operation since December 1995 having 12 instruments: Extreme ultraviolet Imaging Telescope (EIT), Large Angle and Spectrometric Coronagraph (LASCO) and the Michelson Doppler Imager (MDI). SOHO is in a halo orbit around the earth-sun L1 point.
- Hinode (originally Solar B) – launched by Japan in September 2006 to observe solar flares.
- TRACE (Transition Region and Coronal Explorer) – To image the TR and solar corona at high angular/temporal resolution.
- SDO (Solar Dynamics Observatory) – Launched in February 2010 in geosynchronous orbit. Composed of 3 instruments: Helioseismic and Magnetic Imager (HMI), Atmospheric Imaging Assembly (AIA) and Extreme Ultraviolet Variability Experiment (EVE).

4 The solar interior: theory and probes

4.1 Understanding solar interior, solar standard models

- We know about the general (global) properties of Sun. But how do we know about the internal structure?
- In absence of direct observations, recourse is taken to construct standard solar model (SSM) . . . a mathematical treatment of the Sun .
- It assumes Sun as a spherically symmetric ball of gas, i.e., all physical parameters are function only of r (distance from the Sun's center)

Internal rotation is assumed to be sufficiently slow (hence neglected) and internal magnetic fields are negligibly weak (of course, these assumptions are not correct).

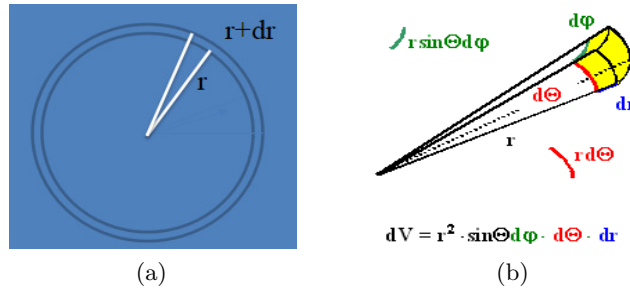
4.2 Standard solar model: formalism

- Theoretical ingredients: Equations of Conservation laws.
 - Mass conservation
 - Momentum conservation
 - Energy conservation
- Additional Equations
 - Energy transport
 - Equation of state
 - Nuclear reaction networks and reaction rates → energy production
 - Opacity, And several assumptions
- There are two basic forces at play:
 - GRAVITY, that causes stars to collapse
 - PRESSURE, that causes stars to expand
 - (Rotation is neglected as an approximation)

4.3 Conservation of mass

In absence of flows, mass of a spherical shell must be accounted by its density. At any point r inside Sun's sphere, the volume element of the shell is:

$$dV = r^2 dr \int_0^\pi \sin \theta d\theta \int_0^{2\pi} d\phi = 4\pi r^2 dr \quad (4.1)$$



then mass in dV is:

$$dm = 4\pi r^2 \rho dr \quad (4.2)$$

Radius of a star can change during its life, while its mass does not change much. Therefore it is customary to use mass m , and not r , as independent variable. Thus we write:

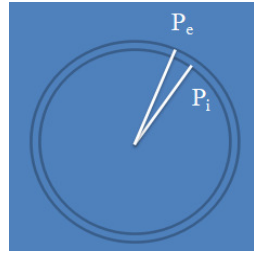
$$\frac{dr}{dm} = \frac{1}{4\pi r^2 \rho} \quad (4.3)$$

giving:

$$\frac{R_\theta}{M_\theta} \approx \frac{1}{R_\theta^2 \bar{\rho}} \text{ or } \bar{\rho} \approx \frac{M_\theta}{R_\theta^3} \quad (4.4)$$

Here, total derivative is used as we have assumed steady state, but in general $r = r(m, t)$ so one must retain partial derivative. We may place boundary condition at $m = m_\theta$. But model must give radius r .

4.4 Conservation of momentum



Pressure (force per unit area) acts outwards. The difference in pressure

$$P_i - P_e = - \left(\frac{dp}{dr} \right) dr = f_p \quad (4.5)$$

Force due to gravity acts inward (acceleration x mass) = $-g(4\pi^2\rho dr)$. Force per unit area due to gravity = $-g(4\pi^2\rho dr)/(4\pi r^2) = -g\rho dr = f_g$. At equilibrium, these forces must balance, so

$$f_p + f_g = 0 \quad (4.6)$$

thus

$$\begin{aligned}\frac{dp}{dr} &= -g\rho \\ \frac{dP}{dr} &= -g\rho = -\frac{Gm}{r^2}\rho\end{aligned}\tag{4.7}$$

Converting dr to dm (using conservation of mass $dm = 4\pi r^2 \rho dr$):

$$\frac{dP}{dm} = -\frac{Gm}{4\pi r^4}\tag{4.8}$$

Temperature and pressure of solar core can be estimated from this. L.H.S $\Rightarrow -\int_0^M \frac{dP}{dm} = P_{core} - P_{surface}$, and R.H.S $\Rightarrow \int_0^M \frac{Gm}{4\pi r^4} dm = \frac{GM^2}{8\pi R^4}$. Thus

$$P_{core} = P_{surface} + \frac{GM^2}{8\pi R^4} \Rightarrow P_{core} \approx \frac{GM^2}{8\pi R^4} \quad \text{assuming } P_{core} \gg P_{surface}\tag{4.9}$$

Using ideal gas law:

$$P_{core} = nkT = \frac{\rho kT}{m_p}\tag{4.10}$$

where k (Boltzman cont.), n (no. density $atoms/cm^3$). This gives

$$T_{core} \sim \frac{GMm_p}{kR}\tag{4.11}$$

This gives $T_{core} \sim 2.7 \times 10^7 K$ (Actual value $1.5 \times 10^7 K$)

4.5 Some results of imbalance of forces

When the forces do not balance, the shell accelerates. We have from equation of momentum conservation:

$$\begin{aligned}\frac{dm}{4\pi r^2} \cdot \frac{d^2r}{dt^2} &= f_p + f_g = -\frac{dP}{dr} - g\rho dr = -\frac{dP}{dm}dm - \frac{Gm}{r^2}\rho dm \frac{1}{4\pi r^2\rho} \\ &\Rightarrow \frac{d^2r}{dt^2} = -4\pi r^2 \frac{dP}{dm} - \frac{Gm}{r^2}\end{aligned}\tag{4.12}$$

1. For hydrostatic equilibrium, $\frac{d^2r}{dt^2} = 0 \Rightarrow \frac{dr}{dt} = 0$ or const

2. When P vanishes \rightarrow Free Fall. Assuming τ_{ff} = time to collapse,

$$\frac{d^2r}{dt^2} \approx \frac{R}{\tau_{ff}^2} = g \Rightarrow \tau_{ff} \approx \left(\frac{R}{g}\right)^{1/2} \sim 27 \text{ min (for sun)}\tag{4.13}$$

3. When g vanishes \rightarrow star explode. Assuming τ_{exp} = time to explode,

$$\frac{d^2r}{dt^2} = 4\pi r^2 \frac{dP}{dm} = -\frac{1}{\rho} \frac{dP}{dr} \Rightarrow \frac{R}{\tau_{exp}^2} = \frac{P}{\rho R} \Rightarrow \tau_{exp} \approx R \left(\frac{\rho}{P}\right)^{1/2} \simeq \frac{R}{c_s}\tag{4.14}$$

where c_s is sound travel time \Rightarrow again 27 min for Sun.

4.6 The interplay between pressure and gravity plays out throughout a star's life

- There are stages in a star's life where gravity wins and the star begins to collapse (From molecular cloud \Rightarrow proto Sun \Rightarrow present epoch).
- There are stages where pressure wins and the star begins to expand =; End phase \Rightarrow Red giant \Rightarrow planetary nebula
- For the most part though (in main sequence phase), gravity and pressure balance each other \Rightarrow hydrostatic equilibrium. \Rightarrow main sequence stage HR diagram
- The Sun is currently in this state of life.

4.7 Conservation of energy

Define dl =luminosity of a mass shell, i.e.

$$\int_0^m \frac{dl}{dm} dm = L \quad (4.15)$$

An eqn of continuity must be satisfied by radiation where dE/dt is the rate of energy production per unit thickness of a shell of radius r , L the total net energy flux through the shell.

$$\begin{aligned} \frac{dE}{dt} + \frac{dL}{dr} &= 0 \Rightarrow \frac{dL}{dr} = -\frac{dE}{dt} \\ \frac{dL}{dr} &= 4\pi r^2 \rho \varepsilon \end{aligned} \quad (4.16)$$

or

$$\frac{dL}{dm} = \varepsilon \quad (4.17)$$

Here ε is the nuclear energy released per unit mass by thermonuclear reactions in the gravitationally stabilized solar fusion reactor. It is assumed that energy produced by nuclear reactions equals the photon luminosity of the Sun.

The mean energy generation rate for the Sun can be inferred from the above:

$$\bar{\varepsilon} \approx \frac{L_\theta}{M_\theta} \quad (4.18)$$

4.8 Procedure for calculating a solar model

A star is considered to be at zero age (protostar) where it has a homogeneous composition. It has begun to derive most of its luminosity from nuclear reactions . Thus the period of contraction from a cloud of gas and dust is neglected.

The Standard Solar Model (SSM) considers evolving a one solar mass(M_θ) stellar model at zero age to the present age of the Sun.

The abundance of elements in the zero age solar model is estimated from primordial meteorites. Along with this abundance information, a reasonable guess at the zero-age luminosity, is then converted by an iterative procedure into the correct value for the model.

The set of basic differential equations are integrated numerically. The star is made up of spherically symmetric shells, with conditions slowly changing from shell to shell. The laws of physics relate one shell to the others, that allow each physical quantity to be numerically determined in each layer.

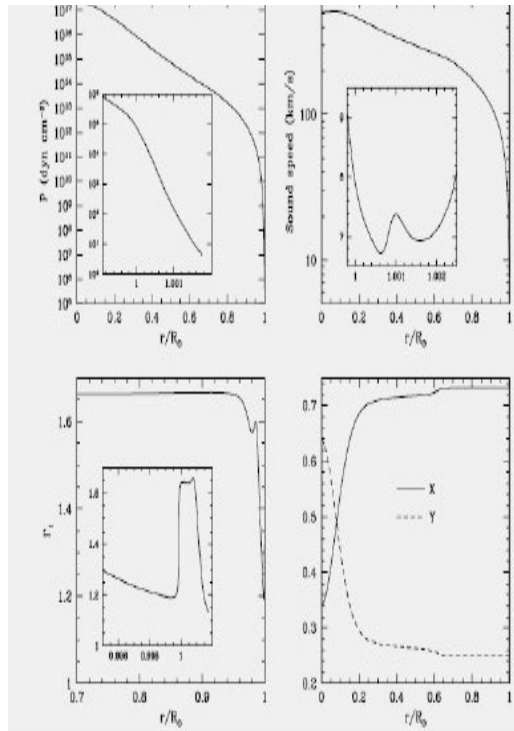
Numerical integration is carried out in finite steps making use of the equations of state, giving relationships for the pressure, the opacity and the energy generation rate in terms of the density, temperature and composition.

In principle, an integration might be carried outward from the center, where natural boundary conditions on mass and luminosity are $M_\theta = 0$, and $L_\theta = 0$ at $r = 0$. The central pressure and temperature, P_c , and T_c , are actually unknown, but estimated values are obtained from hydrodynamical eqns.)

The surface boundary conditions for the stellar structure equations are taken as $L = L_\theta$, $P = 0$, $R = R_\theta$ and $T = 0$.

Any discrepancy from the measured values of the Sun's luminosity, surface abundances, etc. can then be used to refine the model.

Calculating a solar model means the determination of pressure, temperature and chemical composition as a function of mass or radius through the Sun.



There are several models. One of the recent Standard Solar Model is by Brun, Turck-Chieze & Zahn (1999)

Temperature, density, pressure, and sound speed decrease as r is increased, except some departures near the surface (inset)

Also shown are adiabatic index Γ_1 and H/He abundance profiles.

4.9 Do we have any checks on the SSM?

The standard solar model can be tested by the measurement/detection of neutrinos produced inside the Sun, and solar oscillations (Helioseismology)

Solar energy output derived from nuclear reactions by pp-chain (2ν pp reaction), predict production of 2×10^{38} neutrinos per second.

At the distance of earth (1AU), no. of ν crossing $1\text{ sq m/sec} = 6 \times 10^{14}$

Solar oscillations: precise measurement provide nearly 'direct' knowledge of solar internal structure and dynamics.. sound speed, density, rotation..

These serve as complementing probes and enable us "to see" inside the Sun, and deduce thermal and chemical composition profiles as well as rotation and magnetic fields prevailing in the solar interior.

4.10 Solar neutrinos

Historically, the measurement of neutrino flux produced in the reactions operating in the solar core was the first and only probe the physical conditions in the deep interior.

The neutrino fluxes are sensitive to the temperature and composition profiles in the central regions of the Sun.

It was, therefore, hoped that temperature dependence of the nuclear reaction rates in the production of neutrinos would help in determination of the Sun's central temperature. And hence, could help check for SSM.

4.11 How do we detect them?

Neutrinos are very weakly interacting, require large detectors in volume, and are often built deep underground in order to reduce effects of cosmic rays and other background radiation.

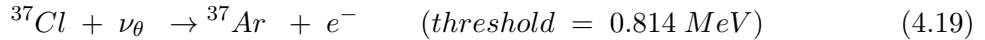
Several neutrino observatories based on various techniques were built in Japan, Europe, and Canada. For example, The Sudbury Neutrino Observatory (SNO) located deep underground in a Mine in Ontario, Canada. The detector was designed to detect solar neutrinos through their interactions with a large tank of heavy water.

But early efforts faced problem: Standard solar models predicted 3 times more neutrino flux than observed \Rightarrow neutrino deficiency \Rightarrow standard solar models were in trouble!?

4.12 The Homestake experiment

Radiochemical experiments – chlorine and Gallium (charge current or CC reactions).

- Chlorine experiment by Davis(1964) was sensitive to intermediate and high energy neutrinos. It has a tank containing 615 tons of ordinary cleaning fluid, tetrachloroethene, C_2Cl_4 . Located 1480m underground in the Homestake gold mine in South Dakota. Chlorine nuclei are the solar neutrino absorbers, chlorine is converted to argon according to the reaction



The capture rate is dominated by the 8B neutrinos contributing 5.9 SNU, with the 7Be neutrinos making a contributing of 1.1 SNU ($1\text{SNU} = 10^{-36}$ captures per target atom per second).

- Unfortunately, it reported solar neutrino counting rate of 2.56 ± 0.23 , and NOT $7.6 \pm 1.2\text{SNU}$ as predicted by the standard solar model for the Chlorine experiment.
- This puzzling deficit in the neutrino counting rate, by nearly a factor of 3 over the SSM prediction, constitutes the solar neutrino problem (e.g., Cleveland et al. 1998).

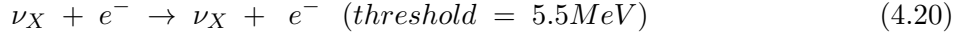
4.13 Homestake neutrino detector

Located 1480 meters underground in a gold mine, South Dakota. 100,000 gallon tank of perchloroethylene (a common dry-cleaning fluid). The reaction threshold is 0.814 MeV to be captured by the chlorine-37 nucleus.



4.14 The Japanese Kamikande and SuperKamiokane neutrino expts

A 680 ton water tank located 1 km underground in Kamioka mine (Fukuda et al. 1996). Water detectors detect neutrinos through Cerenkov light from elastic $\nu - e^-$ scattering (ES reaction) if the recoil energy of the electron is at least 5 MeV.:

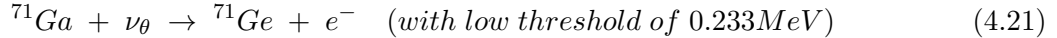


The upgraded SuperKamiokande experiment (Fukuda et al. 1999) are sensitive only to the high-energy 8B neutrinos released by the pp-chain, high-temperature dependent reaction rate. It is possible to determine their arrival direction and can identify neutrinos coming from the solar direction.

The measured flux from the SuperKamiokandde experiment is again deficient by about 50% over the total flux predicted by the standard solar model.

4.15 Other experiments...

There are three other radiochemical experiments, GALLEX, SAGE and SNO (Hampel et al. 1999) that use a gallium detector



These are capable of detecting the low-energy pp-neutrinos while the chlorine expt detected intermediate and ES expts the high energy neutrinos.

They reported measurement of the solar neutrino counting rate of 74.7 ± 5.0 SNU, while the SSM prediction of the neutrino capture rate for the gallium experiments is 128 ± 8 SNU.

Again a deficit in the measured neutrino counting rate.

Thus the experimental efforts and more refined theoretical models have only confirmed the discrepancy between the measured and calculated neutrino fluxes.

4.16 Predictions for solar neutrino detection

Typical predictions for observable fluxes for the gallium, chlorine and water detectors, and observational results are as follows: Where $R = (\text{measured neutrino flux}) / (\text{predicted model neutrino flux})$.

Expt	Chlorine	Gallium	SK	SNO
Threshold (MeV)	0.834	0.233	5	5
Predicted Flux (SNU)	7.7 ± 1.1	130 ± 7	1.0 ± 0.15	
R	0.33 ± 0.03	0.55 ± 0.03	0.465 ± 0.015	0.36 ± 0.015

Solar neutrino unit (snu): Capture of one neutrino per second per 10^{36} target atoms.

Neutrino deficit??

- Was it an observational problem? This was a popular explanation as long as the Homestake observation alone existed. But ruled out after gallium and water detector results.
- Was the problem with erroneous solar models? (5–10% lower temperature in core gives neutrino flux consistent with Homestake detector).
- Neutrino physics is incomplete (i.e. the standard model of particle physics wrong!)
- Nuclear physics describing the pp-chain is incorrect?
- Nuclear physics describing interaction between neutrino and ^{37}Cl is incorrect (Kamiokande & ^{71}Ga showed that this wasn't the problem)

4.17 Accounting for the observed deficit: non-standard Models

- Reduction in the central temperature: It will lead to even larger suppression of the high energy 8B neutrino flux to which the SuperKamiokande experiment is exclusively sensitive. Paradoxically, the Homestake experiment that detects the intermediate as well as high energy neutrinos will then show an even larger reduction in the neutrino counting rate. Thus by reducing the core temperature it is not possible to get a solar model which simultaneously matches both the Homestake and SuperKamiokande measurements.
- Reduce the relative abundance of heavy elements (low Z): This would reduce opacity κ and thus the temperature gradient. However, this does not seem a plausible way for solar-type stars in the first place, and the solar oscillation observations contradict this suggestion as well.
- A rapidly rotating core which would lower the thermal pressure: This is inconsistent with oscillation results that indicate that the core rotates at nearly the same angular speed as the surface.
- A strong internal magnetic field: It could lower the central temperature but it should be very intense to have a significance, say 10%, contribution to the pressure of the core.

All such proposals lead to a slight reduction in the central temperature causing a lowering of the flux of high-energy neutrinos.

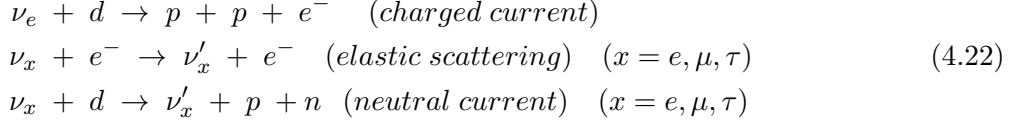
4.18 The Sudbury neutrino observatory

In 2001 the Sudbury Neutrino Observatory (SNO) first results indicated that the solar neutrino problem was coming to its final solution. This D_2O detector was able to distinguish between the total neutrino flux and the ν_e flux. (see results published in Sep. 2003 <http://www.sno.phy.queensu.ca/>).

SNO experiment at a depth of over 6000 meters uses 1000 tons of heavy water containing the deuterium isotopes of hydrogen for detecting solar neutrinos by Cerenkov radiation that is emitted when an in-coming neutrino creates a free electron or neutron (sensitive to both charge, or CC,

and neutral current or NC reaction). The deuterium present in the heavy water is dissociated by a neutrino. All three flavors of neutrino ν_X (ν_e, ν_μ, ν_τ) participate equally in this process.

The Sudbury Neutrino Observatory is capable of measuring the 8B neutrinos ($> 5\text{MeV}$) through the flowing reactions:



It was reported that neutrinos aren't missing, e^- neutrinos produces in the Sun just convert into μ and τ neutrinos (Ahmad et al. 2001). The neutrino problem actually lies with the neutrino physics.

4.19 Years of extremely difficult neutrino problem got resolved, thanks to solar standard models, with the series of neutrino observing efforts

Superkamiokande observations in 1998 indicated neutrinos oscillated between 3 flavors: electron neutrinos (ν_e), muon neutrinos (ν_{mu}), and tau neutrinos (ν_{tau}). Also, they have finite masses.

In 2001 Sudbury Neutrino Observatory (SNO) was able to distinguish between the total neutrino flux and the ν_e flux.

The Sun produces electron neutrinos (ν_e) only. The predicted fluxes are for electron neutrinos.

So, possibility of a large enough fraction of solar neutrinos transforming to other neutrino flavors before reaching the Earth → elegant solution to the whole problem.

Standard solar model was vindicated together with new neutrino observations and resolved "the solar neutrino problem" and test SSM.

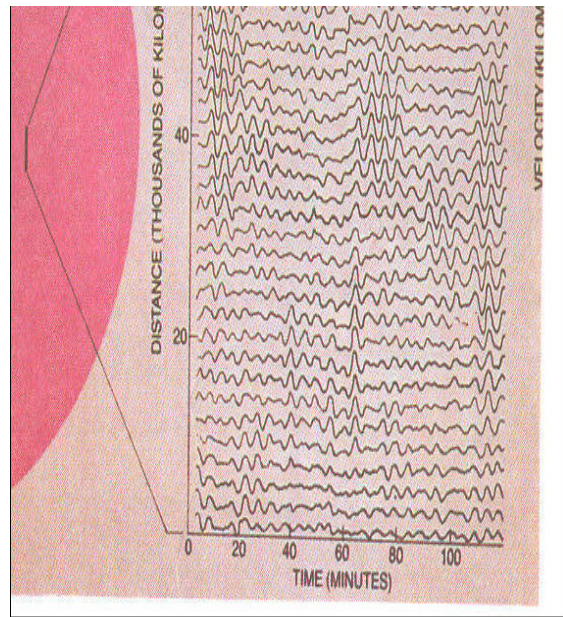
4.20 Discovery of solar oscillations – another tool to probe solar interior

Oscillatory motions on the Sun were first reported in Doppler imaging observations of the solar photosphere by Leighton, Noyes & Simon in 1960.

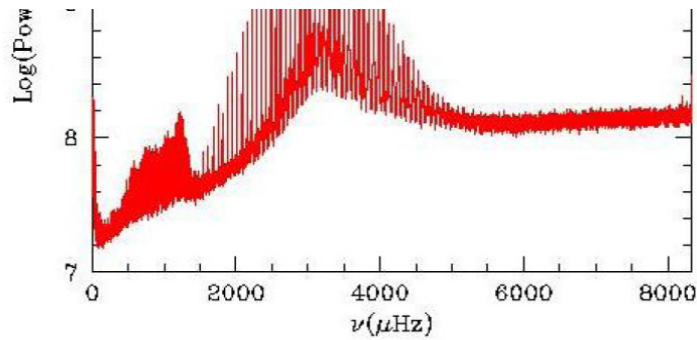
The oscillations with a period of ~ 5 min (Freq. ~ 3 mHz). are best seen as Doppler shifts of spectral lines, but also as intensity variations.

The amplitude is a few 10s of meters/second, increases only slightly with height in the atmosphere.

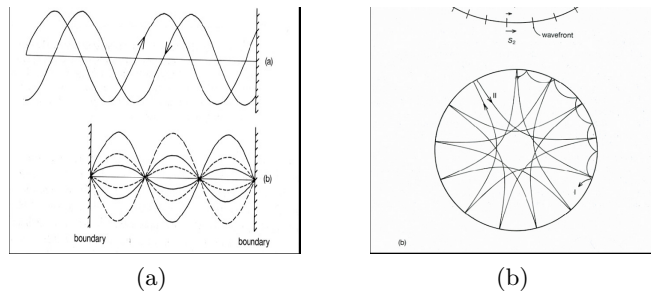
These surface variations result from superposition of millions of modes of oscillations.



4.21 Individual modes can be inferred from power series analysis of long time series of doppler images of the solar photosphere.



4.22 What causes these waves?



Ulrich (1970) and, independently, Leibacher & Stein (1971) proposed that observed oscillations are due to standing acoustic waves trapped in cavities that extend well into the Sun's interior.

A standing wave arises from two waves travelling in opposite directions, reflected from boundaries, forming an acoustic cavity in which waves travel repeatedly. At the two boundaries, nodes (with zero displacement) are established.

Acoustic cavities can exist without solid boundaries, e.g., in the solar interior.

Convection excites stationary sound waves, which are reflected from two boundaries and establish a variety of modes. Each solar mode is trapped in cavities of varying depths, depending on horizontal wavelength - affected by internal temperature, composition, flows.

4.23 How are the modes reflected/refracted in the interior?

Temperature increasing steeply towards the centre, so does the sound speed: $\nu_s \propto T^{1/2}$.

Thus for a sound wave, which propagates towards the interior from the surface at an angle, the wave-front's (perpendicular to the direction of the wave) deeper edge travels faster than its upper edge

\Rightarrow wave turns gradually and travel in an arc.

While travelling upwards, the wave undergoes total internal refraction at the Sun's surface due to abrupt decrease of density (due to sharp ρ gradient).

Large l modes confined to outer layers, small l modes penetrate deeper cavities. These modes provide a diagnostic tool to probe the interior of the Sun.

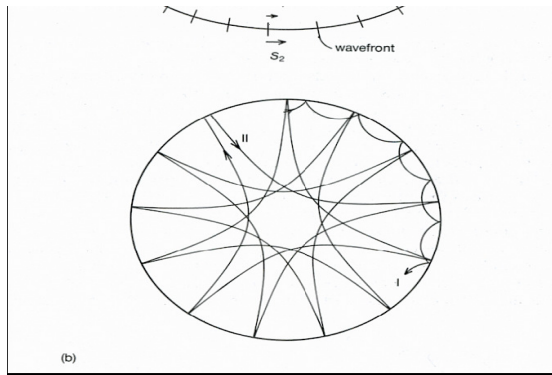


Figure 30: Shallower the angle, shallower its penetration depth – higher angle (\rightarrow longer λ), deeper penetration depth

4.24 Solar global oscillations: mode description

An observational parameter in spherical body, such as, velocity or intensity is a superimposition of many modes of solar oscillation:

$$\nu(\lambda, \theta, \varphi, t) = \sum_{n,l,m} \nu_n(r) Y_l^m(\theta, \varphi) e^{i\omega t} \quad (4.23)$$

where latitude θ , longitude φ and depth r . The spatial dependence in the spherical harmonic

$$Y_l^m = P_l^{|m|}(\theta) e^{im\varphi} \quad (4.24)$$

The time part is written as $e^{i\omega t}$ and the radial part as $\nu_{nl}(r)$ which gives the radial structure of the modes with given degree l and radial order n .

Thus, a mode with frequency $\nu = \frac{\omega}{2\pi} = \frac{1}{P}$ is characterized by three integers:

degree $l \geq 0$ (total no. of planes slicing the solar surface), azimuthal order m (number of planes cutting the equator perpendicularly, $|m| < l$)

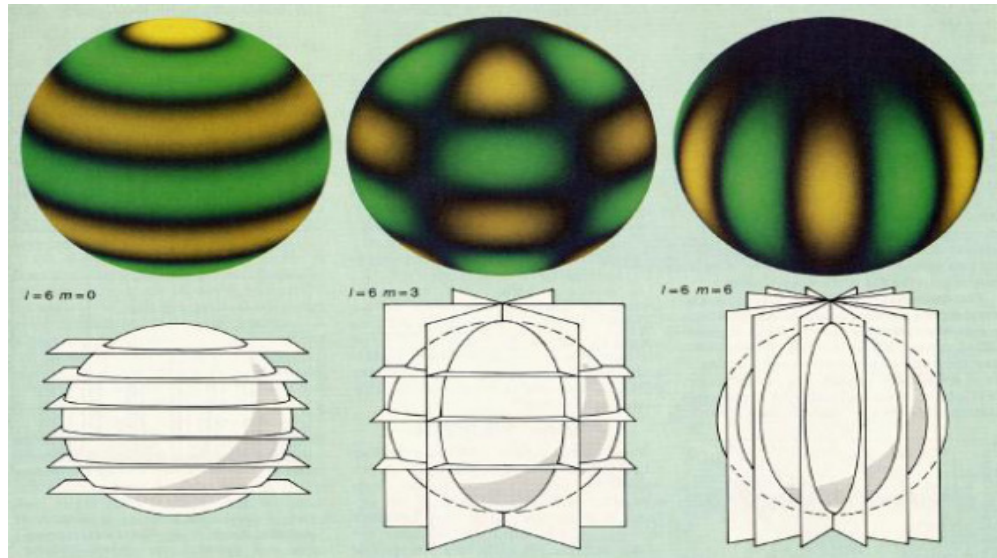
\Rightarrow For each l , there are $(2l + 1)$ degenerate m modes (due to neglect of rotation), radial order n $-\infty < n < \infty$ gives number of nodes in the interior.

4.25 Surface structure of solar oscillation modes as described by spherical harmonics

The degree l measures the horizontal component of the wavenumber

$$k_h = \frac{[l(l+1)]^{1/2}}{r} \quad (4.25)$$

\Rightarrow large l means small horizontal wavelength λ_h . (Surface structures of modes with $l = 6$ and $m = 0, 3$, and 6 are shown below):



4.26 Radial order n defines number of nodes inside the interior

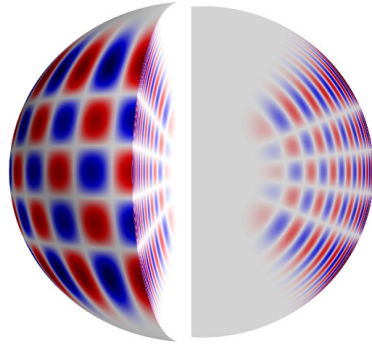


Figure 31: A solar p -mode with $n = \frac{1}{4}$, $l = 20$ and $m = 16$

The surface shows the corresponding spherical harmonic.

4.27 Helioseismology

Helioseismology is the study of the wave oscillations in the Sun. Changes in the propagation of these waves through the Sun reveal inner structures and allow to infer profiles of the interior conditions of the Sun.

In analogy with terrestrial seismology, the solar seismology is termed as Helioseismology.

It is possible to infer the location of the base of convection zone in the outer envelope of the Sun.

Information about the core of the Sun using helioseismology provides a method, along with the SSM, to calculate the age of the Sun. This is independently of the method of inferring Sun's age from meteorites.

Helioseismology has helped in refining and constraining SSMs, and to the resolution of neutrino problem.

5 Helioseismology: technique and results

5.1 Helioseismology

Helioseismology is the study of the wave oscillations in the Sun. Changes in the propagation of these waves through the Sun reveal inner structures and allow to infer profiles of the interior conditions of the Sun.

In analogy with terrestrial seismology, the solar seismology is termed as Helioseismology.

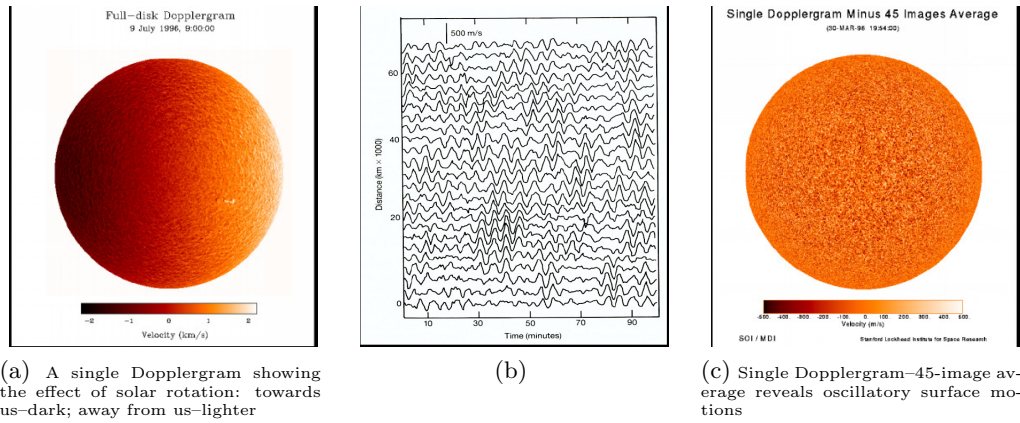
Oscillatory motions, with a period of 5-min ($\nu \sim 3.3\text{mHz}$) and amplitude of \sim few 10sm/s , on the Sun were first reported in Doppler imaging observations of solar photosphere by Leighton, Noyes & Simon in 1960.

10^7 modes are present on solar surface at any time, with typical amplitude of a mode $\pm 20\text{ cm/s}$, and total amplitude of all modes \sim a few 100m/s

Helioseismology has helped in refining and constraining SSMs, and to the resolution of neutrino problem.

5.2 Discovery of oscillations

Solar Dopplergram: small displacements in suitable velocity sensitive spectral line wavelength alternating between towards (blue shift) and away (red shift) from the observer are measured. The oscillations are best observable in the central part of the Sun \Rightarrow radial oscillations



5.3 Solar oscillations – a comparison

Velocity fields (LOS) at Solar Surface

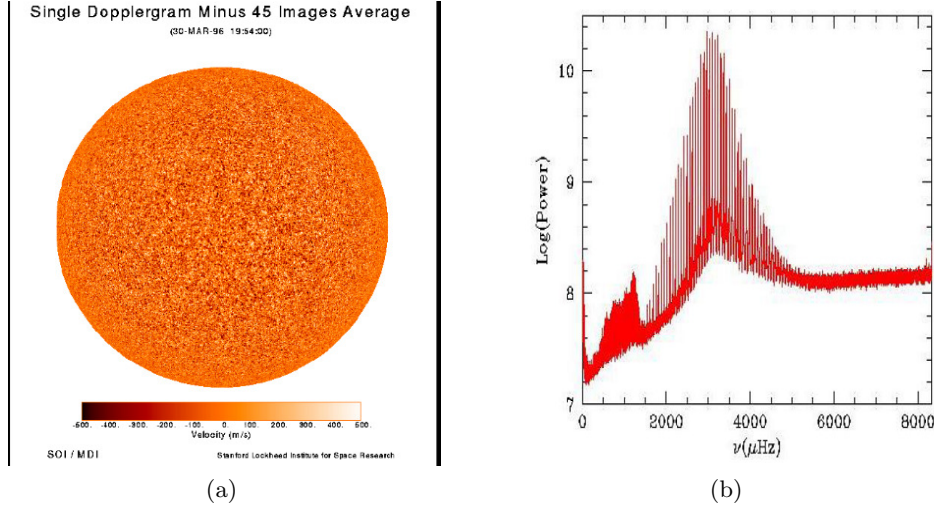
Earth's rotation & Orbital vel.	Solar Rotation	Convective motion	Solar Oscillations
500 m/s	2km/s	1km/s	<1 m/s

Intensity variation at solar surface

Convection (granulation)	Sunspots	Solar oscillations
15%	factor of 10	10^{-5}

The Sun's photosphere vibrates with a period of around 5 minutes. These oscillations are best seen as Doppler shifts of spectral lines.

These surface variations result from superposition of over 10 million modes of oscillations. Individual modes can be inferred from Fourier analysis of long time series of Doppler images of the solar photosphere.



5.4 Solar global oscillations: mode description

An observed parameter, such as, velocity or intensity, is a superimposition of many modes of solar oscillation (in spherical coordinates):

$$\nu(r, \varphi, \theta, t) = \sum_{n,l,m} \nu_n(r) Y_l^m(\theta, \varphi) e^{i\omega t} \quad (5.1)$$

where, latitude θ longitude φ , and depth r . The spherical harmonics $Y_l^m = P_l^{|m|}(\theta) e^{im\varphi}$ gives surface structure, temporal part by $e^{i\omega t}$, and the radial part $\nu_{nl}(r)$ with a mode characterized with frequency $\nu = \frac{\omega}{2\pi} = \frac{1}{P}$ and 3 integers, degree l and radial order n .

Degree $l \geq 0$ (total no. of planes slicing the solar surface),

Azimuthal order m (number of planes cutting the equator perpendicularly $|m| \leq l \Rightarrow$ For each l , there are $(2l + 1)$ degenerate m modes (due to neglect of rotation)

Radial order n ($-\infty < n < \infty$) gives number of nodes in the interior.

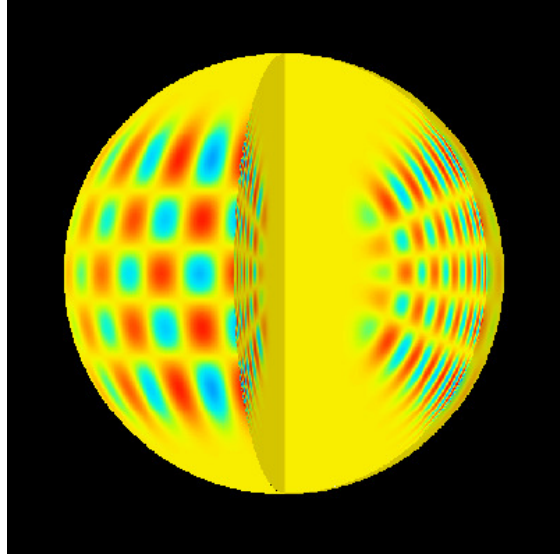


Figure 32: $l = 20, m = 16, n = 14$ and $\nu = 2.93588 \text{ mHz}$

5.5 Basic equations of hydrodynamics

The stability and modes of oscillations of a gravitating gaseous (non-viscous) body are described by the following hydrodynamical equations:

1. Mass conservation (continuity) Equation:

$$\frac{\partial \rho}{\partial t} + \nabla \cdot (\rho \vec{v}) = 0 \quad (5.2)$$

2. Equation of Motion, or Momentum conservation:

$$\rho \left(\frac{\partial \vec{v}}{\partial t} + \vec{v} \cdot \nabla \vec{v} \right) = -\nabla p + \rho \vec{g} \quad (5.3)$$

where $\vec{g} = -\nabla \Phi$ and $\nabla^2 \Phi = 4\pi G\rho$

3. Energy conservation equation:

$$\rho \frac{dQ}{dt} = \rho \varepsilon - \nabla \cdot \vec{F} \quad (5.4)$$

For small amplitude perturbations, the equations are linearized and dispersion relations are obtained describing the waves and oscillations of in a given SSM.

5.6 The linearized equations

$$\begin{aligned}
\text{Equation of continuity :} \quad & \rho_1 + \nabla \cdot (\rho_0 \vec{\xi}) = 0 \\
\text{Equation of momentum :} \quad & \rho_0 \frac{\partial^2 \vec{\xi}}{\partial t^2} + \nabla p_1 - \frac{\rho_1}{\rho_0} \nabla p_0 + \rho_0 \nabla \Phi_1 = 0 \\
\text{Poisson's Equation :} \quad & \nabla^2 \Phi_1 = 4\pi G \rho_1
\end{aligned} \tag{5.5}$$

where $\vec{\xi} = (\xi_r(r), \xi_h(r) \frac{\partial}{\partial \theta}, \frac{\xi_h(r)}{\sin \theta} \frac{\partial}{\partial \phi}) Y_l^m(\theta, \phi) e^{i\omega t}$ is a vectorial distance of a gas parcel from its equilibrium position, and Eulerian perturbations (at a fixed position in the Sun) of various parameters are denoted by subscript '1'. By eliminating the variables ξ_n and ρ_1 , we have

$$\begin{aligned}
\frac{1}{r^2} \frac{d}{dr} (r^2 \xi_r) - \frac{\xi_r h}{c^2} + \frac{1}{\rho_0} \left(\frac{1}{c^2} - \frac{l(l+1)}{r^2 \omega^2} \right) p_1 - \frac{l(l+1)}{r^2 \omega^2} \Phi_1 &= 0 \\
\frac{1}{\rho_0} \left(\frac{d}{dr} + \frac{h}{c^2} \right) p_1 - (\omega^2 - N^2) \xi_r + \frac{d\Phi_1}{dr} &= 0 \\
\frac{1}{r^2} \frac{d}{dr} \left(r^2 \frac{d\Phi_1}{dr} \right) - \frac{l(l+1)}{r^2} \Phi_1 - \frac{4\pi G \rho_0}{h} N^2 \xi_r - \frac{4\pi G}{c^2} p_1 &= 0
\end{aligned} \tag{5.6}$$

where $h = -\frac{1}{\rho_0} \frac{dp_0}{dr}$, $c^2 = \frac{\Gamma_1 p_0}{\rho_0}$, Lamb frequency $S_l^2 = \frac{l(l+1)c^2}{r^2}$ and the Brunt–Väisälä frequency $N^2 = h \left(\frac{1}{\Gamma_1 p_0} \frac{dp_0}{dr} - \frac{1}{\rho_0} \frac{dp_0}{dr} \right)$. These are solved numerically with appropriate boundary conditions, and only non-trivial solution are considered for particular values of eigen-frequencies.

On eliminating p_1 and Φ_1 from the set of eqns. for non-radial oscillations we can describe the properties of oscillation modes, and their frequencies by the following:

$$\frac{d^2 \xi_r}{dr^2} = \frac{\omega^2}{c^2} \left(1 - \frac{N^2}{\omega^2} \right) \left(\frac{S_l}{\omega^2} - 1 \right) \tag{5.7}$$

where the Brunt–Väisälä frequency $N^2 = h \left(\frac{1}{\Gamma_1 p_0} \frac{dp_0}{dr} - \frac{1}{\rho_0} \frac{dp_0}{dr} \right)$, Lamb frequency $S_l^2 = \frac{l(l+1)c^2}{r^2}$.

Evidently, the characteristic frequencies, acoustic or Lamb frequency (S_l) and the buoyancy or Brunt–Väisälä frequency (N) play a very important role in determining the behaviour of these modes. N is the freq with which a small fluid element will oscillate about its equilibrium position when displaced. It is independent of degree l .

But, Lamb frequency is l dependent. For $l = 0$, $S_l = 0$

5.7 Types of solar oscillations

There are two types of eigen-frequencies allowed. Dominant restoring force depends upon location in the Sun and on perturbation frequency.

p-(acoustic) modes–high frequency: where pressure gradient is the main restoring force. They travel with the sound speed C_s , and live longest where C_s is the lowest, i.e., at the solar surface,

since $C_s \sim T^{1/2}$. They propagate throughout the solar interior, but are evanescent outside the photosphere.

g-(gravity) modes–low frequency: where buoyancy due to gravity is the main restoring force. They propagate in the radiative interior and in the atmosphere, but are evanescent in convection zone (their amplitude drops exponentially there, and very small amplitudes are expected at the surface).

g-modes are expected to be most sensitive at the solar core while p-modes are most sensitive at the surface.

Upper limit on solar interior g-modes lies below 1cm/s while p-modes have amplitudes of a few meters/second.

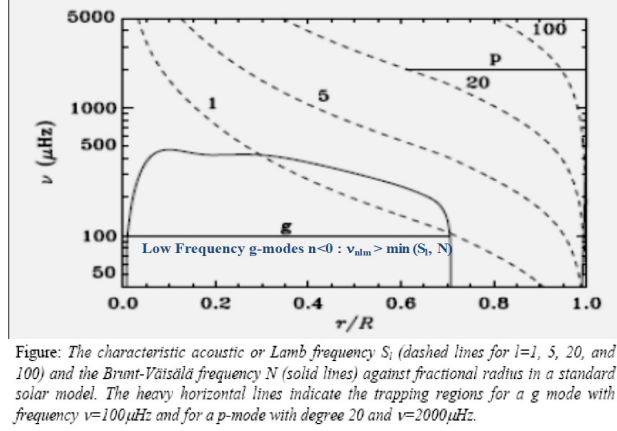
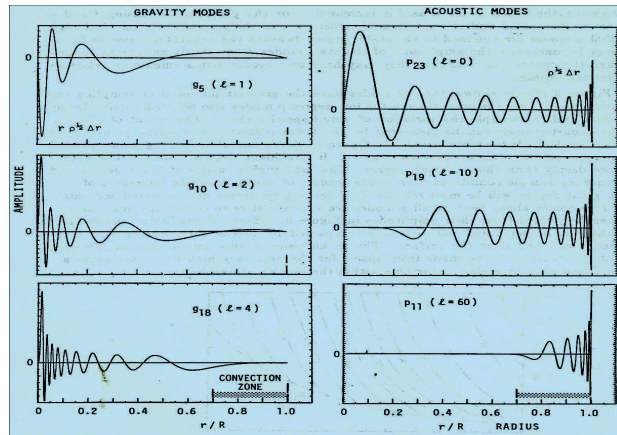


Figure: The characteristic acoustic or Lamb frequency S_l (dashed lines for $l=1, 5, 20$, and 100) and the Brunt–Väisälä frequency N (solid lines) against fractional radius in a standard solar model. The heavy horizontal lines indicate the trapping regions for a g mode with frequency $\nu=100\mu\text{Hz}$ and for a p-mode with degree 20 and $\nu=2000\mu\text{Hz}$.

The characteristic acoustic or Lamb frequency S_l (dashed lines) for $l = 1, 5, 20$, and 1000, and the Brunt–Väisälä frequency N (solid lines) against r/R in a SSM. The horizontal heavy lines indicate the trapping regions for a g-mode with $\nu = 100 \mu\text{Hz}$ and for a p-mode with $l = 20$ and $\nu = 2000 \mu\text{Hz}$.

5.8 Radial displacement corresponding to some p- and g-modes calculated for a standard solar model



5.9 Solar Dispersion Relation : The $l - \nu$ Diagram

Modes resonating between two turning points, r_0 and r_1 , survive destructive interference only when an integral number of vertical wavelengths fit in the cavity defined by the two turning points:

$$\int_{r_0}^{r_1} k_r(r) dr = n\pi + \varepsilon \quad (5.8)$$

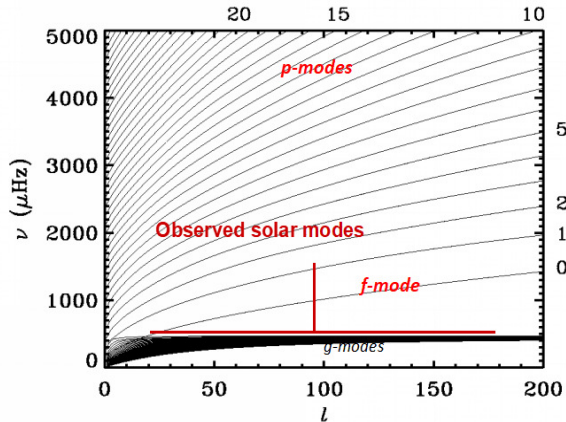
where $k_r(r)$ is the vertical wave number, and ε is a correction factor.

Then radial order n of the modes define the dispersion relation between degree l (through $k_r(r)$) and determines discrete frequency for every given l .

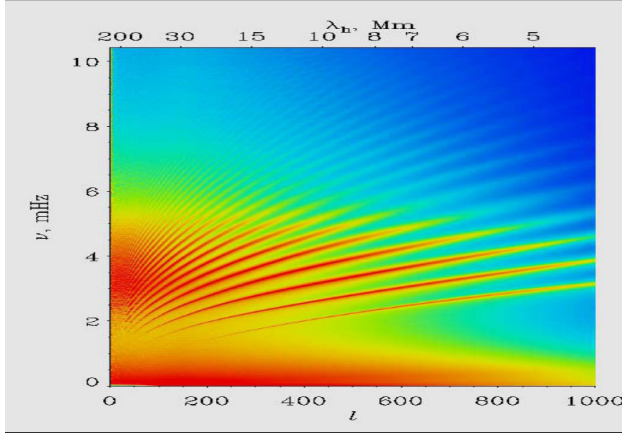
Based on this relation, a $l - \nu$ diagram of frequencies as a function of degree l can be plotted.

The power of solar modes appears to be concentrated in discrete ridges corresponding to every radial order n .

5.10 Solar dispersion relation: the $l - \nu$ diagram, frequencies of a standard model



$$k_h = \frac{[l(l+1)]^{1/2}}{r} \text{ such that } \lambda_h l \sim 2\pi R_\theta.$$



Power spectrum from a 6-day long time series of MDI-SOHO data in 1996. The ridges in the $l - \nu$ diagram correspond to p-modes of different radial order n . For the same l , ridges represent mode with different n ; for a given $l \neq 0$ penetration depth increases with frequency ν (as number of ridges increases too).

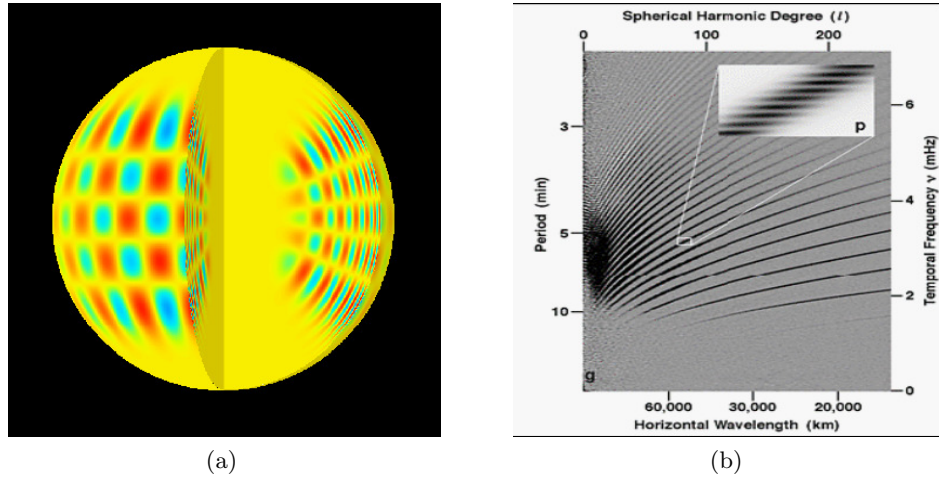
5.11 Modes and solar structures

Only waves with specific combinations of period (P) and horizontal wavelength (λ_h) resonate within the Sun.

The precise combinations resonate in the Sun's interior; and produce "ridges" of larger power.

Most of the p-mode power lies between $2.5 - 4.5\text{mHz}$ (period range: $4.8 - 6.5\text{min}$), $10 < l < 200$, and $k_h < 0.8\text{Mm}^{-1}$ ($\lambda_h > 8 \times 10^3\text{km}$).

g-mode: $\nu \leq 0.3\text{mHz}$; ($T \geq 50\text{min}$)



Each of the solar modes is trapped in a different region of the solar interior. Hence, sensitive to structures and dynamics in the corresponding region.

Combining information from large number of independent modes, it is possible to infer the structure and dynamics of the solar interior.

But ... Require high accuracy for velocity measurements. For example, Doppler shift for $\lambda 6000 \text{ \AA}$ solar spectral line (line width $\sim 0.1 \text{ \AA}^\circ$), corresponding to a velocity amplitude $\Delta\nu \sim 1 \text{ m/s}$

$$\Delta\lambda = \lambda_0 \frac{\Delta\nu}{c} \sim 10^{-5} \text{ \AA}^\circ \quad (5.9)$$

Thus, for individual mode amplitudes $\sim 0.1 \text{ m/s}$ would need measurement accuracy of parts per million of its width.

However, now accuracy of current instruments: better than 1 cm/s .

5.12 Maximum value of observable frequencies and degree l (temporal cadence and spatial resolution)

Maximum value of observable frequencies depends on the time-interval (cadence) Δt between observations.

For Nyquist frequency $= \frac{1}{2\Delta t} = 8.3 \text{ mHz}$ (observed from $l - \nu$ diagram), one gets required temporal cadence $\Delta t = 1 \text{ minute}$.

For $l \geq 250 \Rightarrow$ spatially imaged observations of Sun's full disk at $1k \times 1k$ pixels are required (now a days CCDs with $4k \times 4k$ available).

\Rightarrow better resolution needed for higher degree l .

5.13 Frequency resolution

For time series of one day duration: $T = 24 \text{ hr}$, the frequency resolution $\Delta\nu$ in the Fourier transform:

$$\Delta\nu = \frac{1}{T} = \frac{1}{86,400} \sim 11.6 \mu\text{Hz} \quad (5.10)$$

However. Even longer, continuous data time series would be needed to resolve mode frequencies at low l 's where ridges are very narrow, and crowded.

\Rightarrow For $T = 10 \text{ years}$, $\Delta\nu = \frac{1}{T} \sim 3.18 \times 10^{-9} \text{ Hz}$ (3.18 nHz) \Rightarrow Such long times series are essential for precise mode identification.

Unfortunately, day-night cycle at a single observing station introduces side-lobes or ghosts (i.e. spurious peaks in the power spectrum) that make it difficult to correctly identify solar oscillations.

Fortunately, there are alternatives to overcome this difficulty.

Uninterrupted, long time series of observations (for both unimaged and imaged solar observing) can be achieved by:

1. Observing from geographic south poles during summer months (usually 10-12 days at max due to low Sun and/or severe weather)
2. Ground-based global networks of solar observatories:
 - Birmingham Solar Oscillation Network (BiSON) – unimaged
 - International Research on Interior of Sun (IRIS) – unimaged
 - Global Oscillation Network Group (GONG) – imaged
 - aiwan Oscillations Network (TON) – imaged
3. Observing from space-borne instruments – SOHO, SDO

5.14 Global oscillations network group (GONG)

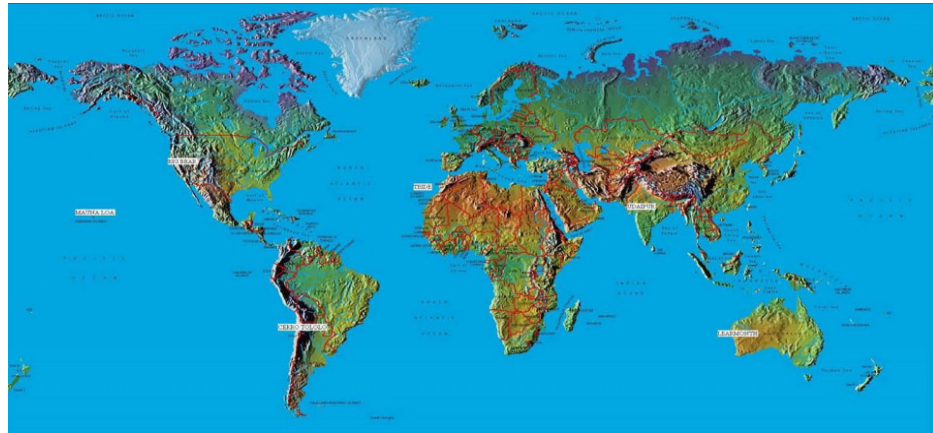


Figure 33: Six site network–Learmonth (Aus), Udaipur (India), Tenerife (Canarias), Cerro-Tololo (Chile), BigBear (USA), Mauna Loa (Hawaii)

- Extremely sensitive, and stable velocity imagers to obtain nearly continuous observations. 256×256 CCD deployed in 1995 (upgraded to 1024×1024 CCD in 2001)
- Frequencies for 500,000 modes determined, for $l \leq 150$ and $1 \leq \nu \leq mHz$
- Network started on 7 May, 1995 with > 23 year data analysed.

Space-borne observations need to be done from suitably located altitudes, and preferably at the sun-lit Lagrangian L1 point (on a line joining Sun & Earth at ~ 0.01 distance Dearth-sun ~ 1.5 million kms):

1. SOlar and Heliospheric Observatory (SOHO) (launched in 1995) – at L1 point, carries 3 instruments for helioseismology:

- Michelson Doppler Imager (MDI) on-board SOHO
 - Global Oscillations at Low Frequencies (GOLF)
 - VIRGO (Variability of solar IRradiance and Gravity Oscillations)
2. Solar Dynamics Observatory (SDO) (launched in Feb. 2010) – in a circular geosynchronous orbit 36,000 km above Earth (faces periods of several weeks when Earth briefly blocks Sun each day) - HMI

Additional advantage: Free from atmospheric degradations. Limitations: Once launched, no changes/repairs/up-gradations possible.

5.15 SOHO and now SDO carry out helioseismology from space



(a) Solar and Heliospheric Observatory (SOHO): A NASA-ESA Mission



(b) Solar Dynamics Observatory (SDO): A NASA mission

- a: Launched on 2 Dec 1995, longest-lived heliophysics mission. It is located at Sun-Earth L1 (Lagrangian point) of gravitational balance, 0.01 AU from Earth.
- b: Launched February 11, 2010, under "The Living With a Star program" at 102° west longitude in geosynchronous orbit of ~ 36000 km. SDO-HMI instrument for helioseismology and magnetograms Expected to last till 2020.

5.16 Probing the solar interior: methodology

Helioseismic data of oscillation frequencies are analysed in two ways:

- Forward method: a set of solar models for internal structure are constructed using the structure equations with different values of adjustable parameters. The model is then perturbed using a linearised theory to obtain the eigen-frequencies of solar oscillations. Theoretically computed eigen-frequencies are compared with the observed frequencies... never turn out to be perfect. Difficult to determine adjustable parameters uniquely due to correlations between different.

- Inverse techniques: The sound speed, density and rotation are deduced by inverting the observed oscillations. Requires a reference solar model to calculate the sound speed and density profiles inside the Sun for comparison of inversion results. However, the inferred profiles are not particularly sensitive to the choice of the reference model.

→ Preferred approach.

5.17 Inversion – sound speed and density

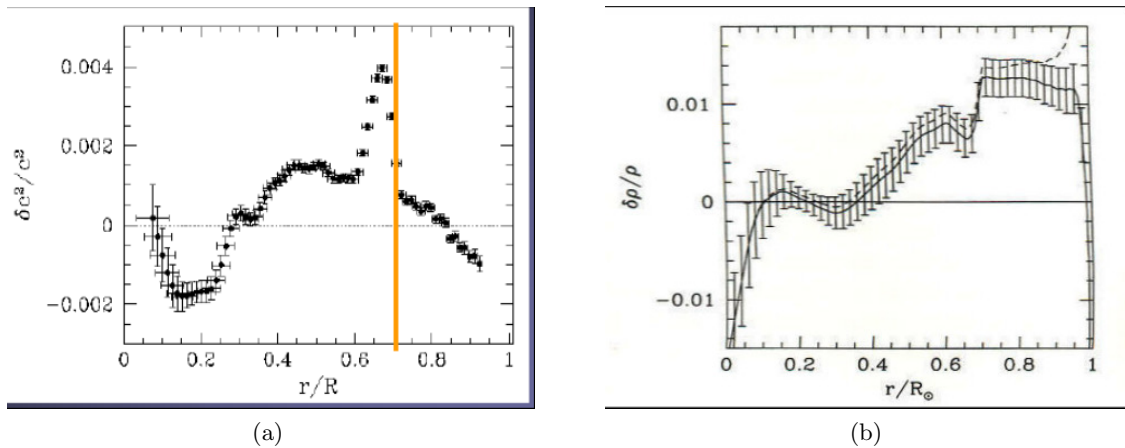


Figure 34: Relative difference in sound speed and density between 'helioseismology' and standard solar model

Problem areas: solar core, bottom of CZ, solar surface.

More Physics needed?!

Result from inversions and from standard solar model plotted vs. radial distance from Sun centre.

Note the difference between the SSM and the Sun is only 0.4%. Very good match!

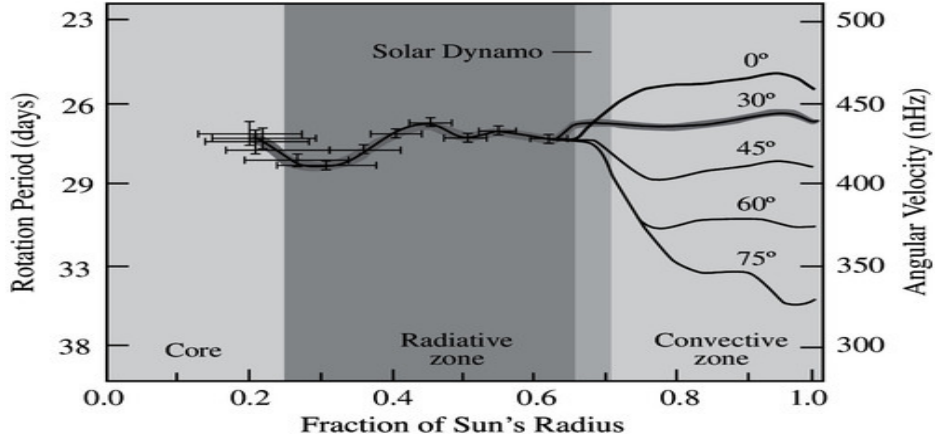
5.18 Possible reasons for small differences of helioseismic inversions from SSM

- The narrow peak at $0.67 R$ (beneath convection zone: Tachocline) is attributed to a sharp gradient in He abundance profile in the SSM. A small turbulent mixing can solve the problem. Strong rotational shear discovered at tachocline is likely to induce the required mixing.
 - The sharp decrease of the sound speed as compared to SSM at the boundary of the core at $0.25R$ may indicate over-abundance of He at the edge of the energy-generating core.
 - The steep increase of sound speed towards the centre can be understood if the He is less abundant in the core than in the SSM → possibly due to use of incorrect nuclear reaction rates. Or, it may be the result of macroscopic motions in the core induced by the instability of ^3He burning.

- The steep drop near the surface is due to uncertainties of outer layers in the SSM.. Also needs better observations near the surface but large degree (l) modes are difficult to detect to limitations of high spatial resolution observations.

5.19 Solar internal rotation with depth and latitudes

Rotation breaks degeneracy in m , i.e., splits frequencies ω due to m -dependence ($\omega \pm m\Omega$). Inversion allows to infer $\Omega(r, \theta)$ as a function of depth and θ . Depth of convection zone, internal rotation,



'tachocline' between radiative & convection zones: Site of transition between differential and solid-body rotation.

5.20 Results from helioseismology: summary

Depth of convection zone – With improved solar models, the present estimate for $R_{base} = (0.713 \pm 0.001)r_{sun} \Rightarrow 199700 \pm 700\text{km}$ from Sun's surface.

Tachocline or the interface layer – lies between radiative zone and convective zone at $0.70R_{sun}$ with thickness of $0.04R_{sun}$. This is where the differential rotation changes to solid rotation. Sun's magnetic field is believed to be generated by a magnetic dynamo in this layer, and the shear flow across it can stretch magnetic field lines of force and make them stronger.

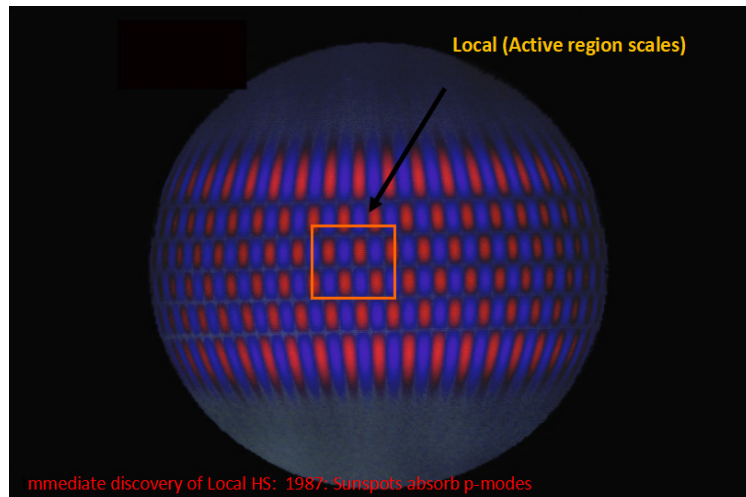
Abundance of Helium: 0.249 ± 0.003 .

Opacity: Significant increase ($\sim 15\%$) at the base of convection zone.

Central Temperature of the Sun: $(15.6 \pm 0.4) \times 10^6 K$.

Many discoveries from recent developments in global and local approaches of helioseismology.

5.21 Global v/s local helioseismology



Global (whole Sun)

1. Horizontal interference selects integer values of l
2. Entire sun is sampled
3. Spherical harmonics describe global waves
4. Does not get structure as function of longitude
5. Does not get non-symmetric latitudinal structure
6. Deals with $l \leq 180$

Local (Active region scales)

1. No horizontal interference, can have any wavelength
2. Sampling of local areas
3. plane wave approx.
4. longitudinal structure can be determined
5. Non-symmetric latitudinal structure can be determined
6. Valid for $l \geq 80$

5.22 Science objectives of local helioseismology

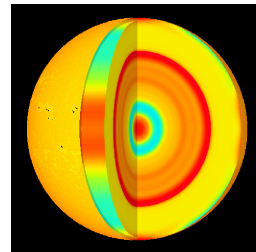


Figure 35: Interior Structure

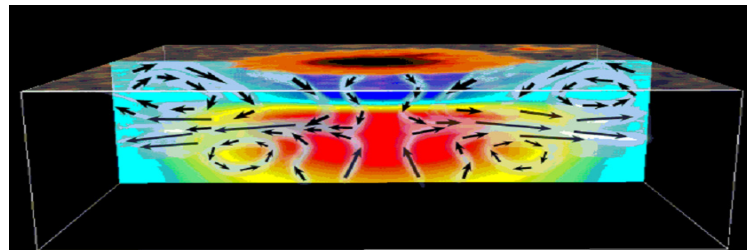


Figure 36: Sunspot Dynamics

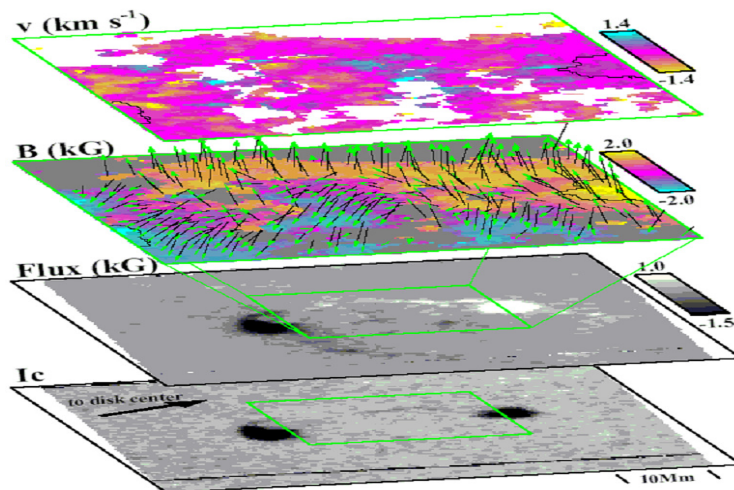
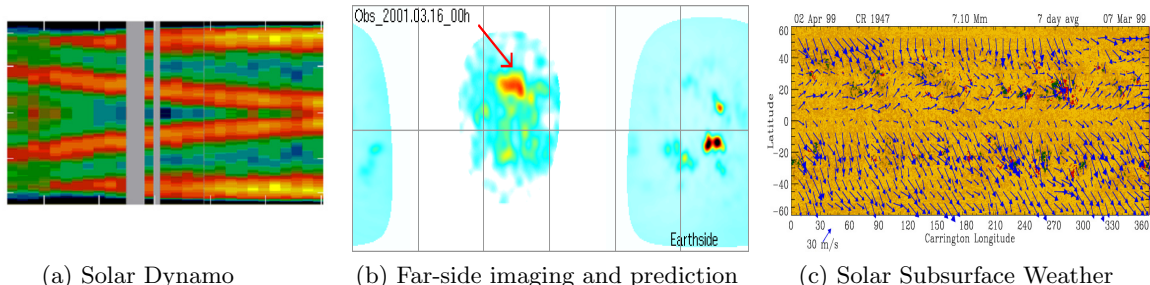


Figure 37: Magnetic Connectivity with interior



5.23 Asteroseismology

Asteroseismology refers to the study of the internal structure of stars through the interpretation of their oscillation frequency spectra in analogy with helioseismology. Reliable detection of oscillations on many low mass Sun-like stars have been made.

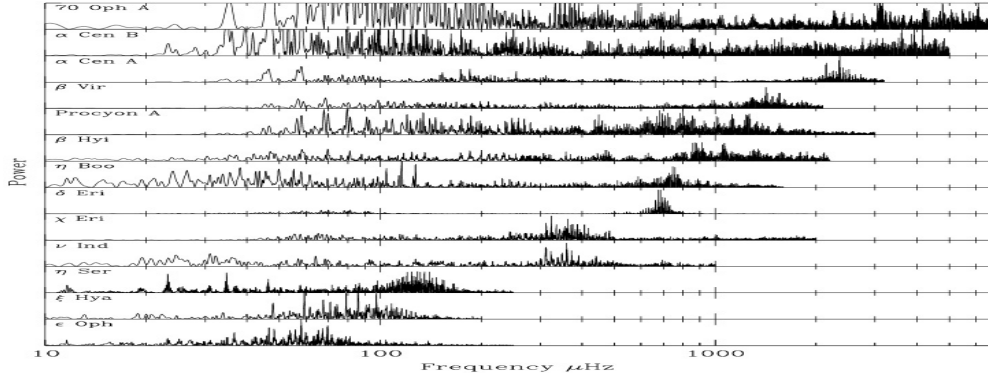


Figure 38: Frequency spectra of some solar-like stars covering the entire range in spectral type.

5.24 Sun as a star and asteroseismology

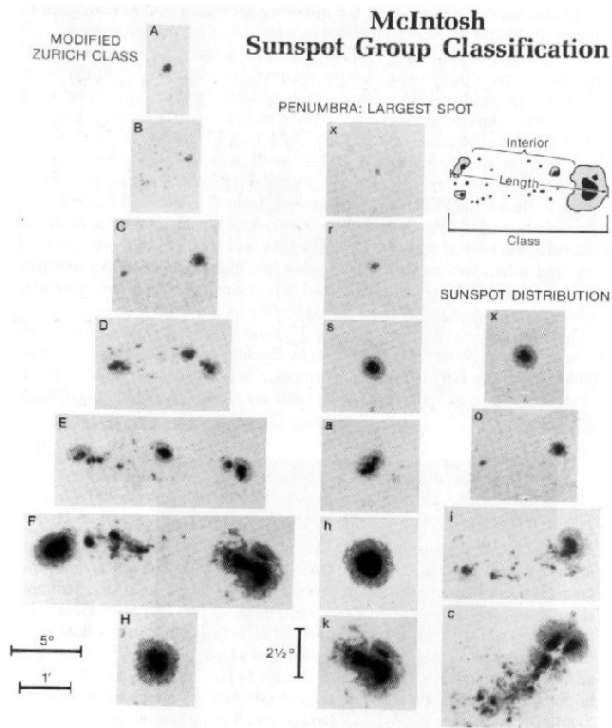
- In unimaged Sun (Sun as a star): low- l eigen-modes are observed from the time-series of integrated Sun-light: Due to cancellation effects at large scale, only modes with $l = 0, 1, 2$ provide signal. One gets a simpler power spectrum.
- Low l modes are important for 2 reasons:
 1. They reach deeper into the Sun or stars.
 2. These are the only modes detectable on other Sun-like stars.
- Asteroseismology Projects:
 - Space Missions: COROT, Kepler
 - Ground-based: ESO 3.6m (HARPS), ESO VLT (UVES), Network of smaller telescopes

6 Solar activity and magnetic cycles

6.1 Sunspots—signpost of solar activity

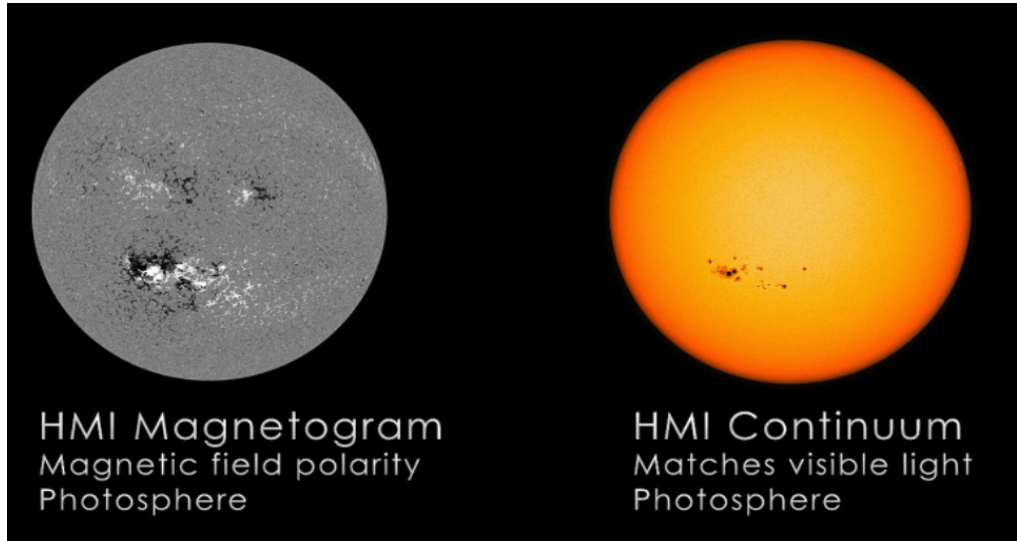
- Life--cycle of sunspot groups appears to follow a pattern. The first indication of sunspots forming is appearance of bright faculae. This indicates arrival of magnetic flux tube pushing the photosphere from sub-photospheric layers.
- Over few days, a spot forms, then one or more following (f-) spots with opposite magnetic polarity. Small spots merge and get bigger. Preceding (p-) spot develops a penumbra, and the overall magnetic field becomes dipolar.
- During the next weeks, the group grows further, and many small spots form between the main preceding and following spots; solar flare activity is likely.
- Large groups make one or more rotations as it gradually diffuses. The initial p-spot is the last to decay.
- The rapid formation (15–30 days) and slow decay (months) of sunspot groups is thought to indicate rapid rise but slow sinking of the turbulent flux tubes.

6.2 Various types of sunspots are observed



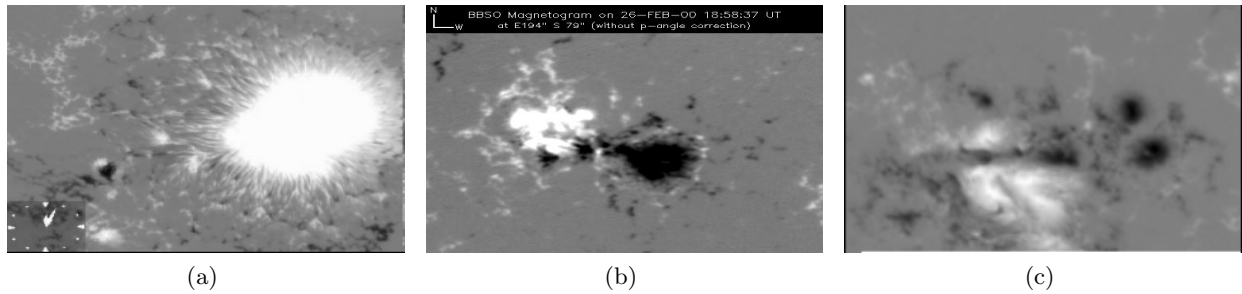
McIntosh classification is based on class (first letter), penumbra (second) and sunspot distribution (third). Class of sunspot group: single (A) , pair (B, C), or complex group (D, E, F), Penumbra of the largest spot in the group, and Sunspot distribution.

6.3 Sunspots are seats of strong magnetic fields as observed from solar magnetograms



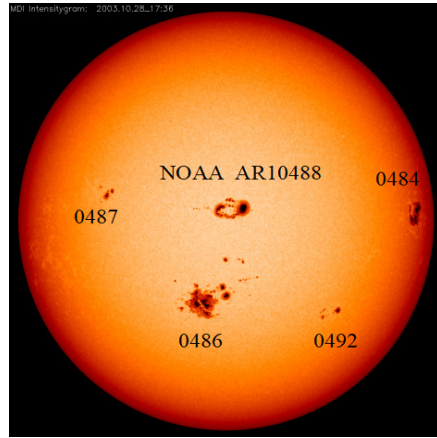
Magnetograms display not only the strong magnetic field structures of sunspots, and also away from them in weaker field regions all over the Sun's disk.

6.4 Active region classification based on magnetic complexity (Mt. Wilson)



1. ALPHA (α): A single dominant spot, often linked with a plage of opposite magnetic polarity.
2. BETA (β): A pair of dominant spots of opposite polarity (Bipolar, i.e., a leader and a follower).
3. GAMMA (γ): Complex groups with irregular distribution of flux polarities.
4. BETA-GAMMA ($\beta\gamma$): Bipolar groups having more than one clear N-S polarity inversion line.
5. DELTA (δ): Umbrae of opposite polarities together in a single penumbra.

6.5 Naming the Sunspot groups /active regions



Sunspot groups were earlier named/numbered by observatories.

Nowadays, active regions are named by NOAA; started on Jan. 5, 1972 with AR0001.

AR are numbered consecutively as they appear on the visible side of Sun's disk.

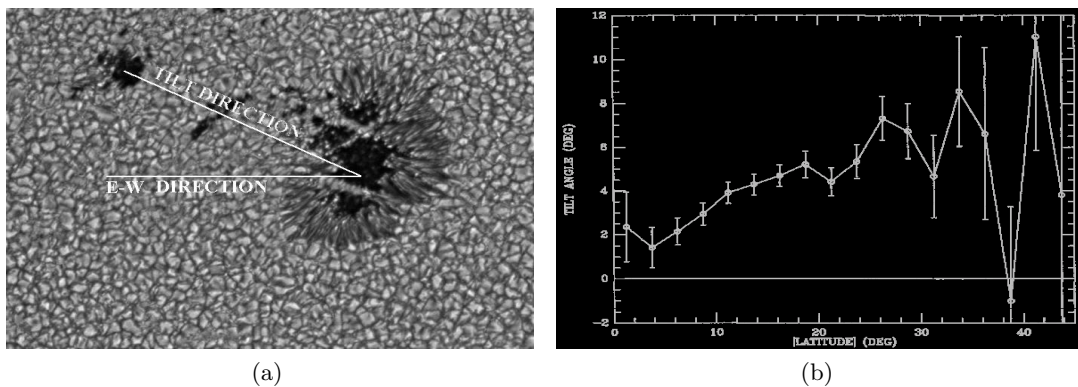
As Sun rotates, long lasting ARs may reappear. They are given new numbers...

On Jun 14, 2002, AR10000 named

For convenience only 4 digits are retained after 9999.. AR10484 is referred as AR048.

6.6 Active region tilt: Joy's law

Tilt of sunspot axis with the equator. Magnetic axis of Sunspot groups (active regions) are tilted to equator by $\sim 5.6^\circ$ and f-polarity spots poleward. This tilt increases with latitude.



6.7 Sunspot number – the indicators of solar activity

Sunspots are indicators of enhanced activity on the Sun. They have been reported even before telescope was invented in 1605, but ever since intensive regular observations have been carried out and their numbers counted. A pattern of their appearance and disappearance has been noticed.

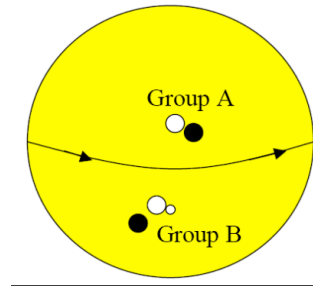
The number of sunspots are counted over the whole visible disk of Sun. These are plotted on daily, monthly, and yearly basis. Interesting trends from these plots emerge about Sun's temporal behaviour.

The Solar cycle was first discovered in 1843 by Schwabe who noticed a variation in average sunspot numbers from over 17 years of observations. Wolf compiled and constructed the cycles back to 1745, eventually pushing these reconstructions to the observations by Galileo and contemporaries in the early 17th century.

Monthly sunspot number is given by the Wolf Number (also known as the International sunspot number, relative sunspot number, or Zürich number) :

$R = k(10 \cdot g + f)$, where g is number of groups, f is the number of individual spots, and k is a correction factor that accounts for telescope size, atmospheric conditions, observer, etc.

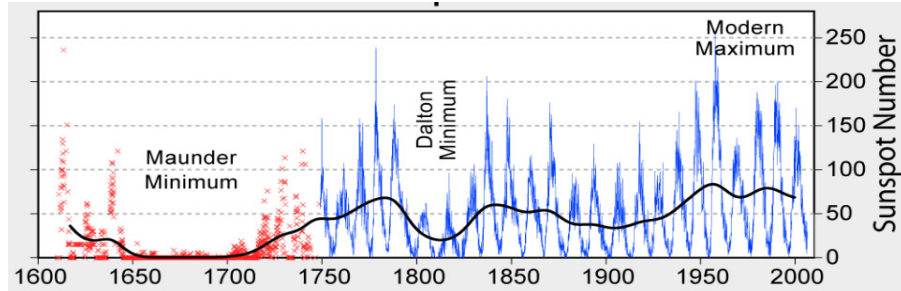
For example: The diagram contains two groups, Group A contains 2 spots, while Group B contains 3 spots. This implies, $g = 2$ groups, and $f = 5$ individual spots in these groups. Assuming $k \sim l \Rightarrow R = l(10 \cdot 2 + 5) = 25$.



6.8 11-Year sunspot activity cycle: the rise and fall of solar activity

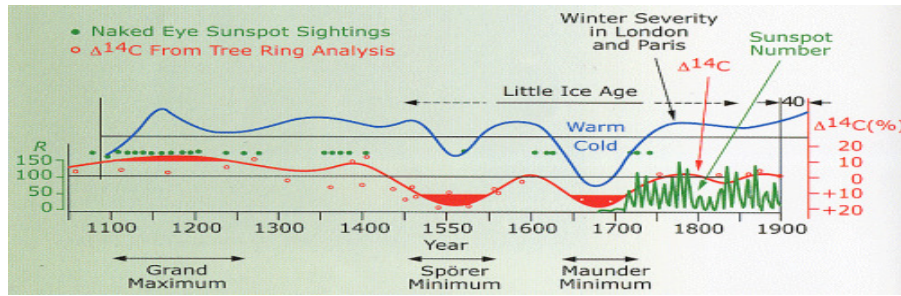
Sunspot numbers show a quasi-periodic behavior: the average length between maxima ~ 11.1 years, but varies in individual cases between 9 and 14 years. On average, spottedness rises to a maximum in ~ 4 years and then drops to a minimum in ~ 7 years – 11 years sunspot cycle.

Longest minimum on record, the Maunder Minimum (1645-1715), lasted ~ 70 years: Solar cycle appeared to have broken down. The long quiet period coincided with a Little Ice Age, in Earth's northern hemisphere. Low solar activity appears to have played a role in the 17th century abnormal cooling.



6.9 Long period solar activities

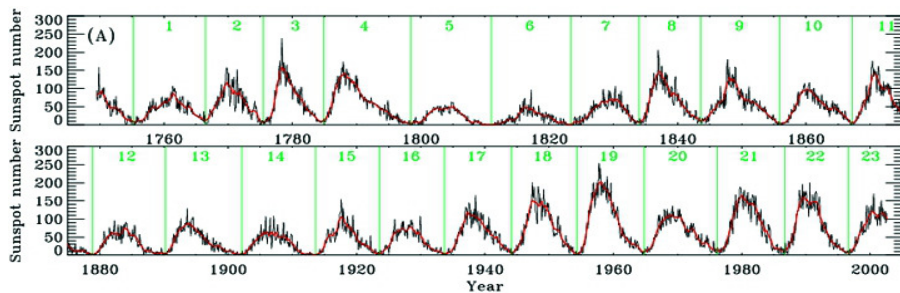
Late precambrian annual deposits (varves) laid down 680 million years ago show that 11yr cycles operated even in the past! Longer period 80 yr. (Gleissberg Cycle), 145, 290 yrs are also present. Grand maximum (1100–1250 AD), Sporer minimum (1450–1550) like features (like the long Maunder period of low activity).



The sunspot cycle revived itself after Maunder minimum in the early 18th century and has carried on since with the familiar 11-year period.

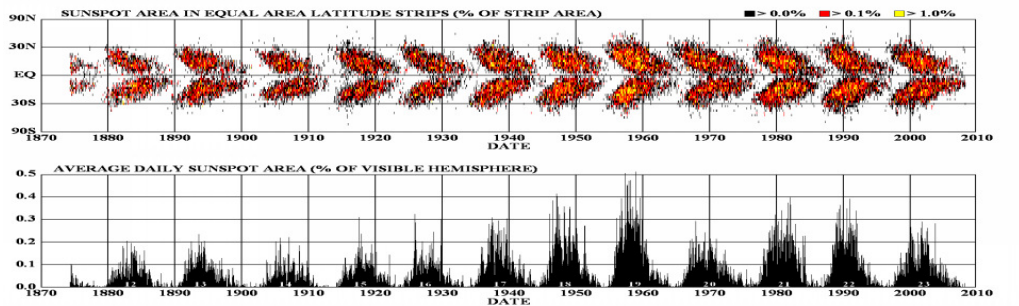
Sunspots observations have been more regular since early 18th Century. The solar cycles have been numbered from 1740 onwards.

The present cycle, numbered as 24th, peaked around 2013-14 and is now declining, expected to reach to the minimum in 2019, and then cycle 25 would follow. (Trends of successively lower amplitude sunspot cycles since 21st cycle).



6.10 The butterfly diagram: Equator–ward migration of active zones

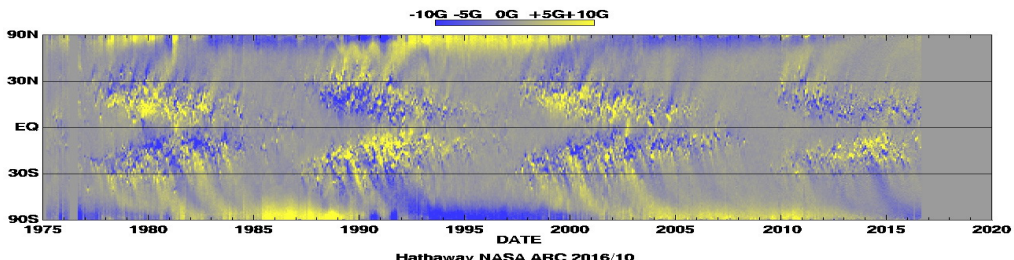
When locations of the sunspots on the visible solar hemisphere are plotted with time, an interesting butterfly diagram emerges: shows an equator-ward migration of active zones as the cycle advances (Spörer's Law). Variation of average spot latitude with progress of the cycle. The first spots of



a new cycle lie around $\pm 40^\circ$ latitude and rare occasions as high as $\pm 45^\circ$. There is asymmetry between the two hemisphere. There are times when spots belonging to two cycles are present as a new cycle begins.

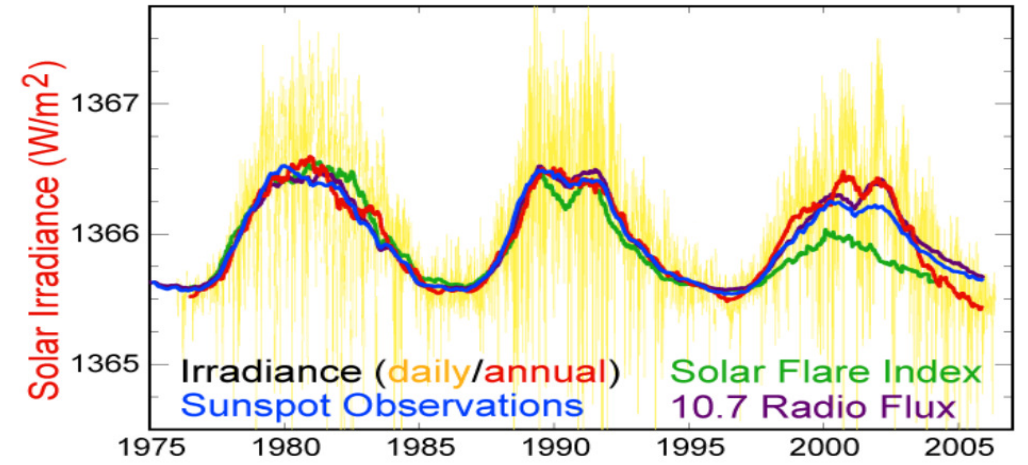
6.11 Magnetic butterfly diagram: poleward and equatorward flux motion

Solar magnetograms are available since 1975, and flux polarity, strength are plotted which shows interesting ‘equator-ward’ and ‘pole-ward’ motion of magnetic fluxes. It is found that polarity of the polar magnetic fields reverses at about the time of the solar activity maximum. Time vs. solar



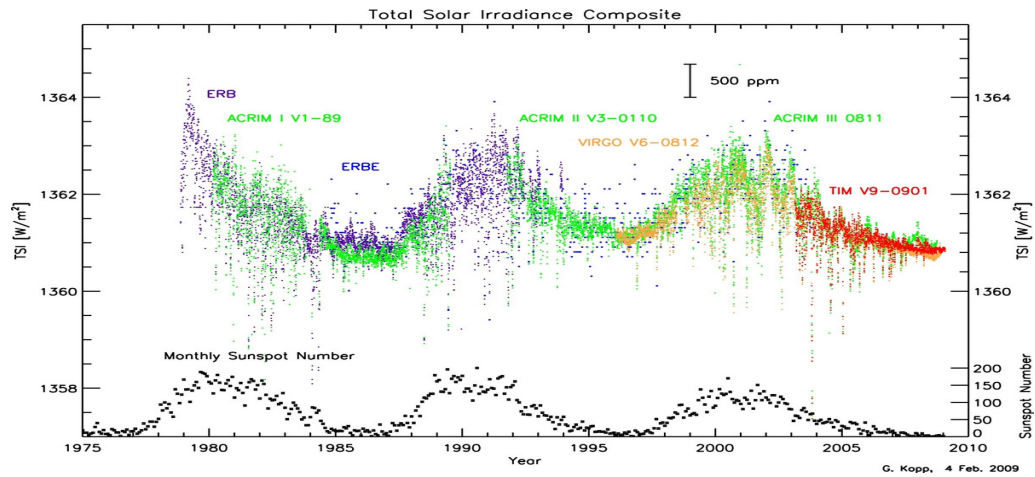
latitude diagram of the radial component of the solar magnetic field, averaged over successive solar rotation. The “butterfly” signature of sunspots is clearly visible at low latitudes.

6.12 Other indicators of solar activity



Similar plots result when other indicators of solar activity, such as, 10.7 cm Radio flux, flares, CMEs are plotted with time. Activity cycles 21, 22 and 23 seen in sunspot number index, TSI, 10.7cm radio flux, and flare index.

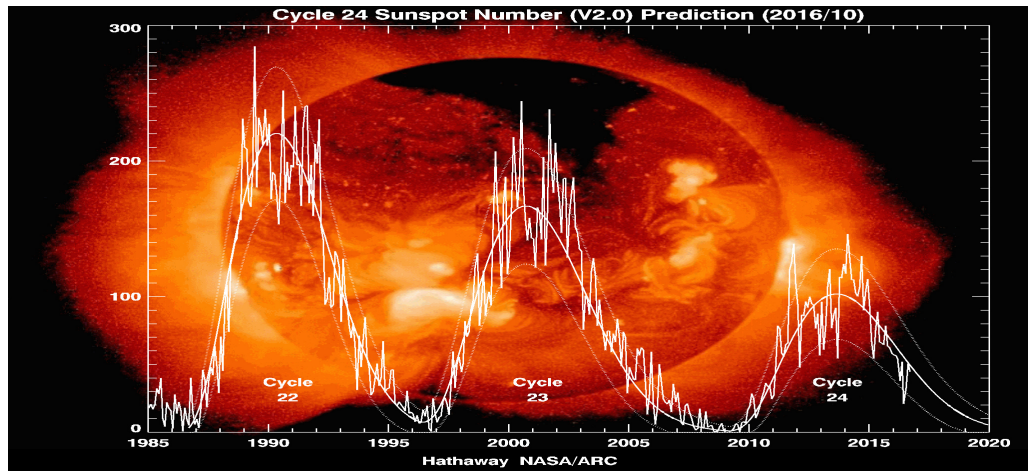
6.13 Solar constant (irradiance) – Not really a constant



Total Solar Irradiance (1978-2010): A three-decade record of total solar irradiance shows that variations in solar total irradiance correspond well with the cycle of sunspots with a very small relative amplitude of 0.04% .

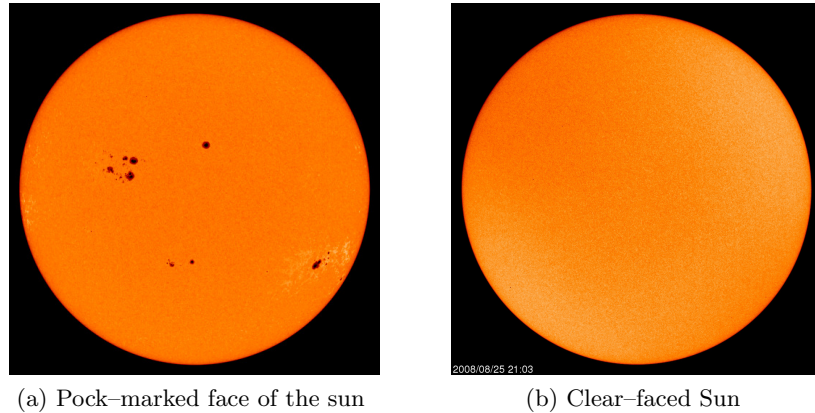
6.14 Smoothed sunspot numbers plotted over the recent solar cycles 22-24

The present Cycle 24 had its maximum (68.9 in August 2013), which was the minimum amplitude at in over the last 100 years (since Cycle 14 with a maximum of 64.2 in February 1906). If the trend continues, it may lead to a mini-Maunder Minimum and an ice-age as the one in 17th century!



6.15 The changing face of the Sun with the solar cycle

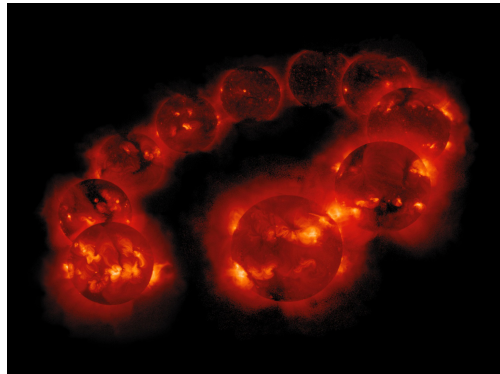
Solar Max 23 (high spottedness), Solar Min 23 (blank).



(a) Pock-marked face of the sun

(b) Clear-faced Sun

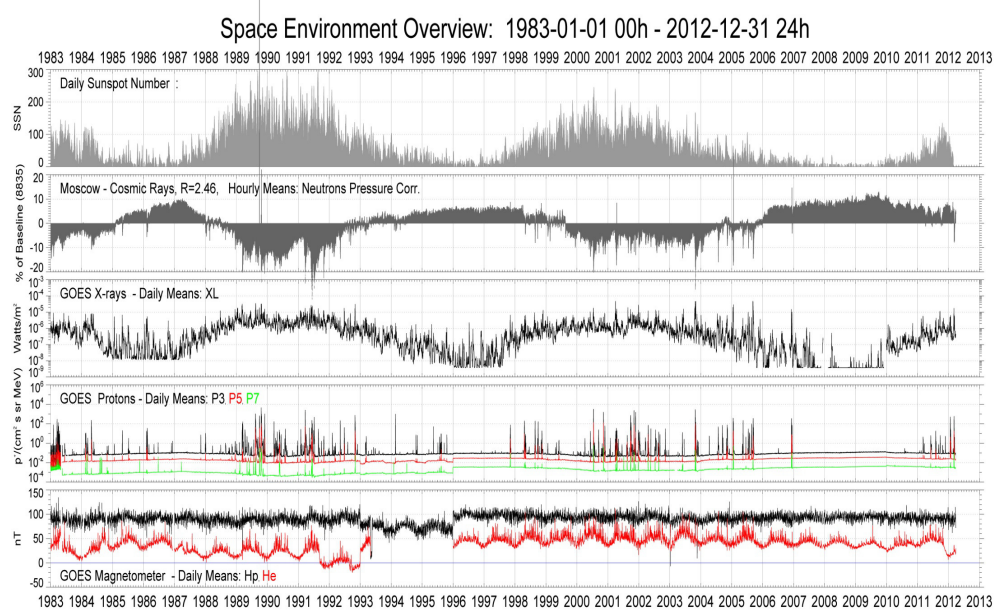
6.16 The changing face of the Sun with the solar cycle



Sun's hot X-ray emitting coronal plasma are controlled by the magnetic fields. So the X-ray images

reflect the global changes of large scale magnetic fields, with an overall decrease in brightness by 100 times.

A solar cycle: a montage of 10 years' (August 30, 1991-September 6, 2001) of Yohkoh SXT images demonstrating the variation in solar (magnetic) activity during a sunspot cycle.

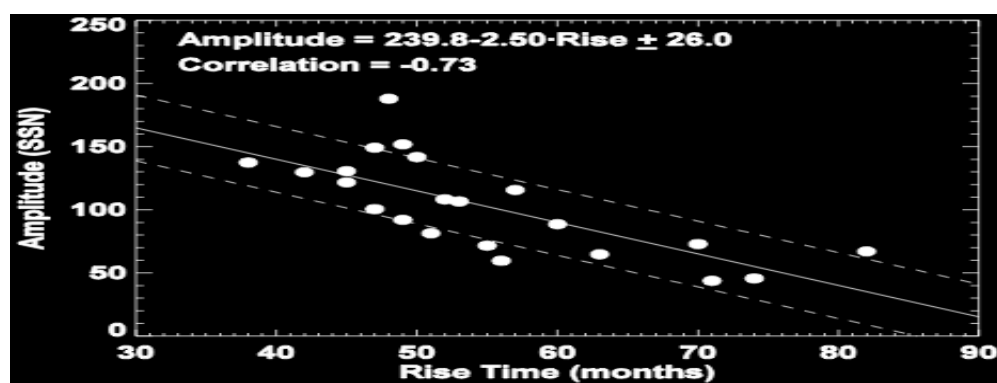


An overview of three solar cycles shows the relationship between the sunspot cycle, galactic cosmic rays, and the state of our near-space environment.

6.17 The Waldmeier effect

The sunspot cycles are asymmetric – the time to rise to maximum is less than the time to fall to minimum. Strong cycles take less time to reach maximum than do small cycles.

WE1 –Anti-correlation between cycle strength and rise time. WE2 –Correlation between cycle strength and rise rate (useful to predict strength of a cycle).

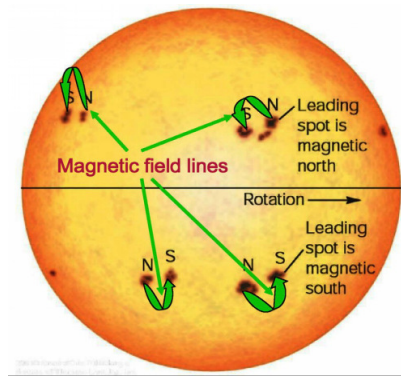


6.18 Magnetic polarity of Sunspot groups

This illustrates the way magnetic polarity typically behaves in a sunspot group.

In a given hemisphere, the leading & following spots in a group always have the same relative polarity during a given cycle.

The sense of this polarity is opposite in the two hemispheres, and it reverses at the end of each 11 year activity cycle (Hale's Law).



The effective period of reversal of Sun's surface magnetic field was thus found to be 22-years.

6.19 The main characteristics of a solar cycle

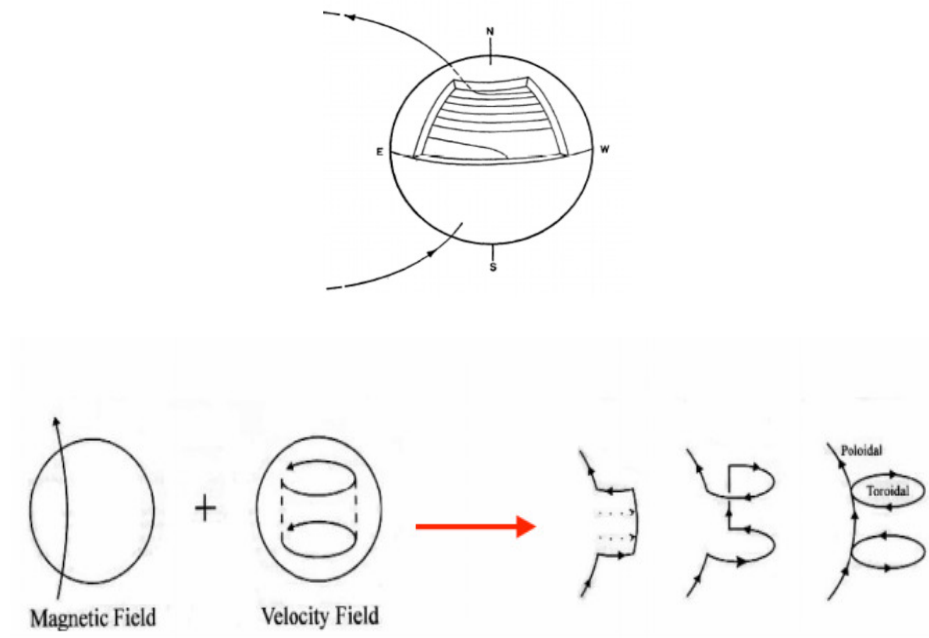
- 11-year quasi-period of the sunspot cycle
- Equator-ward drift of the active longitude as cycle progresses (Spörer's law)
- Pole-ward drift of magnetic fluxes
- 22-year magnetic cycle
- Equator-ward tilt of magnetic axis of sunspot groups (Joy's law)
- Reversal of polar magnetic fields near the time of cycle maximum

6.20 Understanding the solar cycle: Babcock's model, The $\alpha - \omega$ effect – the solar dynamo

The 11-year sunspot cycle is half of a 22-year Babcock–Leighton solar dynamo cycle, which corresponds to an oscillatory exchange between toroidal and poloidal solar magnetic fields.

Stage 1: Magnetic field is generated in deep convection zone at the tachocline.

Stage 2: The ω effect -submerged lines of force are drawn out by differential rotation $\omega = \omega(\theta)$ as fields are concentrated, and converted from poloidal to toroidal. Magnetic pressure $\frac{B^2}{8\pi}$ builds up.

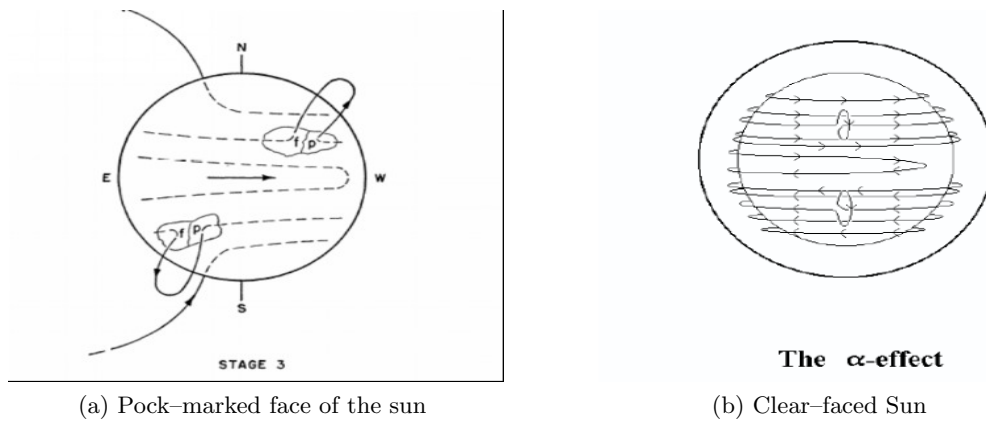


Stage 3a: Buoyancy—As field strength increases, $\frac{B^2}{8\pi}$ becomes significant, and buoyancy causes fields to rise from the tachocline to surface.

Stage 3b: Twisting of fields occurs due to solar rotation's effect on rising magnetic flux tubes from interior – Coriolis effect, or α effect. This twist makes sunspot groups obey Joy's law.

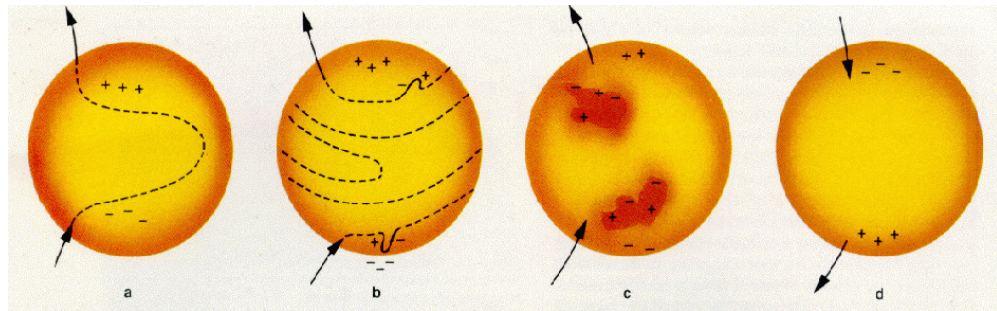
As the cycle nears end, leading fluxes drift toward the equator, where their opposite polarities mix and cancel; the trailing fluxes drift pole-ward and cancel and replace the existing flux polarity, and make the field reverse (Hale's law).

α effect regenerates poloidal field from toroidal field. And entire sequence repeats, except that all polarities have been reversed. Thus a complete magnetic cycle takes 22 years to complete.



This cycle repeats from stage 1. Solar convections draws field from tachocline to surface, Coriolis force then causes twist.

6.21 Babcock's $\alpha\omega$ model of the Sunspot cycle



a: Poloidal, b: Toroidal Spots appear, c: rift of fluxes, d: Flux cancels/reverse.

6.22 Some recent inferences—convection v/s tachocline shear layer

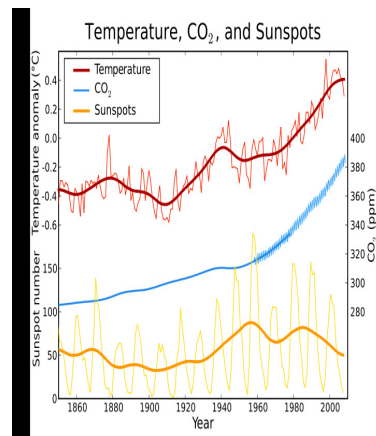
Although the tachocline has long been thought to be the key to generating the Sun's large-scale magnetic field, recent research raise some questions on this assumption.

Radio observations of brown dwarfs (very low mass stars) have indicated that they also maintain large-scale magnetic fields and may display cycles of magnetic activity.

The Sun has a radiative core surrounded by a convective envelope, and at the boundary of these is the tachocline.

Structure of brown dwarfs consists of a solar-like convective envelope that exists from core to surface. They lack radiative cores, therefore, have no tachocline, yet display solar-like magnetic activity. Therefore, it has been suggested that solar magnetic activity is only generated in the convective envelope, and tachocline may not be necessary for activity cycles.

6.23 "Global warming—Climate Change: Is the sun to blame"



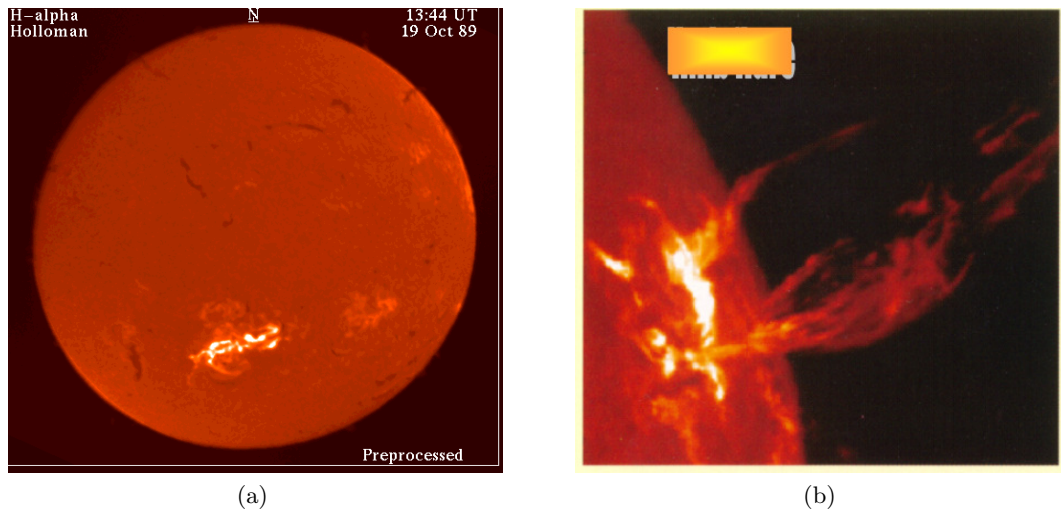
The Earth is gradually heating up in recent years. Opposing camps fight over whether the drivers are man-made or natural.

The Sun displays a variation of its irradiance, which is thought to influence the Earth's climate.

To what extent is the Sun responsible for the global warming seen in the last decades?

7 Solar explosive phenomena: flares

7.1 Solar flares



solar flare is a sudden explosive enhancement of energy over entire electromagnetic spectrum, from radio waves at the longest wavelength end, optical emission and to X-rays and γ -rays at the shortest wavelengths, occurring over localized region of solar atmosphere ($\sim 3 \times 10^9$ sq km, or 0.1% of the sun's visible hemisphere).

Energy release range: $10^{28} - 10^{32}$ ergs, duration: a few min to hrs in minor to major events, blast waves (Moreton waves), energetic particles and plasma ejection (CMEs) may also be associated.

7.2 First optical observations of flares

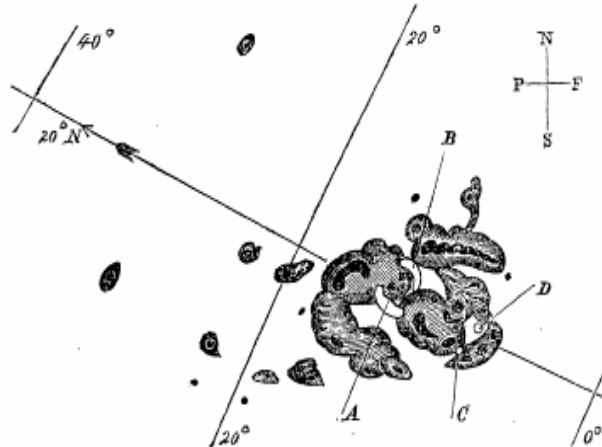


Figure 39: The Carrington's Flare

Richard Carrington and Richard Hodgson observed a flare for the first time on 1 Sep.1859 while projecting solar image by telescope through a broad-band filter.

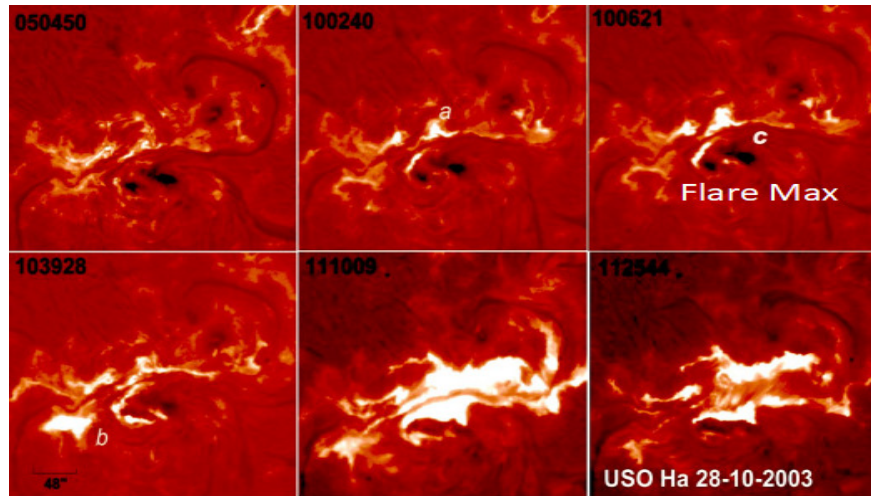
Intense white light brightening was observed on photographic plate within the sunspots, growing and fading in a few minutes.

It appears that accidentally a WL flare (photospheric) was involved in the 1859 discovery. Rare class of flares!

Chromospheric flares are observed by adding a narrow ($\approx 1 \text{ \AA}$) passband filter centered at H_{α} wavelength \Rightarrow allows the observation of even smaller flares.

Traditionally H_{α} was the main source of information about solar flares. (Other passband filters are also used from ground and space).

7.3 Some observational facts about flares in H_{α}

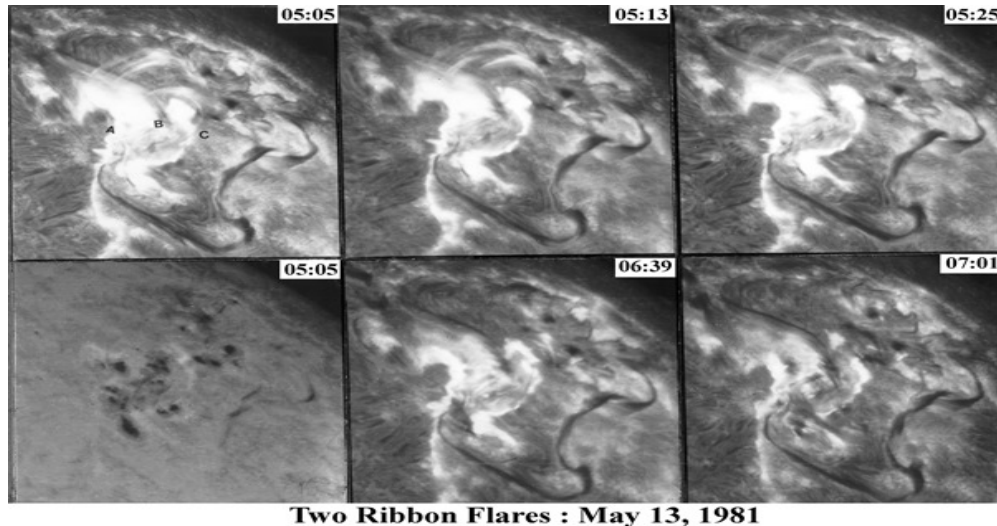


Bright elongated ribbons seen in H_{α} on either sides of dark filaments, tracing magnetic polarity inversion line.

Generally the ribbons, around magnetic inversion line, separate away with time: signature of magnetic reconnection!

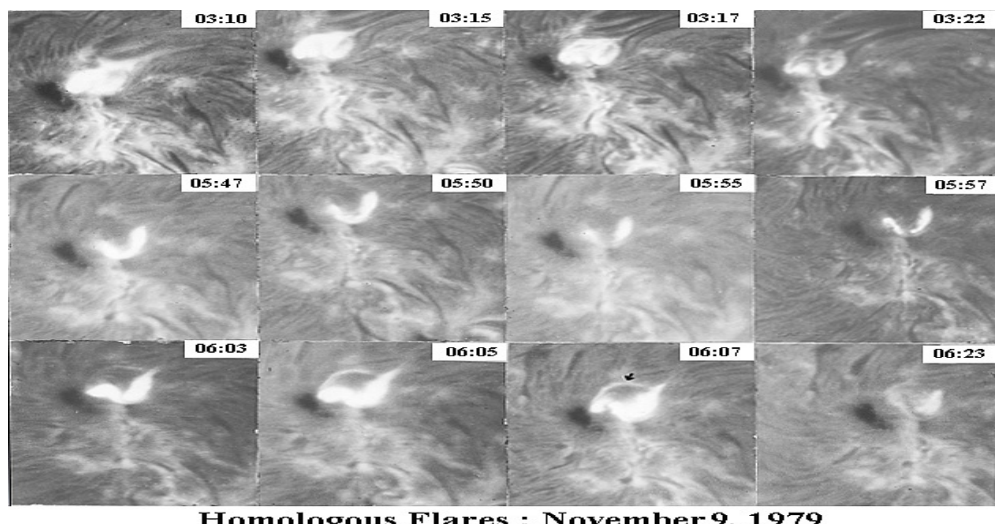
Flares seen in H_{α} from ground are also seen in EUV, and soft & Hard X-rays from space.

Flares mostly occur in "active regions (ARs)" i.e., regions of strong and complex magnetic fields. Large flares are less frequent than smaller ones. The frequency of occurrence of solar flares varies, from several per day when the Sun is particularly "active" to less than one every week when the Sun is "quiet", and follows the 11-year solar cycle as the sunspot numbers.



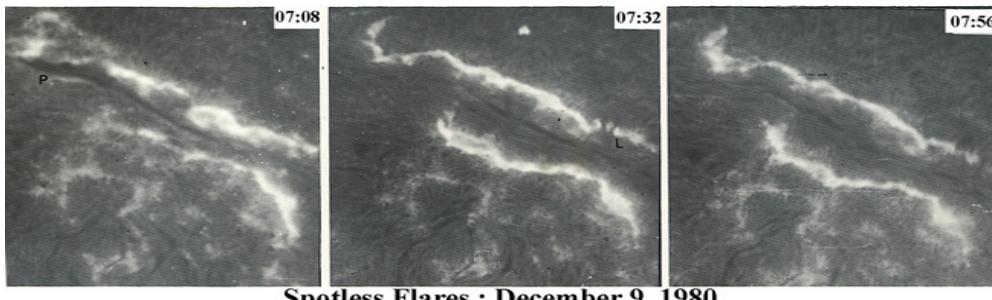
A large 2-ribbon flare was observed in Hale No. 17644 at around 03:46 UT (beginning missed). The post flare loops are seen around 05:05 UT. The upper loop system appears to connect the flare ribbons. The lower loop system was densely packed obscuring the underlying chromospheric features.

7.4 Homologous flares: repeated occurrence of flares in similar topology and location



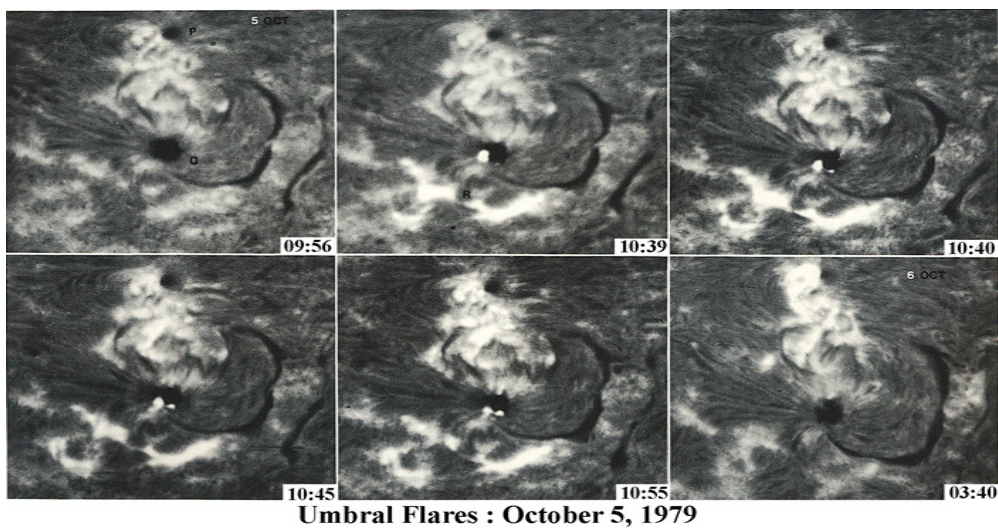


(a) Spotless flare: Filament eruption associated with flux emergence



(b) Spotless flare : Partial eruption of filament

Umbral Flares: A rare class of flares where a compact flare brightening is observed within or periphery of a sunspot umbra, while the extended flare ribbon is located outside. Usually, it is observed that expansion of flare ribbon is inhibited from moving towards large magnetic field regions.



7.5 Flare associated sprays (observed in limb flares)

Flare sprays are a type of eruption associated with solar flares. They involve faster ejections of material than eruptive prominences, and reach velocities of 20 to 2000 kilometers per second.



Figure 40: his and all previous $H\alpha$ sequences are adopted from “Photographic Atlas of the Solar Chromosphere”

7.6 Flare observations from space telescopes

Space telescopes observe wavelengths shorter than UV, which are completely absorbed by the atmosphere.

Since the 1970s, the GOES series of satellites observe the Sun in soft X-rays, and their observations became the standard measure of flares, diminishing the importance of the optical and $H\alpha$ observations and classification. Through the more recent years, Yohkoh, Hinode, SOHO, TRACE, and SDO.

Hard X-rays were observed by many different space instruments, recent one is the Reuven Ramaty High Energy Solar Spectroscopic Imager (RHESSI).

Space observations are important part of solar imaging with their incredible fine details that reveal the complexity of the solar corona.

Spacecraft may also employ radio detectors at extremely long wavelengths (as long as a few kilometers) that cannot propagate through the ionosphere.

7.7 Flares radiation enhancement occurs in many wavelengths

Flares produce radiation across the entire E.M. spectrum, including X-rays and radio emission. There are typically three stages to a solar flare:

1. Precursor stage: release of energy is triggered. $H\alpha$, SXR emission (preheating) detected.
2. Impulsive stage: protons and electrons are accelerated to energies $\gtrsim 1$ MeV. Radio waves, HXR, and $\gamma - rays$ are emitted.
3. Gradual or decay phase: gradual decay of SXR, $H\alpha$.

The duration of these stages can be as short as a few seconds or as long as an hour.

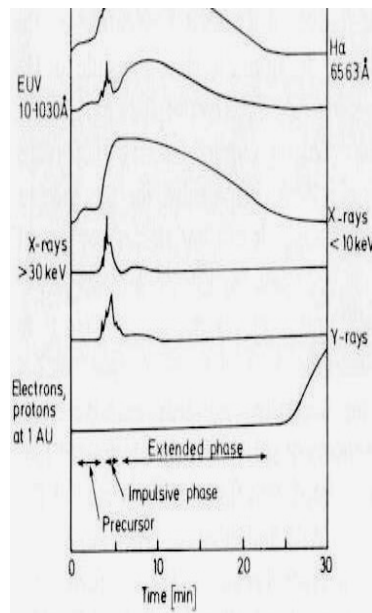
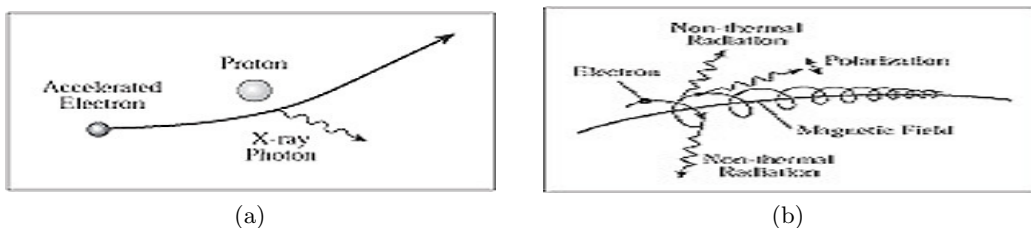


Figure 41: Schematics of different phases of a typical solar flare (Adapted from Kane 1974)

7.8 X-ray & radio emission (NON-thermal mechanisms)



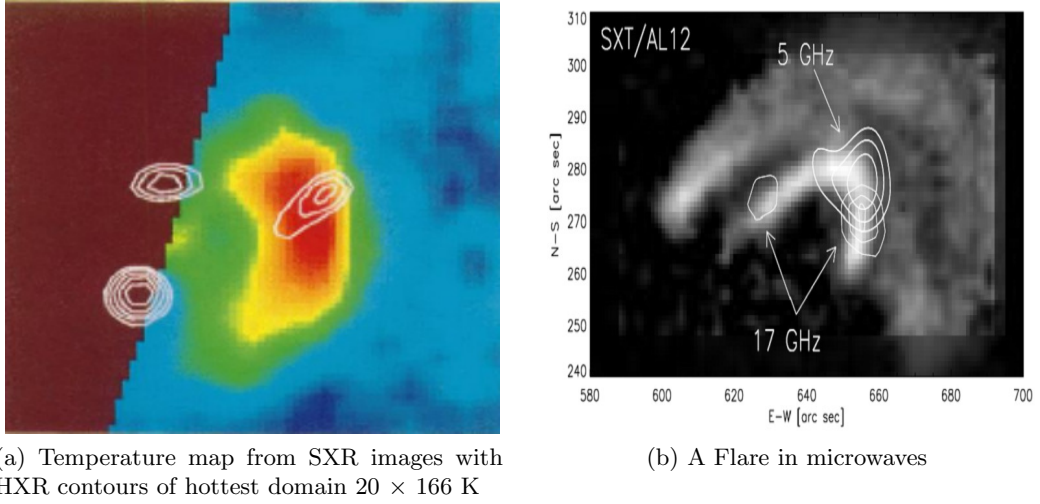
- a: When accelerated electron moving in corona encounters a proton, it is pulled toward the proton due to Coulomb attraction between them, bending the electron's trajectory and

altering its speed. In the process, the electron emits e.m. radiation (bremsstrahlung, German for "braking radiation").

- b: Relativistic electrons emit a narrow beam of synchrotron radiation as they spiral around a magnetic field. This emission is non-thermal radiation because the electron speeds are much greater than the thermal motion at coronal temperatures.

7.9 X-ray emission in flares

There are two basic components in the solar X-ray spectrum: (1) thermal SXR (1-10 keV) radiation of hot electrons, and (2) Non-thermal HXR (10-100 keV) radiation of relativistically accelerated electrons.



HXR often have a loop top source and double source at foot-points of the SXR loops and $H\alpha$ emission in the chromosphere.

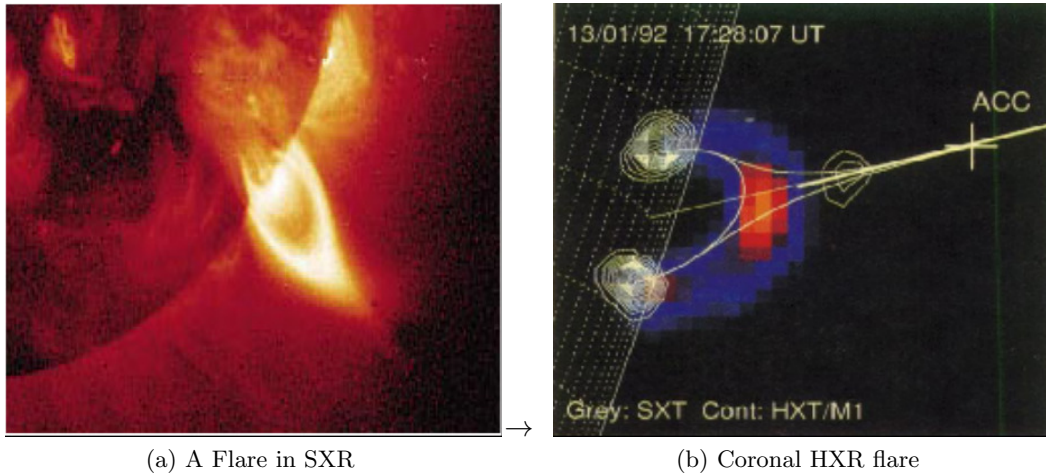
HXR are produced in the low corona and dense chromosphere by non-thermal electrons injected down along the legs of the coronal loop.

This observation is further supported by the similar time profile of radio waves at cm wavelengths also produced by non-thermal electrons.

7.10 X-ray emission in flares cusp geometry – reconnection site

A flare in SXR, showing cusp geometry, which may indicate the reconnection site where opposite polarity lines of force be present: requisite for magnetic reconnection (Yohkoh SXT observation).

Coronal HXR flare. Time of flight localization of acceleration site ("+") is consistent with the above-loop top location HXR source (Yohkoh HXT).



(a) A Flare in SXR

(b) Coronal HXR flare

7.11 The time profiles of a solar flare at HXR energies ($> 30\text{keV}$)

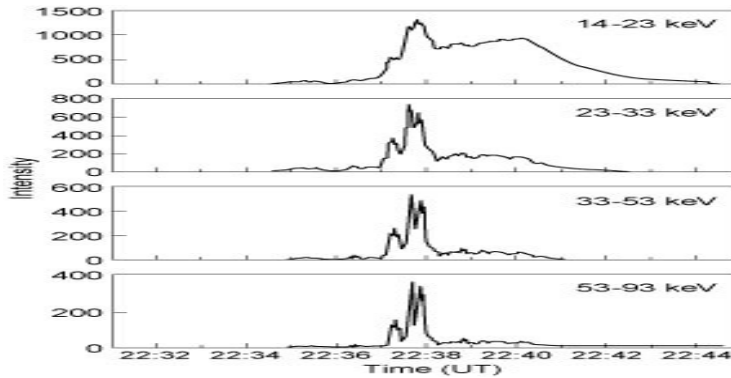


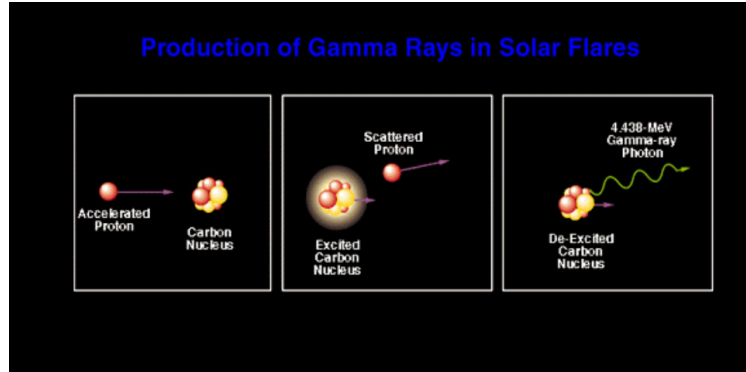
Figure 42: Yohkoh HXT

HXR is characterized by an impulsive feature that lasts for only ~ 1 minute, coinciding with accelerated relativistic electrons that emit non-thermal bremsstrahlung at HXR and non-thermal synchrotron radiation at cm radio wavelengths.

Lower energy radiation $< 30\text{keV}$ consists of two components – an impulsive component followed by a gradual phase that slowly builds up in the decay phase of solar flares when thermal radiation dominates. At even lower soft X-ray energies (about 10 keV), the gradual phase dominates the flare emission.

7.12 Flares and the γ rays

γ -rays have energies > 100 keV. Nuclear interactions of flare-accelerated protons and nuclei of carbon and other elements (energies 1-100MeV) in the dense layers below the acceleration site produce γ -rays at energies between 0.4 and 7.1 MeV. The nucleus is excited to higher energy level during each collision, and then emits γ -ray photons with specific energy characteristic of nucleus involved.



7.13 Radio emission from solar plasma

Radio wavelengths $\gtrsim 1 \text{ mm}$. Frequency is often used to characterize radio emissions, such that $\lambda(m) = 300/f(\text{MHz})$. Thus, e.g., $\lambda(1\text{mm}) \Rightarrow f(300\text{GHz})$. Radio emissions occur in perturbed plasma layers of the solar atmosphere in plasma frequency and are mainly due to free electrons moving in the magnetized plasma

$$f_{pe} = \frac{1}{2\pi} \sqrt{\frac{n_e e^2}{\epsilon_0 m_e}} \quad \text{or} \quad f_{pe} (\text{Hz}) \approx 9 \times \sqrt{n_e (\text{m}^{-3})} \quad (7.1)$$

Chromosphere: electron density drops from $2 : 5 \times 10^{17} \text{ m}^{-3}$ to $10^{16} \text{ m}^{-3} \Rightarrow$ correspond to plasma frequencies 4.5 GHz - 0.9 GHz (6.7 - 33.3 cm).

Corona: electron density varies with γ as

$$n_e = (1.55r^{-6} + 2.99r^{-16}) \times 10^{14} \quad (7.2)$$

where r in solar radii, density in m^{-3} .

This gives at $2 R_s$. plasma frequency $\sim 14 \text{ MHz}$ (21 m).

The energy density in radio waves is extremely small for astronomical objects, and measured in Jansky:

$$1Jy = 10^{-26} \text{ W Hz}^{-1} \text{ m}^{-2} \quad (7.3)$$

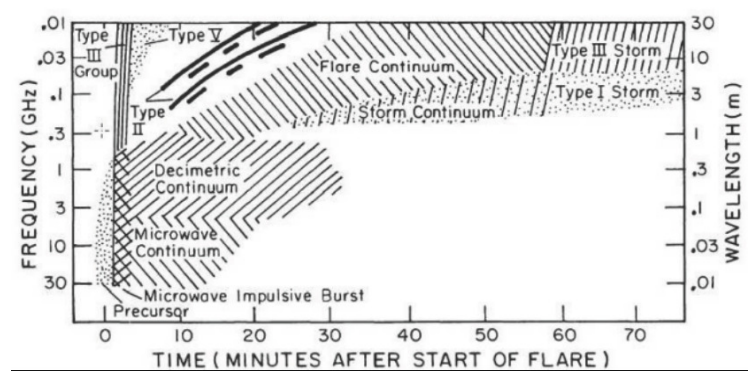
In solar astronomy, Solar flux unit (sfu) is used

$$1sfu = 10^{-22} \text{ W Hz}^{-1} \text{ m}^{-2} = 104Jy \quad (7.4)$$

7.14 Radio observations – radio bursts

During World War II, in 1942, British radar operators observed radiation that was interpreted as solar emission. In 1943 Grote Reber first reported radio observations of the Sun at 160 MHz.

Solar activity like storms and bursts related to the flares were revealed. Sun is now observed from 15 MHz up to 400 GHz. During solar flares, due to electrons released in corona, and plasma clouds moving away, a variety of radio bursts are observed. These bursts are structures in frequency space that change with time. Type I, II, III, IV, V etc.



 University of Glasgow

Type III Radio Bursts

Type III radio bursts are created by electrons and can be observed in space and/or at Earth (e.g. see Reid & Ratcliffe 2014 RAA).

Frequency (MHz)	Radius (R_{SUN})	Region
250 MHz	$0.16 R_{\text{SUN}}$	MID CORONA
10 MHz	$1.5 R_{\text{SUN}}$	CORONA
1 MHz	$7.5 R_{\text{SUN}}$	INTER-PLANETARY SPACE
0.15 MHz	$5.7 \times 10^9 \text{ m}$	ORBIT OF MERCURY
0.02 MHz	$1.8 \times 10^{11} \text{ m}$	PARKER SPIRAL LENGTH AT EARTH

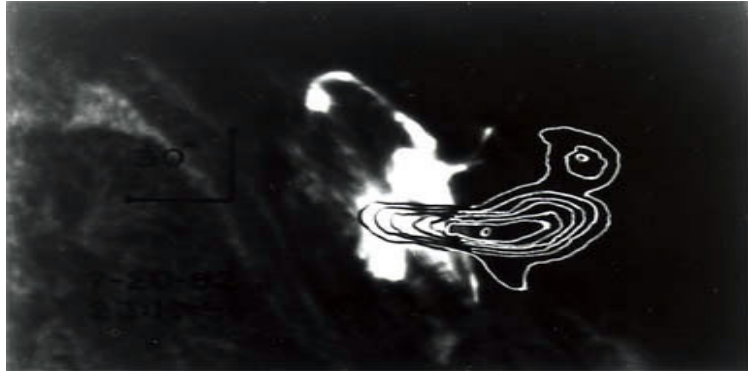
Solar Radio Burst Classifications

TYPE	CHARACTERISTICS	DURATION	FREQUENCY RANGE	ASSOCIATED PHENOMENA
I	Short, narrow-bandwidth bursts. Usually occur in large numbers with underlying continuum.	Single burst: ~ 1 second Storm: hours - days	80 – 200 MHz	Active regions, flares, eruptive prominences.
II	Slow frequency drift bursts. Usually accompanied by a (usually stronger intensity) second harmonic.	3- 30 minutes	Fundamental: 20 – 150 MHz	Flares, proton emission, magnetohydrodynamic shockwaves.
III	Fast frequency drift bursts. Can occur singularly, in groups, or storms (often with underlying continuum). Can be accompanied by a second harmonic	Single burst: 1 - 3 seconds Group: 1-5 minutes Storm: minutes - hours	10 kHz – 1 GHz	Active regions, flares.
IV	Stationary Type IV: Broadband continuum with fine structure	Hours - days	20 MHz – 2 GHz	Flares, proton emission.
	Moving Type IV: Broadband, slow frequency drift, smooth continuum.	30 – 2 hours	20 – 400 MHz	Eruptive prominences, magnetohydrodynamic shockwaves.
	Flare Continua: Broadband, smooth continuum.	3 – 45 minutes	25 – 200 MHz	Flares, proton emission.
V	Smooth, short-lived continuum. Follows some type III bursts. Never occur in isolation.	1-3 minutes	10 - 200 MHz	Same as type III bursts.

NOTES: In nearly all cases, drifting bursts drift from high to low frequencies.
The Frequency Range is the typical range in which the bursts appear – not their bandwidth.
The sub-types of type IV are not universally agreed upon and are thus open to debate.

@Copyright IPS AUSTRALIA

7.15 Flare and Radio Burst



Electrons are rapidly accelerated just above the tops of coronal loops during the early stages of the flare. They emit loop-like radio signals (white contours) over the $H\alpha$ flare-ribbons (Radio maps from the Very Large Array (VLA) at a λ 20 cm or ν 1420MHz). (From Ken Lang.)

7.16 Source of flare energy

E_T, E_g not enough to account for the flare energy release:

- *thermal* = $3 \cdot 10^{28}$ ergs

- $E_{gravitational} = 3 \cdot 10^{28}$ ergs; \Rightarrow in-fall mechanism
- $E_{fusion} \Rightarrow$ not possible in the low density atmosphere
- $E_{magnetic} = 10^{32}$ ergs

Source of Energy - MAGNETIC:

$$W = \frac{B^2}{8\pi} \cdot L^3 \quad (7.5)$$

This magnetic energy, is converted into heat, bulk K.E., particle acceleration, and radiation

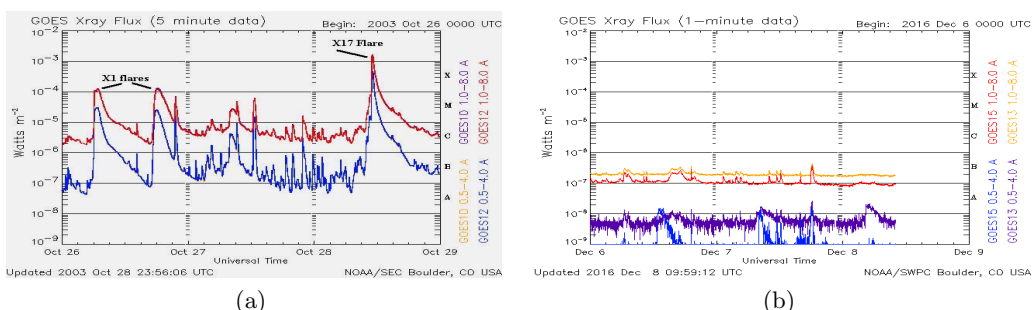
MHD Processes – Magnetic Induction Equation

7.17 Energy release in Solar flares occurs in various forms

FORM OF ENERGY RELEASE		LARGE FLARE (ergs)	SMALL FLARE (ergs)
Hydrodynamic Plasma Flow (I.P. ejections, shock wave, sprays)		4×10^{32}	-
Radiation	SXR, UV	5×10^{31}	$< 10^{29}$
	Optical (continuum)	3×10^{31}	-
	H α	3×10^{30}	10^{26}
	HXR	5×10^{26}	10^{24}
	γ -ray	2×10^{25}	-
	Radio	10^{24}	$< 10^{21}$
Accelerated Particles	Electrons	3×10^{31}	10^{27}
	Protons	3×10^{31}	-
Duration		Several minutes to hours	Up to several minutes

7.18 Flare classification in various observational categories

$H\alpha$ flare importance: based on both flare area and brightness in $H\alpha$. X-ray classification: Based on SXR data from monitoring satellites,



$H\alpha$ Class	Area ($10^{-6}A_H$)	Flux at 5000 MHz (s.f.u)	SXR class and flux in 0.1-0.8 nm range (watts perm^2)
S	≤ 100	5	C2 (2×10^{-6})
1	100-250	30	M3 (3×10^{-5})
2	250-600	300	X1 (1×10^{-4})
3	600-1200	3000	X5 (5×10^{-4})
4	≥ 1200	30,000	X9 (9×10^{-4})

7.19 Some large flares

The most powerful flare ever observed was the first one (Carrington flare) observed on September 1, 1859. It had produced auroras down to tropical latitudes, and disrupted telegraph systems. Effects of this flare were reconstructed using its traces left in Greenland. As compared with other events during the last 150 years it was placed at the top of all lists.

The flare and ultra-fast CME of August 1972 would have been a life-threatening event to Apollo astronauts if it had occurred during a mission to the Moon.

The largest solar flare measured with recent instruments occurred on November 4, 2003. This event saturated the GOES detectors. Extrapolating the GOES curve, it was estimated to be X28, and analysis of the ionospheric effects estimated to X45.

Other large solar flares: April 2, 2001 (X20), October 28, 2003 (X17.2 and 10). September 7, 2005 (X17), and an X9.3-class flare (SDO) on September 6, 2017 in the declining phase of current Cycle 24.

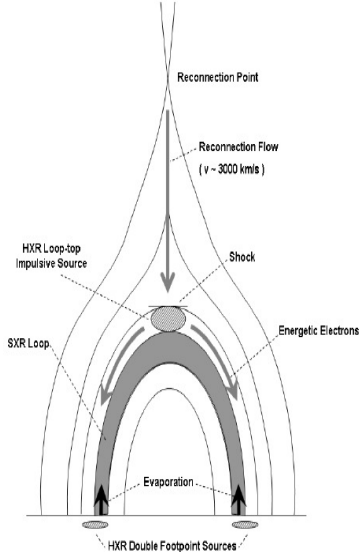
7.20 Fundamental questions about flares

- Where and how flare energy is stored? Photospheric flux motion believed to contribute to storage of energy in flux rope
- Why is the stored energy released? Only fragmentary data exist.
- Where is the flare energy released? At coronal sites.. indications exist.
- What happens to the energy after release? Enormous data exists in the form of chromospheric/ TR/coronal atmosphere from multi-wavelength observations.

7.21 Modeling the flares: CSHKP model

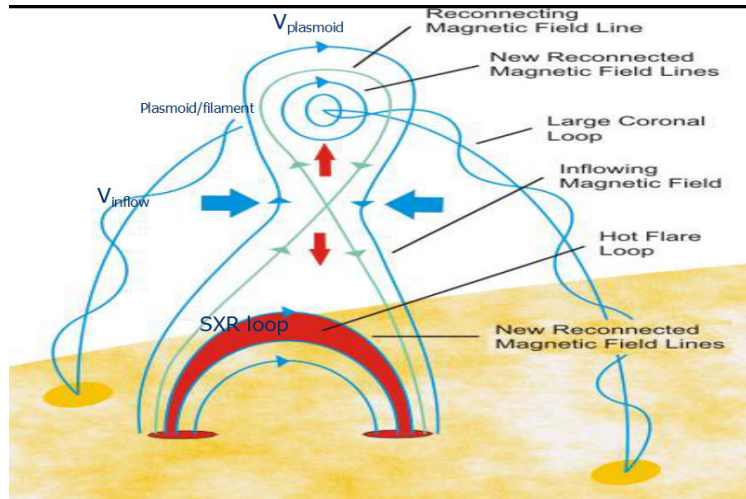
Primary source of flare energy is believed to be related to reconnection of magnetic field lines in corona at the top of a loop. This then heats the plasma, relativistically accelerates electrons that emit loop top HXR, microwaves, radio bursts. Solar flares affect all layers of the solar atmosphere . Some of the non-thermal electrons channel down the loop and hit the chromosphere and emit footpoint HXR by electron-ion bremsstrahlung.

Beams of accelerated protons entering dense atmosphere cause nuclear reactions $\Rightarrow \gamma$ -ray spectral lines .



Chromosphere is heated and rises into the loop giving a slow, gradual increase in SXR. This upwelling of heated material is chromospheric evaporation, and occurs in the decay phase of the flare.

Eruptive Flare Model (Shibata 1996): Flux rope through the core of the plasmoid is tied into the photosphere. Due to photospheric flux motions, flux rope gets stretched/twisted and thus magnetic energy is stored.



The coronal plasma under MHD Approximation is governed by Maxwell's equations, and fluid dynamical equations, which are linked using generalized Ohm's law as follows: First assumption plasma velocity $\nu \ll c$, Second assumption of MHD: Plasma in solar atmosphere is mostly neutral.

Generalized Ohm's law:

$$\vec{j} = \sigma (\vec{E} + \vec{v} \times \vec{B}) \quad (7.6)$$

Ohm's law provides the link between the electromagnetic equations and the plasma fluid equations.

$$\nabla \times \vec{B} = \mu \vec{j} \quad (7.7)$$

And Maxwell's Eqn in MHD approximation

$$\frac{\partial \vec{B}}{\partial t} = -\nabla \times \vec{E} \quad (7.8)$$

Therefore, we have from Ohm's law, and the magnetic Induction Equation

$$\frac{\partial \vec{B}}{\partial t} = -\nabla \times (\vec{v} \times \vec{B}) + \eta \nabla^2 \vec{B} \quad (7.9)$$

changes due to Advection, and Diffusion \Rightarrow depends on Reynold's number $R_m = \frac{\text{Term1}}{\text{Term2}} = \frac{L^2}{\eta \tau} = \frac{LV}{\eta} \gg 1$ for corona (diffusion is too low).

7.22 Solar coronal plasma conditions and magnetic reconnection

In solar corona, electrical conductivity is very large, i.e., resistivity η is very small, so magnetic Raynold's number is very large

$$R_m = \frac{LV}{\eta} = 10^8 \gg 1 \quad (7.10)$$

(advection much larger than diffusion). Thus, field-lines are frozen-in to the plasma, i.e., radiating plasma is a good tracer of magnetic field lines in the solar atmosphere . But, high R_m makes it difficult to release energy stored in stressed magnetic fields, as energy release process proceeds over diffusion time scale τ_D . Thus, the corresponding time scale for conversion of magnetic energy to heat is:

$$\tau_D \sim \frac{L^2}{\eta} = 10^{11} \text{ s} \gg \text{typically } 10^2 \text{ s for a flare.} \quad (7.11)$$

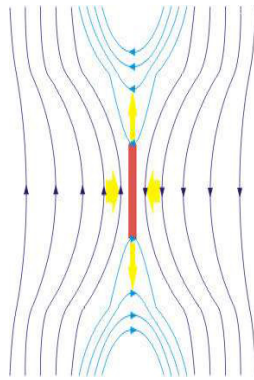


Figure 43: Magnetic Reconnection

Thus, either the length-scales L should be very small, i.e., $L \sim 1 \text{ km}$, or η large (possible in neutral sheets where classical concepts of electrical resistivity may not hold). Reconnection with rapid diffusion of magnetic fields could occur in a variety of ways.

7.23 Impact of flares on Earth

Solar flares strongly influence local space weather in the vicinity of the Earth.

Flares are associated with the ejection of plasmas and particles through the Sun's corona into outer space; and emit radio waves.

X-rays and UV radiation emitted by solar flares can affect Earth's ionosphere and disrupt long-range radio communications.

The soft X-ray flux of flares increases the ionization of the upper atmosphere, which can interfere with short-wave radio communication.

Soft X-ray flux of flares can heat the outer atmosphere, and thus increase the drag on low orbiting satellites, leading to orbital decay.

Hard X-rays and energetic particles can damage the spacecraft.

Direct radio emission at decimetric wavelengths may disturb the operation of gps, radars and other devices that use those frequencies.

Flares can produce streams of highly energetic particles in solar wind, known as solar proton event. In case of Earthward direction of ejection , associated particles penetrate into the magnetosphere causing auroras.

Massive solar flares may be accompanied with CMEs which can trigger geomagnetic storms that can disable satellites and knock out terrestrial electric power grids for extended periods of time.

The radiation risks posed by solar flares are a major concern for manned mission to Mars, the Moon, or other planets.

Most proton storms take at least two hours from the time of visual detection to reach Earth's orbit, giving astronauts as little as 15 minutes to reach shelter.

7.24 Forecasting of flares

Current methods of flare prediction are difficult and problematic, and there is no certain indication when an active region will produce a flare.

Many properties of sunspots and active regions correlate with flare productivity. For example, magnetically complex regions called δ -spots (inverted polarity structure) produce the largest flares.

A simple scheme of sunspot and its magnetic classification , or related to fractal complexity, is commonly used as a starting point for flare prediction.

Predictions are usually stated in terms of probabilities for occurrence of flares above M or X GOES class within 24 or 48 hours. Alerts are issued on daily basis by NOAA, USA, and other agencies.

One can check websites of ground- and space-based missions to checks the state of the Sun. (Also, www.spaceweather.com)

8 Solar explosive phenomena: CMEs

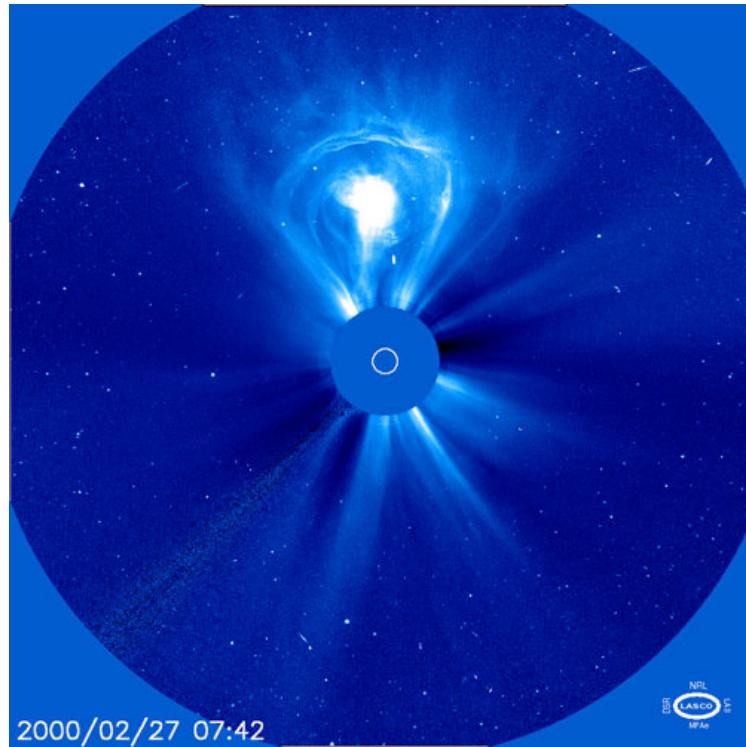
8.1 Coronal Mass Ejections (CMEs)

Coronal Mass Ejections (CMEs): large plasma clouds propagating away from Sun, discovered in December 1971 by coronagraph onboard OSO-7 and SkyLab, while flare was already discovered in 1859. The historical transients visually observed during TSEs are now interpreted as such.

In late 1995, SOHO was launched and two of its three LASCO coronagraphs still operate. LASCO has detected well over 104 CMEs: https://cdaw.gsfc.nasa.gov/CME_list/.

The white light LASCO observations are accompanied by SOHO- Extreme Ultraviolet Imaging Telescope (EIT), observations on disk at coronal wavelengths. In 2006: STEREO-A&B.

WL coronagraph MLSO and in green line from Sac Peak, and Norikura, Japan. A CME (top bright loop). An occulting disk on-board SOHO-LASCO (Large Angle Spectrometric Coronagraph) blocked the intense photosphere (white circle). (NASA ESA-SOHO LASCO).



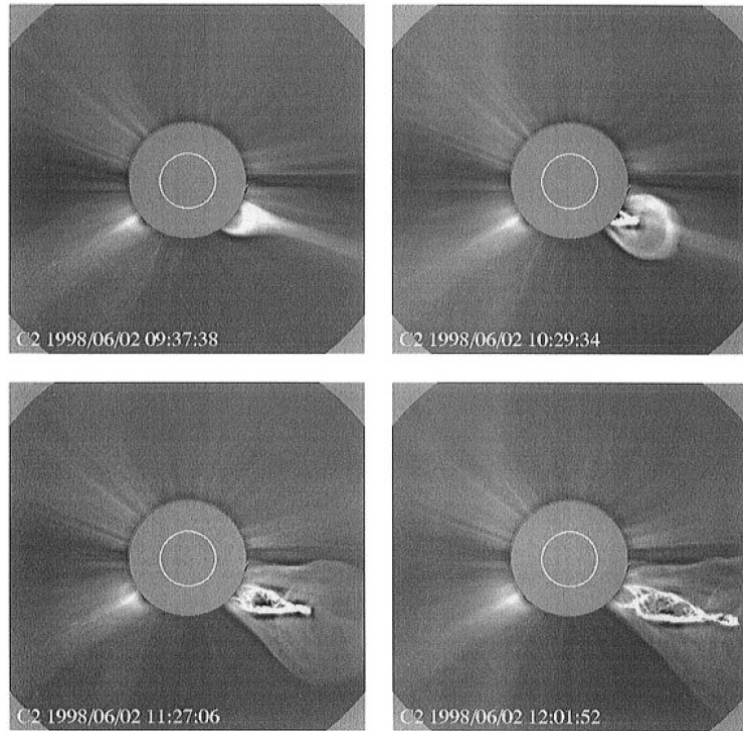


Figure 44: Evolution of a "classic" CME observed by the LASCO C2 coronagraph on 2 June 1998.

Structures just above the prominence, suggest a flux rope. Most of the matter or mass in the mass ejections originates from the lower atmosphere and thus is not "coronal mass".

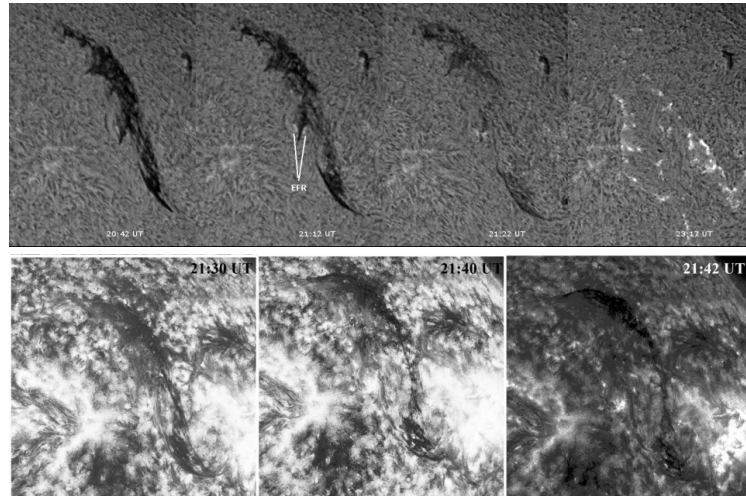


Figure 45: Filament eruption in GONG $H\alpha$ along with SDO/AIA EUV 304 \AA – CME in 171 \AA at 21:55 UT (Source region on the disk of Sun)

8.2 Properties of CMEs

Measured properties of CMEs include their occurrence rates, locations relative to the solar disk, angular widths, speeds and accelerations, masses, and energies. There is a large range in the basic properties of CMEs. Based mainly on sky plane observations (so may be affected by projection effect) – Stereo observations tried to circumvent this drawback.

Typical mass: $5 \times 10^{12} - 5 \times 10^{13}$ kg (from intensity to electron density ne from Thomson scattering, and also from radio and X-ray observations)

Speed: < 10 to ≤ 2500 km/s (ranging from < sound speed to > Alfvén speed)

Typical Kinetic Energy: $10^{20} - 10^{25}$ J (similar as large flares)

CME Mass and K.E. may have solar cycle dependence

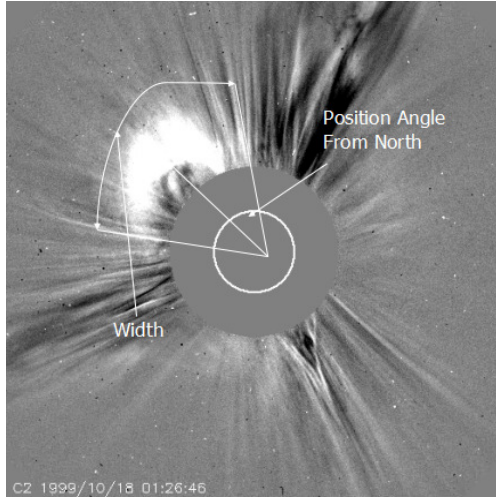
Average Width $\sim 70^\circ$ (from narrow CME 2° to halo CME 360°) They accelerate and then decelerate

Temperature: 8000 K (core) to 2 MK (front)

Rate of occurrence: Solar Minimum: One in two days; Solar Max: a few per day.

8.3 Morphological attributes of CMEs

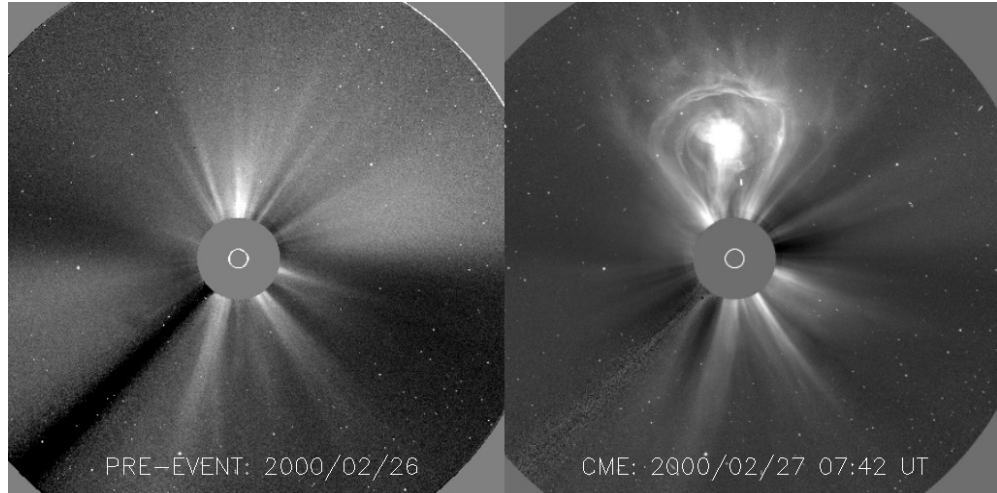
Angular Width, P-angle, Speed, Acceleration



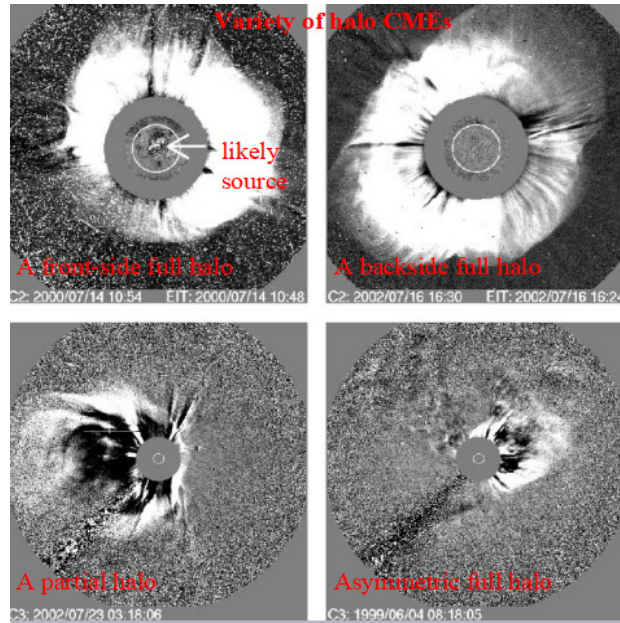
8.4 Substructures of CME

CMEs exhibit a variety of forms: Classical "three-part" structure interpreted as frontal leading edge, part of a flux rope of compressed plasma, followed by a cavity of low density, surrounded by a dense core, i.e., bright filament/prominence.

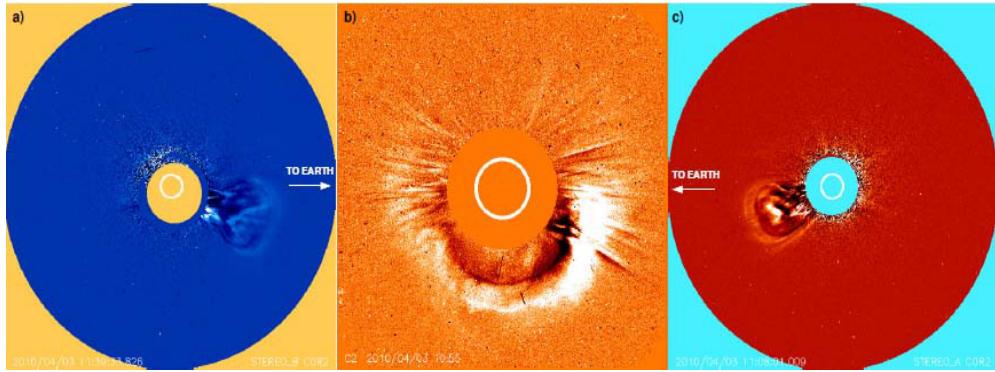
Some CMEs display more complex geometry, as narrow jets, or appear arising from pre-existing coronal streamer blowouts, halo CMEs, or as global eruptions.



Halo CMEs appear as expanding, circular brightenings that completely surround the coronagraphs' occulting disk. If Earth-ward, they are geo-effective. The source regions of frontside halo CMEs are



usually located within a few tens of degrees of Sun's center. Associated activity on the solar disk help to distinguish the front or backside launch of halo CME wrt observer, but can be mistaken if no surface association observed. The "geoeffectiveness" of halo CMEs depends on the source location on the disk.



8.5 Images of the same Earth-directed CME obtained from three different viewing locations

- a: CME observed from STEREO/COR2-B on 3 April 2010/11:39 UT
- b: from LASCO/C2 at 10:55 UT
- c: from STEREO/COR2-A at 11:08 UT

The STEREO A&B spacecraft were $\sim 70^\circ$ in longitude from the Sun-Earth line, and $\sim 140^\circ$ from each other at that time. The change in appearances of the same CME demonstrate the need to consider perspective in measuring CME properties.

8.6 CMEs association with flares and filaments

CMEs are often associated with other forms of solar activity, Solar flares, Eruptive prominence, X-ray sigmoids, Coronal dimming, Moreton waves, Coronal (EIT) waves (bright fronts propagating from the location of the eruption), Post-eruptive arcades, etc.

CMEs originate from the closed field line regions, but the magnetic structure has to be torn off from the Sun and the field must open locally.

CME may reach 1 AU with one or both ends of the magnetic fields still tied to the Sun. Thus the role of reconnection to cut the field lines behind a CME is an important question.

CMEs carry away the excess flux produced during the solar cycle accumulated at low latitudes in the regions of closed magnetic loops. (Solar wind removes flux only from the regions of open field lines, while ejection of large magnetic clouds (CMEs) may take care of getting rid of closed flux.

8.7 Association with flares

It was generally accepted that solar flare was the cause of interplanetary disturbances and major space weather effects on Earth. When interplanetary shocks were discovered by Mariner 2 in 1960s, they were expected to be blast waves from solar flares.

Similarly, when CMEs were discovered in 1973, they were also expected to be flare-driven, but later they were established to be a separate and main phenomena responsible for interplanetary shocks and geomagnetic storms.

There is no one-to-one relationship between CMEs and flares. Many CMEs are associated with solar flares, but many are not, and most flares are not associated with CMEs. When CMEs and flares occur together, the CME onsets observed to precede the flares in many cases.

Now it is generally accepted that CMEs and flares are part of a single magnetically-driven "event". Therefore, it is more appropriate to consider a unified model that accounts for both.

8.8 Association with eruptive prominences

Prominences are observed in coronagraphs often as the bright, central core of the CME structure (the filament component of the classic three-part CME). Prominences are believed to be caused by the formation of a flux rope low in the magnetic structure that eventually erupts to form the CME.

Many CME onset models (e.g., flux cancellation, mass loading) require the presence or formation of a prominence in order for the CME to erupt.

CMEs are more associated with eruptive prominences than flares. Only $\sim 40\%$ of CMEs have an associated flare close to the site of the ejection, before, during or after the lift-off of the CME.

For $\sim 70\%$ of ejections a disappearance of a dark filament or eruptive prominence has been identified. Filaments are thus progenitor of CME.

CMEs with filament eruptions: Substantial Flux emergence before filament eruption. But cases of CMEs also observed without flux emergence. (emergence, shear, twist)

8.9 Where and how do CMEs originate?

A lot of CME-related models have been developed to describe their pre-eruption structures, or, progenitors, their initiations, and their eruptions.

CMEs originate from closed field regions: (i) Active Regions (ii) Filament regions (iii) Combination of AR/Filament regions, (iv) Trans-equatorial interconnecting regions.

Several CME models to describe pre-eruption structures (or progenitors), initiations or trigger, and eruptions based on observations.

Some fundamental questions - What causes a CME to erupt in the first place. Proximity of a CME site to coronal holes, (ii) magnetic shear (iii) filament helicity, sigmoids. What is the exact physical relationship between CMEs and flares? How are CMEs accelerated? What is the role of reconnection?

In order to disentangle the various processes around CME initiation new observations with signifi-

cantly better resolution are required.

8.10 Sigmoid configuration as potential flare/CME site

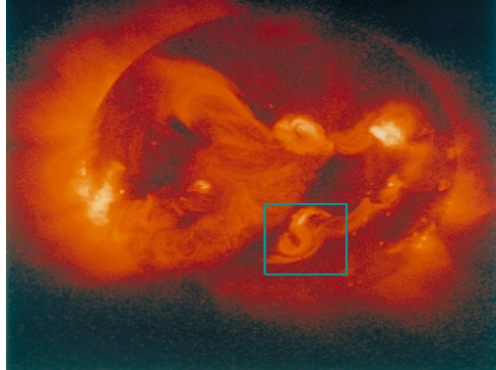


Figure 46: YOHKOH Soft X-ray Telescope (SXT) image taken on 8 June 1998.

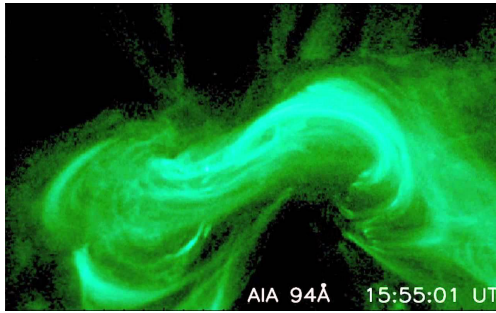


Figure 47: SDO-AIA image

When the coronal magnetic fields get twisted into an S, or sigmoid, shape, they become prone to destabilisation. Statistical studies indicate that the appearance of such a large S or inverted S shape in soft X-rays is likely to be followed by a CME in just a few days.

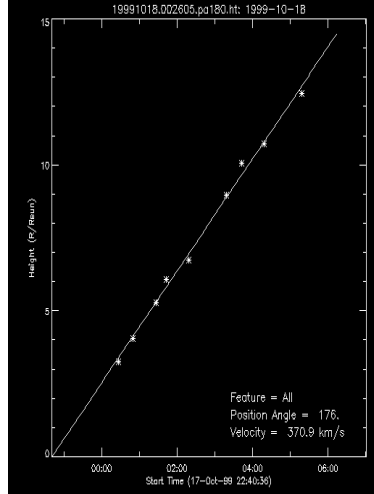
8.11 Height-Time plot → speed

A particular feature in successive images are tracked to obtain the height-time plot.

The slope gives the speed of the CME

Many CMEs initially accelerates to a velocity of 800-1000 km/s within ~ 20 minute

CME accelerations range from $20 - 6800 m/s^2$. 74% of the events reach their peak acceleration at lower corona, i.e., heights below $0.5 R_s$.



8.12 Acceleration of CMEs

The early acceleration phase of typical CMEs mostly ceases by the time it has reaches around $2R_{\theta}$. This indicates that the CME, having mass of order of $\sim 10^{13}$ kg must be accelerated to 100s of km s^{-1} by this distance.

Hence, the erupting CMEs magnetic structure must have a mechanism to attain such energies over a relatively short time scale.

Some theoretical models suggest that this involves an interaction between the erupting and the surrounding field, via runaway magnetic reconnection.

The CME onset itself must involve some instability disrupting the equilibrium between the closed magnetic field in the corona and the tendency of the corona towards its natural state of expansion.

The release of the stored free magnetic energy driving a CME can provide mechanical form of an expanding CME, and erupting filament, flare emission and acceleration of energetic particles, magnetic field reconfiguration and bulk plasma motion.

8.13 Theoretical considerations for modeling

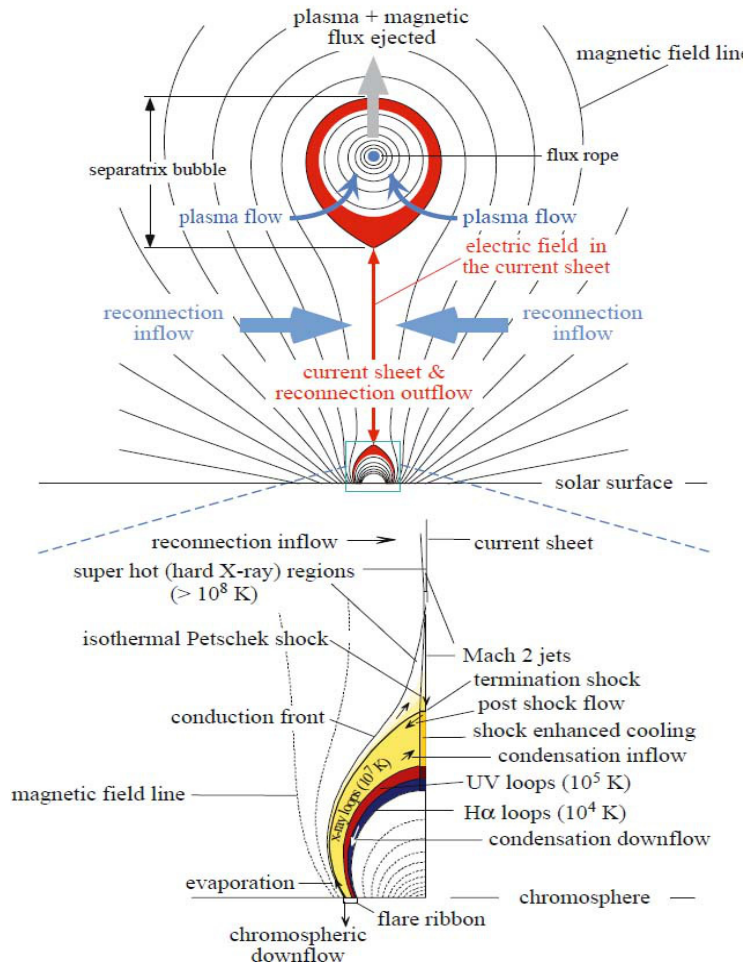
First it was postulated that CMEs might be driven by the heat of explosive flares. However, many CMEs were not associated with flares, and that even those that were often started before the flare, so the idea was shelved.

Because CMEs are initiated in the solar corona (which is dominated by magnetic energy), their energy source must be magnetic.

Most models of CMEs assume that the energy is stored up in the coronal magnetic field over a long period of time and then suddenly released by some instability, or a loss of equilibrium in the field.

There is still no consensus on which of these release mechanisms is correct, and observations are not currently able to constrain these models very well. These same considerations apply equally well to solar flares.

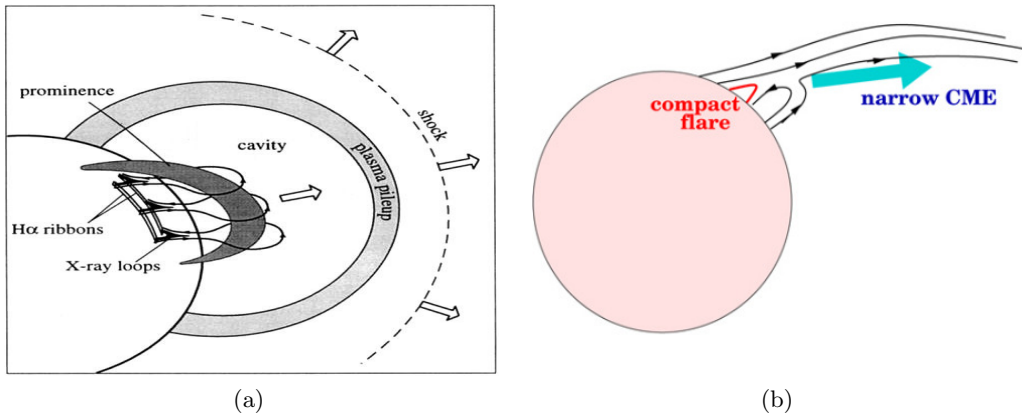
8.14 A standard unified model of solar eruption (flux cancellation and catastrophe model)



A magnetic reconnection takes place at a current sheet under a prominence as it rises up. The CME traps hot plasma below it, and a bow shock is formed above driven by the CME. The closed field region above the prominence is supposed to become a flux rope in the interplanetary medium. Flare-ribbons can form at lower layers.

8.15 Tether-Cutting model—for a standard CME

- a: Normal CME with typical three-part structure- filament eruption, flare ribbons, and the CME (from Forbes 2000)

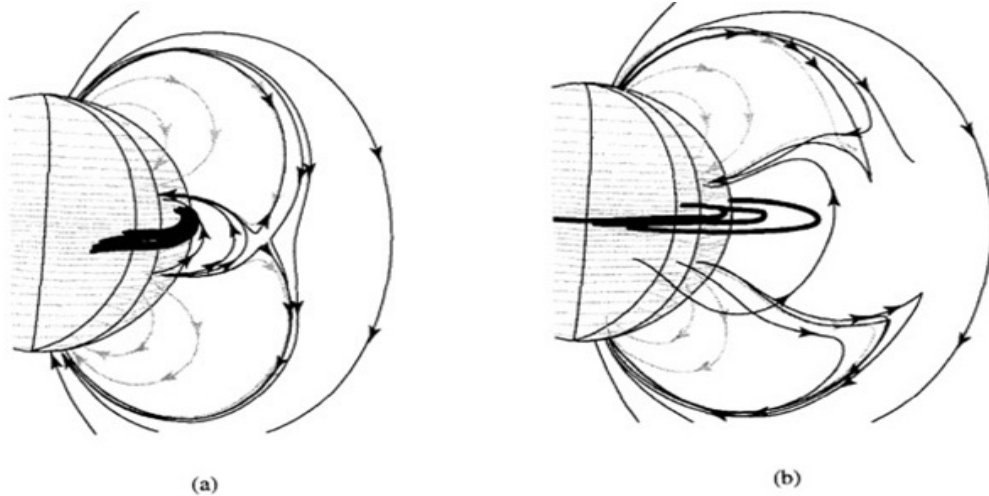


- b: A narrow CME: from the magnetic reconnection of emerging flux region near open magnetic field region (coronal hole)

In many such events, filament clearly the progenitor of the ensuing CME. Filament represent twisted flux rope structure , in equilibrium by overlying field lines-tied to solar surface.

This model includes compressed material at the leading edge of a low-density, magnetic bubble or cavity, and dense prominence (core), and a flare occurring after the filament eruption.

8.16 The break-out model



In the "magnetic breakout" model, reconnection removes the un-sheared field above the low-lying, sheared core flux near the neutral line, thereby allowing this core flux to burst open. Prominences often oscillate, even in quiescent state, and can lead to reconnection of overlying coronal field, thus creating opening for filament eruption \Rightarrow CME.

8.17 Occurrence rate: solar cycle dependence

Automated software, CACTus reported occurrence rate from < 2 per day near solar minimum to ~ 8 per day near solar maximum, (and some what similar from CDAW catalogue). The latitudinal evolution of CMEs is opposite to the evolution of sunspots. During the minimum the CMEs come from very close to the equator, whereas, the source region widens toward the maximum.

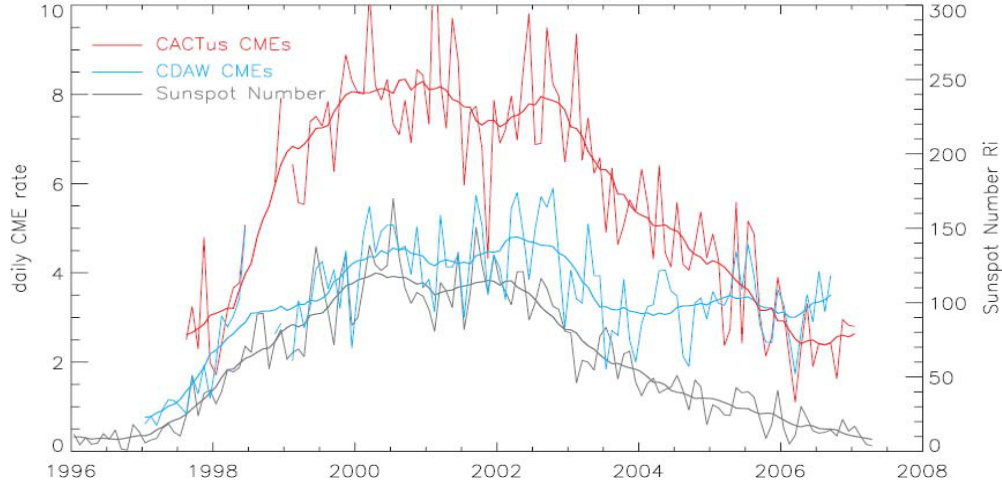


Figure 48: Daily SOHO LASCO CME rates for Cycle 23 from 1997-2006 (CACTus (red) and CDAW CME Catalog (blue)), plotted along with sunspot numbers

8.18 Interplanetary coronal mass ejections (ICME)

CMEs carry into the heliosphere large amounts of coronal plasma and magnetic fields. They are known as interplanetary CMEs or ICMEs.

During their propagation, CMEs interact with the solar wind and the interplanetary magnetic field (IMF). Slow CMEs are accelerated and fast CMEs are decelerated toward the solar wind speed.

Strongest deceleration or acceleration occurs close to the Sun, but it can continue even beyond Earth orbit (1 AU).

CMEs faster than about 500 km/s eventually drive a shock wave. This happens when the CME speed faster than local fast magnetosonic speed.

Such shocks have been observed directly by coronagraphs in the corona, and are related to type II radio bursts. They are thought to form sometimes as low as $2R_s$. They are also closely linked with the acceleration of solar energetic particles.

8.19 Remote sensing Techniques for detecting propagation of ICMEs

Several techniques have been developed to remotely detect and track disturbances related to CMEs in the interplanetary medium. These utilize radio and white light wavelengths to detect and image these structures.

The techniques are kilometric radio observations from space and metric radio interplanetary scintillation (IPS) observations from the ground.

The IPS technique relies on measurements of the fluctuating intensity level of a large number of point-like distant meter-wavelength radio source. They detect changes to density in the (local) interplanetary medium moving across the line of sight to the source. They are observed with one or more ground arrays operating in the MHz-GHz range

8.20 Propagation of a CME in the interplanetary medium

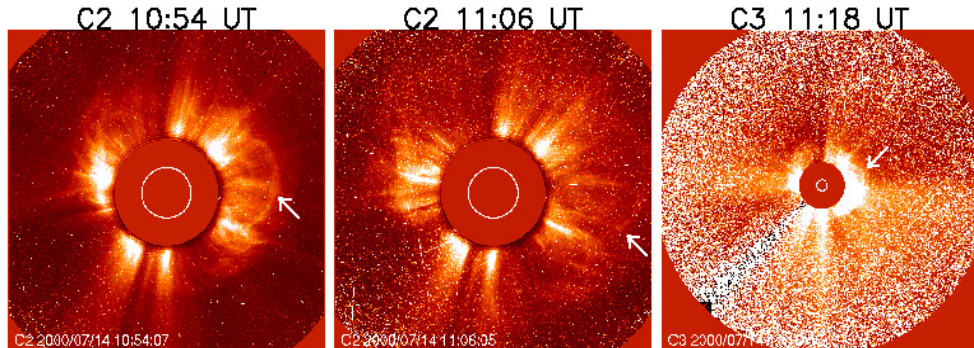


Figure 49: LASCO Images $< 30 R_{sun}$

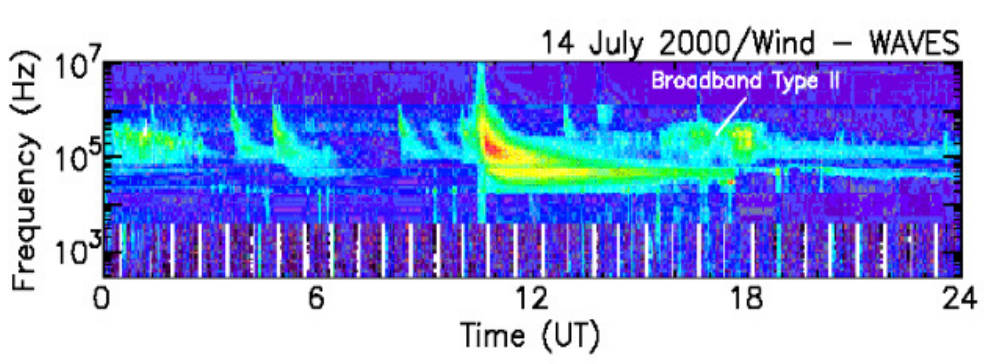


Figure 50: Radio Spectrum

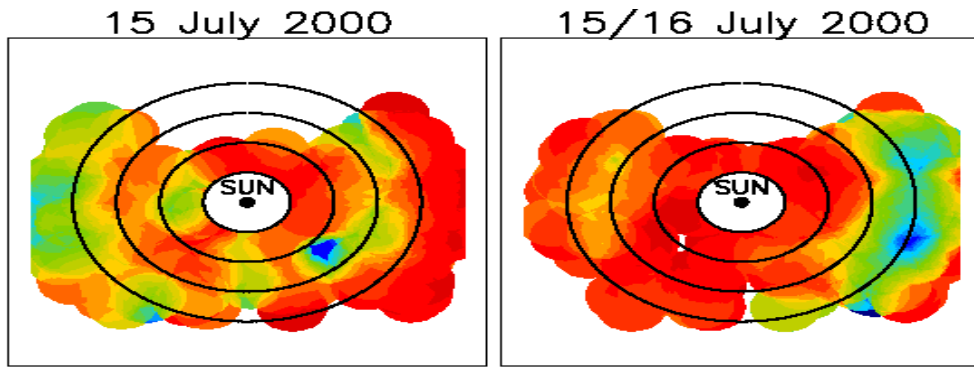


Figure 51: Radio Ooty Scintillation Images 50 - 250 R_{sun}

8.21 Sun-Earth interaction: solar wind (fast and slow streams), flares, CMEs and magnetosphere

The region behind the bow shock and surrounding the Earth is termed the magnetosphere; Magnetosphere is the region of space dominated by Earth's magnetic field . It largely prevents the solar wind from entering the earth, but some high energy solar wind particles leak into the magnetosphere and are the source of charged particles trapped in the Van Allen belts.

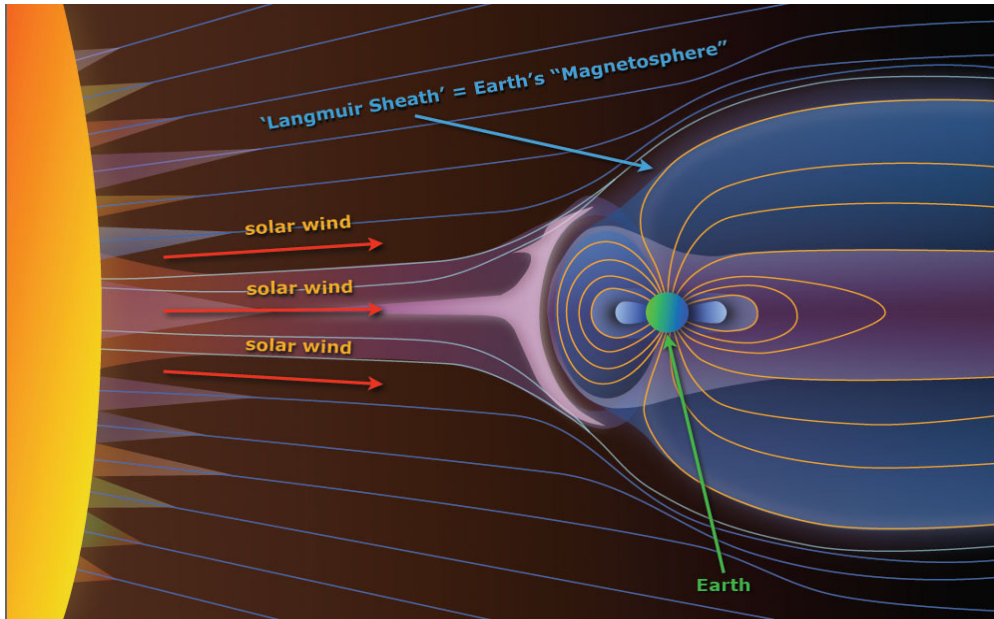


Figure 52: Radio Ooty Scintillation Images 50 - 250 R_{sun}

8.22 Impact on Earth

CMEs inject large quantities of mass and magnetic flux into the heliosphere, causing transient disturbances, driving interplanetary shocks, solar energetic particles and act as major contributor

to space weather.

When ejected towards the Earth, reaching as ICME, the shock wave causes a geomagnetic storm, compressing the magnetosphere on the day side and extending the night-side magnetic tail, which reconnects releasing terawatt scale power directed back toward Earth's upper atmosphere.

Solar energetic particles can cause aurorae in Earth's polar and high latitude regions. Energetic protons released by CME can cause increase in number of free electrons in the ionosphere, especially in the polar regions, enhancing radio wave absorption, especially within the D-region of the ionosphere, leading to Polar Cap Absorption (PCA) events.

CMES and flares can disrupt radio transmissions, damage satellites, and electrical transmission lines resulting in massive power outages.

Humans at high altitudes, as in airplanes or space stations, risk exposure to relatively intense solar particle events.

8.23 Some major recent events

9 March 1989 CME led to severe geomagnetic storm at Earth on 13 March 1989, causing power failure in Canada and short-wave radio interference.

Propagation of ICME through the Solar System

14 October 2014: ICME observed by PROBA2, SOHO, and SDO as it left the Sun, and STEREO-A observed its effects directly at 1 AU.

On 17 October, it reached Mars as observed by Mars Express, MAVEN, etc.

On 22 October, Rosetta observed it at 3.1 AU, as it reached comet 67P/Churyumov–Gerasimenko,

On 12 November, at 9.9 AU, it was observed by Cassini at Saturn.

Three months later, New Horizons spacecraft 31.6 AU approaching Pluto detected arrival of the CME, and Voyager 2 data interpreted its passing 17 months later.

The Curiosity rover's RAD instrument, Mars Odyssey, Rosetta and Cassini showed a sudden decrease in galactic cosmic rays (Forbush decrease) as the CME's bubble passed by.

8.24 Summary

- CMEs, filament eruptions, and flares are three different large-scale eruptive phenomena that occur in the solar atmosphere. It is believed that they are closely related, different manifestations of a single physical process.
- The CME initiation follows storage of energy in closed magnetic field regions on the Sun over a period of time, but its trigger is not obvious.

- Statistically, CMEs are more associated with erupting filaments and X-ray long duration events, and not optical flares.
- Not all CMEs are associated with flares or filament eruptions, but a major flare is invariably associated with a CME.
- CMEs involve destabilization of large-scale coronal structures resulting in reconfiguration of the larger-scale weak fields at high latitudes, and of smaller-scale, strong fields at low latitudes.
- Halo CMEs are important in terms of forecasting space weather. When directed Earthward, can cause major geomagnetic storms at Earth.

Read Euler, read Euler, he is the master of us all.